AstraLux

High Angular Resolution Astronomy with an Electron Multiplying CCD

Felix Hormuth

2007

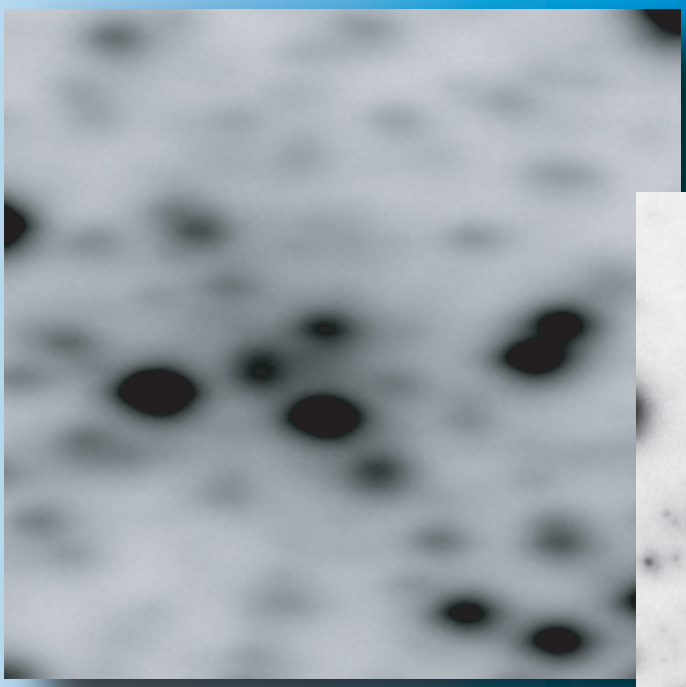

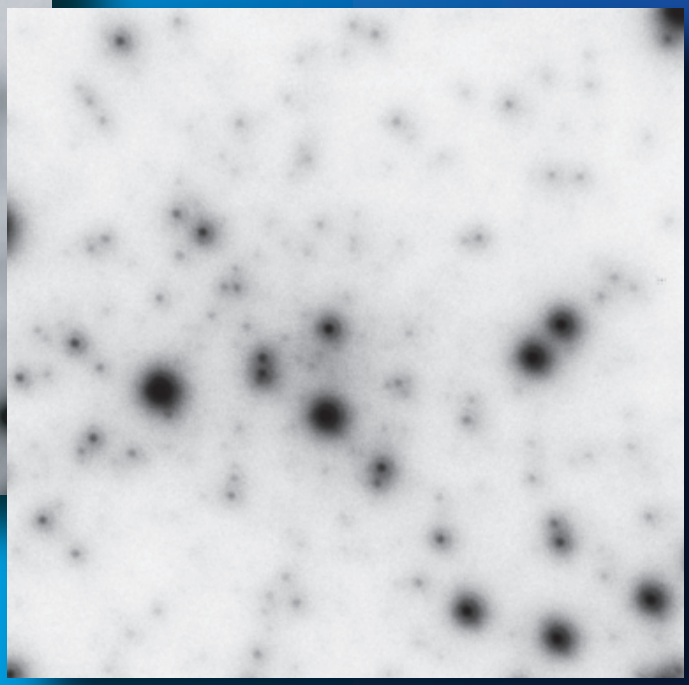

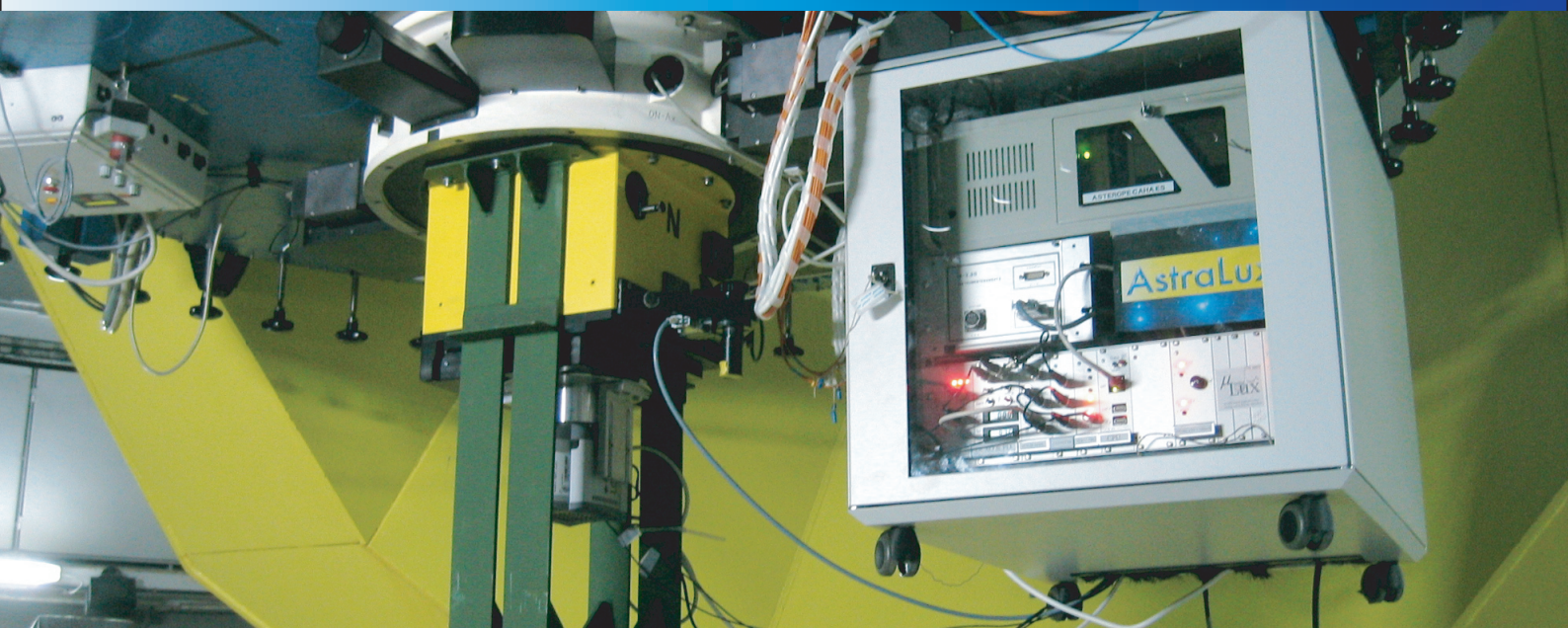

Cover illustration:

Middle: The central 9×9″ of the globular cluster M15, both seeing limited and as observed with AstraLux at the Calar Alto 2.2 m telescope in Lucky Imaging mode.
Bottom: AstraLux and μLux at the Cassegrain focus of the Calar Alto 2.2 m telescope.

Faculty of Physics and Astronomy
University of Heidelberg

Diploma thesis
in Physics

submitted by
Felix Hormuth
born in Mannheim

2007

AstraLux:
High Angular Resolution Astronomy with an Electron Multiplying CCD

This diploma thesis has been carried out by Felix Hormuth at the
Max-Planck-Institut für Astronomie
under the supervision of
Prof. Thomas Henning

Abstract

The spatial resolution of astronomical observations from the ground is impaired by earth's atmosphere. Turbulent variations of the refractive index of the air above a telescope degrade the image resolution to values of typically one arcsecond in the visible light, seventy times worse than the diffraction limit of an 8-m class telescope.
This has been overcome in the past years by the development of adaptive optics systems. These instruments actively compensate the wavefront aberrations introduced by the atmosphere and allow diffraction limited imaging at large telescopes in the near infrared.
This thesis covers an alternative, totally passive approach to the problem of high resolution imaging through the atmosphere. The "Lucky Imaging" technique exploits the temporal behaviour of atmospheric turbulence. By selecting only the best few percent of several thousand short exposure images, it is possible to recover the full angular resolution of medium-sized telescopes at visible wavelengths. This can be realised with a fraction of the instrumental effort and costs that is needed for adaptive optics.
AstraLux, a dedicated instrument for this purpose, has been developed, tested, and used for observations at the Calar Alto 2.2 m telescope. Its design, performance, and first scientific results are presented in this work.

Zusammenfassung

Die räumliche Auflösung bodengebundener astronomischer Beobachtungen wird durch die Erdatmosphäre beeinträchtigt. Turbulente Schwankungen des Brechungsindex der Luft oberhalb eines Teleskops begrenzen die erreichbare Winkelauflösung auf typische Werte von einer Bogensekunde – etwa siebzigmal schlechter als das theoretische Auflösungsvermögen eines Teleskops der 8-m Klasse.
Diese Schwelle wurde in den letzten Jahren durch die Entwicklung adaptiver Optiken überwunden. Solche Systeme kompensieren die von der Atmosphäre aufgeprägten Wellenfrontstörungen aktiv und ermöglichen damit beugungsbegrenzte Aufnahmen im nahen Infrarot.
Die vorliegende Arbeit behandelt eine alternative, rein passive Technik der hochauflösenden bodengebundenen Bildgewinnung. Die Methode des "Lucky Imaging" nutzt die zeitlichen Charakteristika atmosphärischer Turbulenz geschickt aus. Indem nur die besten wenigen Prozent von vielen tausend kurz belichteten Einzelaufnahmen genutzt werden, wird das volle Auflösungsvermögen von Teleskopen mittlerer Größe im sichtbaren Licht erreicht. Hierzu ist nur ein Bruchteil des instrumentellen und finanziellen Aufwands nötig, der bei adaptiven Optiken zu bewältigen ist.
AstraLux, ein eigenständiges Instrument für Lucky Imaging, wurde entwickelt, getestet und für Beobachtungen am 2.2 m Teleskop auf dem Calar Alto benutzt. Das Design, die Leistungsfähigkeit und erste wissenschaftliche Ergebnisse mit diesem Gerät werden in dieser Arbeit präsentiert.

Contents

List of Figures

Chapter 1

Introduction

Looking at the sky with naked eyes in a clear night you will see thousands of stars. All of them appear to change their brightness in an irregular pattern, they “twinkle”. Except in a very few special cases, this is not caused by any physical processes in these stars.

In fact, it is the result of turbulent variations of temperature and pressure in the air above us. A more detailed look at the stars using a telescope with large magnification will show another aspect of these turbulences. The stars do not appear point-like as expected, but seem to be blurred and dispersed into multiple tiny speckles. This is called atmospheric seeing.

It is actually an everyday experience that temperature variations of the air have an effect on the appearance of distant objects: On a hot summer’s day, the mixing of warm and cold air above the black tarmac of a street will distort the images of trees or houses seen close to the horizon. If you ever had a seat in the middle of an aeroplane and watched the ground looking through the hot and dense exhausts of the jet engine, you will have observed the same effect even stronger.

The impact of earth’s atmosphere on the image quality of astronomical observations is fortunately not as extreme as in the examples above. Nevertheless, atmospheric seeing has limited the achievable image resolution for the largest part of the history of observational optical astronomy.

1.1 Astronomy and the Turbulent Atmosphere

Let us switch to a more physical approach to the problem of observing the stars through a turbulent medium – in this case air. The sheer existence of such phenomenons like wind, rain, snow, hot days, cold days etc., in one word: weather, teaches us that the atmosphere surrounding us is not in equilibrium. Local variations of temperature and pressure induce flows on a large range of temporal and spatial scales. In a low-viscosity medium like air, these flows will never be laminar, but turbulent.

At any given moment in time, the atmosphere above a telescope can be imagined as an inhomogeneous mixture of turbulent air cells with different temperatures and pressures. The connection between such inhomogeneities and the blurring of distant objects is established by the depen-

dency of the air's refractive index on these quantities:

$$n(P,T,\lambda) \sim 1 + 7.8 \cdot 10^{-5} \left(1 + 7.5 \cdot 10^{-3} \frac{1}{\lambda^2}\right) \frac{P}{T} \tag{1.1}$$

Here, the light's wavelength λ is measured in μm, the air temperature T in Kelvin and the pressure P in mbar.
The propagation velocity of light through a dense medium is given by c/n. If two rays of light with the same wavelength are sent through the atmosphere, and one of them has to pass a region of colder or denser air, it will be delayed with respect to the other. This delay is equivalent to a *phase difference*.
More suitable than looking at individual rays, one can visualise the light of a distant star as a flat *wavefront* coming from space. If such a wavefront hits the atmosphere like shown in Figure 1.1, the different temperatures and pressures, hence diffraction indices, of the turbulent cells will add different phase shifts. On its arrival on the ground, the wavefront will be bent and distorted. This is the reason for the blurring of astronomical images, the "seeing".

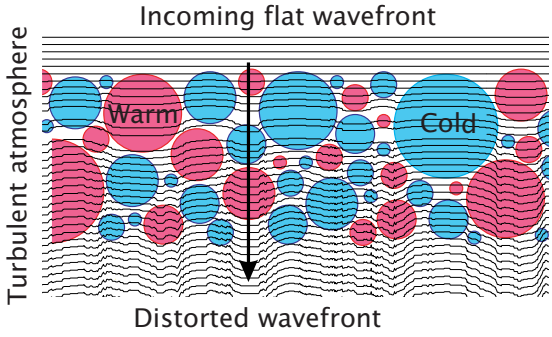

Figure 1.1. *Wavefront distortions caused by turbulent cells with different temperatures or pressures. Adapted from Egner (2003).*

Before starting with a mathematical description of these turbulences and their implication for image quality, a qualitative approach helps to understand how severe the effects of atmospheric seeing on ground-based astronomy are.
The top row of Figure 1.2 shows the theoretical, diffraction limited *point spread functions* (PSF) of three perfect telescopes with different diameters D: 10 cm, 70 cm and 2.2 m. The central parts of the PSFs, the Airy-disks, are surrounded by the first diffraction ring, best visible in the printed images for the 70 cm telescope. This is how a distant star would appear in the absence of the atmosphere. The angular resolution of a diffraction limited telescope, according to Rayleigh, is defined as the angular distance between the PSF peak and the intensity minimum between the Airy disk and the first diffraction ring. In the case of a circular aperture, this angle depends only on the telescope diameter D in metres and the wavelength λ in μm:

$$\alpha = 1.22 \frac{\lambda}{D} \tag{1.2}$$

Another convenient measure for the resolution is the angular diameter of the Airy disk at which the intensity drops to half the value of the peak intensity – the full width at half maximum:

$$\mathrm{FWHM}_{\mathrm{DL}} = 1.02 \frac{\lambda}{D} \tag{1.3}$$

where the subscript *DL* stands for diffraction limited.

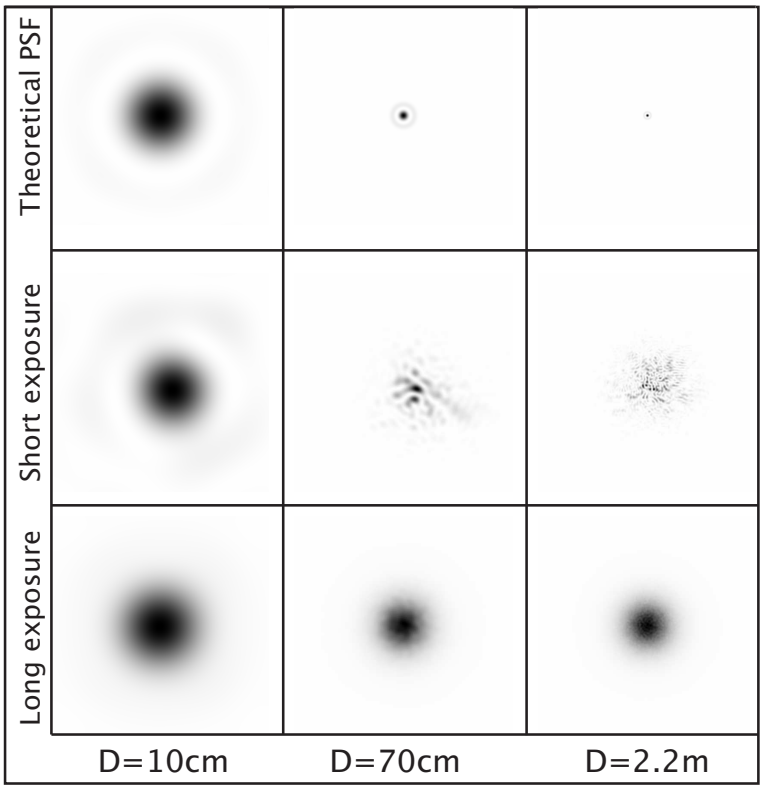

Figure 1.2. *Simulated theoretical and seeing limited short and long exposure point spread functions of a telescope with 10 cm, 70 cm and 2.2 m diameter.*

In the visible light, at $\lambda \approx 500$nm, a telescope with a diameter of 8 m can in theory resolve angles as small as 17 milli-arcseconds. This corresponds to a linear resolution of ≈3 cm at a distance of 400 km – good enough to identify which crew member of the International Space Station is looking out of the window.

The middle row of Figure 1.2 shows how a star would appear in a very shortly exposed image, taken with the same telescopes, but now through the turbulent atmosphere. If a 10 cm telescope is used, the star looks quite similar as in the diffraction limited case. The PSF is only slightly blurred and a bit shifted to the right. The picture is totally different for the 70 cm and 2.2 m telescopes: Instead of a single peak at the position of the star, its image is dispersed into many tiny speckles, each with approximately the same diameter as the diffraction limited PSF.

If many of such short-exposure frames are averaged, as it would be the case in a long-exposure image taken with a CCD camera or a photographic emulsion, these speckle patterns merge into a *seeing disk* with a much larger angular diameter than the individual speckles. Such long-exposure images are shown in the bottom row of Figure 1.2. For the 10 cm telescope, this seeing disk is only slightly larger than the theoretical PSF. Apparently, the atmospheric turbulence did not do too much harm to the image quality.

In the case of the 70 cm telescope, the seeing disk is almost five times larger than the diffraction limited FWHM. The angular diameter of the seeing limited PSF of the 2.2 m telescope is as large as for the 70 cm telescope. Though the theoretical resolution of the 2.2 m telescope is three times better, the atmospheric turbulence limits the achievable image resolution, independently of the telescope's diameter.

The seeing limited images in Figure 1.2 were simulated for an atmospheric turbulence that provides a seeing of 0.8 arcseconds, a quite common value. This is the FWHM of a seeing-limited image, obtained through a telescope which has a theoretical angular resolution that is much better than this value. In the case of the 10 cm telescope, the diffraction limited FWHM at the chosen wavelength of 500 nm has a diameter of already $1\farcs05$ – larger than the seeing limit. This is the reason why the atmospheric turbulence did not affect the final image too much. Effectively, the diffraction limited PSF is convolved with a Gaussian which has the FWHM of the seeing value. For the 10 cm telescope, the resulting FWHM is $1\farcs3$. For the 70 cm and 2.2 m telescopes, the diffraction limited FWHM sizes are $0\farcs15 = 150$ mas and 48 mas, respectively. This is almost negligible compared to the seeing limit of $0\farcs8$, which determines the final PSF size.

When long-time exposures are obtained through the turbulent atmosphere, larger aperture diameters D do not provide better spatial resolution, but only more sensitivity. The photon flux received from a star scales with the aperture area, i.e. with D^2. Since the size of the PSF remains constant in the seeing limited case, the peak value of the PSF and with it the peak signal-to-noise ratio will scale with D^2 also. If the diffraction limit of large telescopes could be recovered, the light would be concentrated into a smaller area, since the PSF diameter is $\propto 1/D$. In the diffraction limited case, the signal-to-noise ratio for a point source would hence scale with D^4.

The atmospheric seeing thus affects not only the spatial resolution of observations obtained through large telescopes, it also deteriorates the sensitivity. Overcoming the effects of atmospheric turbulence would provide higher image resolution as well as improved detection capabilities for faint objects.

1.2 Turbulence Statistics

This section gives a brief introduction into the statistical description of atmospheric turbulence. The *Fried parameter* r_0, a measure for the turbulence strength, is introduced.

1.2.1 Phase Structure Function and Fried Parameter

A very convenient way to describe atmospheric turbulence and its implications for image quality is based on the *Kolmogorov* model, developed by Tatarski (1961). This model is based on the assumption that the energy power spectrum $\Psi\kappa$ of the turbulence depends on the spatial frequency κ as:

$$\Psi(\kappa) \propto \kappa^{-11/3} \tag{1.4}$$

On the time average, optical phase perturbations can be best expressed by a *phase structure function*:

$$\mathcal{D}(|\mathbf{r} - \mathbf{r}'|) = \left\langle |\phi(\mathbf{r}) - \phi(\mathbf{r}')|^2 \right\rangle \tag{1.5}$$

In the case of Kolmogorov turbulence as the underlying physical process, this structure function can be described in terms of a single parameter r_0:

$$\mathcal{D}(|\mathbf{r} - \mathbf{r}'|) = 6.88\,(|\mathbf{r} - \mathbf{r}'|/r_0)^{5/3} \tag{1.6}$$

This parameter r_0, the *Fried parameter* is a measure of the total strength of the wavefront aberrations caused by atmospheric turbulence (Fried, 1965). It can be understood as a kind of coherence length of the turbulent structures.

If the wavefront variance as described by the above structure function is integrated over the aperture of a telescope with diameter D, the total wavefront variance will be:

$$\sigma_\Phi^2 = 1.0299\left(\frac{D}{r_0}\right)^{5/3} \tag{1.7}$$

For values of r_0 close to the telescope diameter, this allows to predict the image quality in the focal plane (see Section 1.3).
The Fried parameter can also be directly related to the full width at half maximum of the seeing limited PSF in a long-time exposure by:

$$\mathrm{FWHM_{SL}} = 0.98\frac{\lambda}{r_0} \tag{1.8}$$

This equation exactly contains the conclusions from the previous section: the diameter of a telescope does not determine the spatial resolution in the seeing limited case. Instead, the effective diameter is approximately given by the Fried parameter r_0. This equation shows one possibility how r_0 can be actually determined. At known wavelength, it can be calculated from the measured FWHM of stars on astronomical images. Since such measurements might be affected by telescope tracking errors or telescope vibrations, special instruments for the measurement of atmospheric seeing parameters have been developed, e.g. the *Differential Image Motion Monitor* (DIMM, Sarazin and Roddier (1990)). Typical values for r_0 at a wavelength of 500 nm are 10−20 cm, corresponding to a seeing of $0\farcs5$–$1''$.

The structure function given by equation 1.6 would predict that the phase difference between two points of a wavefront increases infinitely with the distance between these points. But in reality, the phase structure function starts to flatten out at separations of a few 10 m. This is related to the structure of the atmospheric turbulence. The size of the turbulent cells is limited to typical values of 10−30 m, the *outer scale* L_0. As long as this length is ≈10 times larger than the telescope diameter, it can be neglected for seeing considerations (Winker, 1991). There is also an *inner scale* l_0 of turbulence, at which the turbulent energy is dissipated by the air's viscosity. For most applications, including astronomical observations in the optical and infrared, this scale length is not relevant (Roddier, 1981).

1.2.2 Refractive Index Structure Function

A direct approach to the optical effects of atmospheric turbulence is the *refractive index structure function* C_N^2, describing the turbulent refractive index variations and their dependency on the height h above an observer. The C_N^2 structure function is related to the Fried parameter by:

$$r_0 = \left(16.699\lambda^{-2}\frac{1}{\cos\gamma}\int_0^\infty C_N^2(h)dh\right)^{-3/5} \tag{1.9}$$

Here γ is the angular distance between the zenith and the line of sight, accounting for the larger airmass at lower elevations.

As visible in equation 1.1, the refractive index of air varies only slightly with wavelength in the optical regime. The refractive index structure function can therefore be assumed to be independent on the wavelength, resulting in a very useful relation between the Fried parameter r_0 and wavelength λ:

$$r_0 \propto \lambda^{6/5} \tag{1.10}$$

This implies that the effective optical turbulence strength decreases towards longer wavelengths. As shown in the following sections, this has important consequences for the spatial and temporal behaviour of atmospheric seeing and the performance of techniques that aim at the recovery of a telescope's diffraction limit.
In the seeing limited case, the FWHM of the seeing disk as observed through a large telescope will decrease with increasing wavelength, at least as long as r_0 is much smaller than the telescope's diameter.

1.2.3 Imaging through Turbulence

An incoming plane wave at a given time t and position $\mathbf{r}$ can be mathematically described as a complex field ψ_0:

$$\psi_0(\mathbf{r}, t) = A\mathrm{e}^{i(\Phi_0 + 2\pi\nu t + \mathbf{k}\cdot\mathbf{r})} \tag{1.11}$$

where A is the amplitude, $\mathbf{k}$ the wave vector with $|k|=2\pi/\lambda$, and $\nu=c/\lambda$ the light's frequency. A constant phase offset is represented by ϕ_0.

The wavefront distortions caused by atmospheric turbulence can be expressed as changes of the phase component. The perturbed wavefront ψ_p at any given time is related to the original wavefront ψ_0 by the following equation:

$$\psi_p(\mathbf{r}) = \psi_0(\mathbf{r})\chi_a(\mathbf{r})e^{i\Phi_a(\mathbf{r})} \tag{1.12}$$

Here χ_a is the influence of the atmospheric turbulence on the amplitude, and Φ_a are the induced phase differences. The PSF that corresponds to such a wavefront is derived by Fourier transforming this expression. To simulate a finite telescope aperture D, the wavefront amplitude is set to zero for all points with $|\mathbf{r}|>D/2$.

For astronomical observations through the turbulent atmosphere, the changes in wavefront amplitude are only relevant for very small apertures – as e.g. the human eye. At telescopes with diameters larger than the Fried parameter r_0, the resulting *scintillation* of the observed sources is of the order of only a few percent. Its effect on image quality is almost negligible and will not be considered in the following.

To assess the effects of atmospheric turbulence on the image in the focal plane of a telescope, it is convenient to introduce the *optical transfer function* (OTF). The OTF determines the representation of spatial frequencies k in an image, thus the angular resolution. It is related to the phase structure function $\mathcal{D}$ by (e.g. Roddier, 1999, Chapter 1):

$$\mathrm{OTF}(k) = \exp\left(-\frac{1}{2}\mathcal{D}(\lambda f k)\right) \tag{1.13}$$

In this representation, the phase structure function now depends on the wavelength λ times the spatial frequency k in the focal plane, multiplied by the focal length f of the imaging system.
Since the phase structure function given in equation 1.6 describes the time average, it can be inserted in equation 1.13. This results in the optical transfer function for a seeing-limited long-time exposure through the turbulent atmosphere:

$$\mathrm{OTF}_{\mathrm{seeing}}(k) = \exp\left[-3.44\left(\frac{\lambda f k}{r_0}\right)^{5/3}\right] \tag{1.14}$$

The real image of a point source in the focal plane of a telescope – the point spread function (PSF) – is then derived from the Fourier transform of the OTF:

$$\mathrm{PSF}(r) = \left| \mathcal{FT} \left\{ \mathrm{OTF}_{\mathrm{seeing}} \cdot \mathrm{OTF}_{\mathrm{telescope}} \right\} \right|^2 \tag{1.15}$$

where $\mathrm{OTF}_{\mathrm{telescope}}$ is the optical transfer function of the telescope, defined by shape and size of the aperture in the case of a perfect optical system. The dependency of the seeing limited OTF on $\exp(r_0^{-5/3})$ means that strong atmospheric turbulence, i.e. "bad" seeing and small values of r_0, suppresses high spatial frequencies more than "good" seeing, corresponding to large values of r_0. This is exactly what was shown in Figure 1.2: the fine speckle structure in the short exposure images is averaged out to a smooth PSF with a larger FWHM, containing only low spatial frequencies.

1.3 Measuring Image Quality: the Strehl Ratio

The angular resolution of an astronomical image is only one aspect of its quality. The FWHM of a stellar PSF does not tell which fraction of the star's light is actually concentrated in the central peak. As visible in the short-time exposures in Figure 1.2, most of the light might be actually distributed to numerous speckles surrounding the brightest peak. If an image should not only provide high resolution, but should allow to detect faint sources on a noisy background also, it is essential that as much signal of an object as possible is confined to an area preferably as small as the theoretical PSF.

Karl Strehl (1902) introduced a measure for this kind of image quality, nowadays referred to as *Strehl ratio*. This number is the ratio of the peak intensity of a point source's actual image over the peak intensity if it was observed with a diffraction limited optical system in the absence of any aberrations or atmospheric seeing. Obviously, any redistribution of light from the Airy disk to speckles at larger angular separations results in a decrease of the Strehl ratio, since the total flux remains constant.

An optical system, e.g. a telescope, is referred to as diffraction limited if it provides a Strehl ratio of at least 80%. At Strehl ratios of about 20% and more, the first diffraction ring around a star's image becomes partially visible. Starting at ≈50% Strehl ratio, the first diffraction ring will appear closed.

In principle, the Strehl ratio can be calculated analytically if the exact shape of the incoming wavefront is known (e.g. Hardy, 1998). For most applications, the following approximation gives good results for Strehl ratios >2%, corresponding to a wavefront RMS σ_Φ below 2 rad (Born, 1999):

$$S \sim \exp\left(-\sigma_\Phi^2\right) \tag{1.16}$$

For a diffraction limited system with ≥80% Strehl ratio, the total wavefront RMS thus has to be less than ≈0.5 rad, corresponding to a required accuracy of the mirror or lens surfaces with an RMS of less than $\lambda/13$.

For observations through the turbulent atmosphere, the total wavefront RMS is on average too high to result in useful Strehl ratio estimates with equation 1.16. Instead, in the seeing limited case it is reasonable to assume that the atmospheric turbulence disperses the light of a single star into $\approx(D/r_0)^2$ speckles with similar brightness. In a short-exposure as well as long-exposure image – which is nothing else than the time-average of short exposures – the Strehl ratio can

therefore be estimated as $S=(r_0/D)^2$. Under a V-band seeing of 1″, corresponding to r_0=10 cm, this leads to a Strehl ratio of ≈2% at a 70 cm telescope, but only 0.2% at a 2.2 m telescope.

This estimate can be used to assess the gain in signal-to-noise if a point source, e.g. a star, is first imaged with a seeing limited system and then with some kind of image improving technique that leads to a higher Strehl ratio. If the star's light can be concentrated into a single speckle with a strehl ratio of 100%, the gain will be $(D/r_0)^2$. A real imaging system will never fully reach the diffraction limit, so this gain has to be multiplied by the achieved Strehl ratio:

$$g_{\mathrm{SNR}} \sim S \cdot \left(\frac{D}{r_0}\right)^2 \tag{1.17}$$

This approximation gives good results for $D/r_0 \geq 7$ and is quite useful to assess the performance of image improving techniques. If an image improving system (or algorithm) is able to provide a Strehl ratio of 25%, i.e. S=0.25, the gain in signal to noise at D/r_0=7 is ≈10. In the case of a background limited astronomical observation, such an improvement allows to achieve the same result as in the seeing limited case in only one tenth of the time. Additionally, the improved image will provide a higher spatial resolution than the seeing limited one.

1.4 Spatial and Temporal Decorrelation Effects

For many applications it is a convenient and sufficient assumption that atmospheric turbulence is confined to thin layers at certain heights. Measurements of the C_N^2 turbulence profile above a number of astronomical observatories (e.g. Avila et al., 1998; Klueckers et al., 1998; Egner et al., 2006) support this approach. Taylor (1938) introduced the "Taylor phase screen" model, in which the temporal and spatial characteristics of wavefront aberrations are exclusively attributed to the wind-induced motion of the turbulent layers above the telescope. The turbulent structure within these layers is assumed to be fixed, at least for the time needed by such a phase screen to move across the telescope aperture.
The phase screen model is widely used in simulations of atmospheric turbulence and seeing. Numerical simulations are usually not based on continuous C_N^2 profiles, but calculate the wavefront aberrations caused by typically 1−10 infinitely thin layers at heights between 0 m and 10000 m. Experimental setups for testing of astronomical instrumentation in the laboratory often use several glass plates with etched or ion diffusion generated aberration patterns, each simulating a different turbulence layer (e.g. Butler et al., 2004; Hippler et al., 2006).

The lowest layer, the ground-layer, is in most cases located at the height of the telescope aperture or at least within the first 100 m above it. Measurements indicate that ≈50% of the total turbulence are normally confined to this layer. If the image quality of a single on-axis star is of interest, only the total atmospheric turbulence, i.e. the effective combined r_0 of all layers, has to be considered. This is not true if multiple objects are observed or if the temporal evolution of the speckle pattern is examined.

1.4.1 Spatial Decorrelation: the Isoplanatic Angle

If two stars, separated by an angle $\theta>0°$ are observed through an atmosphere with a layered turbulence structure, their PSFs will differ from each other. The illustration in Figure 1.3 shows the reason for this: since at least a fraction of the atmospheric turbulence is confined to high layers,

in this example at h=5000 m and h=8000 m, the footprints of the telescope aperture sample different parts of these layers. The linear separation between the footprints will be $x = \theta h$ for small angles θ. In the shown example, the aperture footprints of a telescope with 2.2 m diameter will be fully separated in the top layer at an angle of $\theta > 1'$. Thus the contribution of the top layer to the wavefront aberrations seen by the telescope will be completely decorrelated for these two stars. The difference between the resulting total wavefronts leads to different PSFs in the focal plane of the telescope, as shown in the bottom part of Figure 1.3.

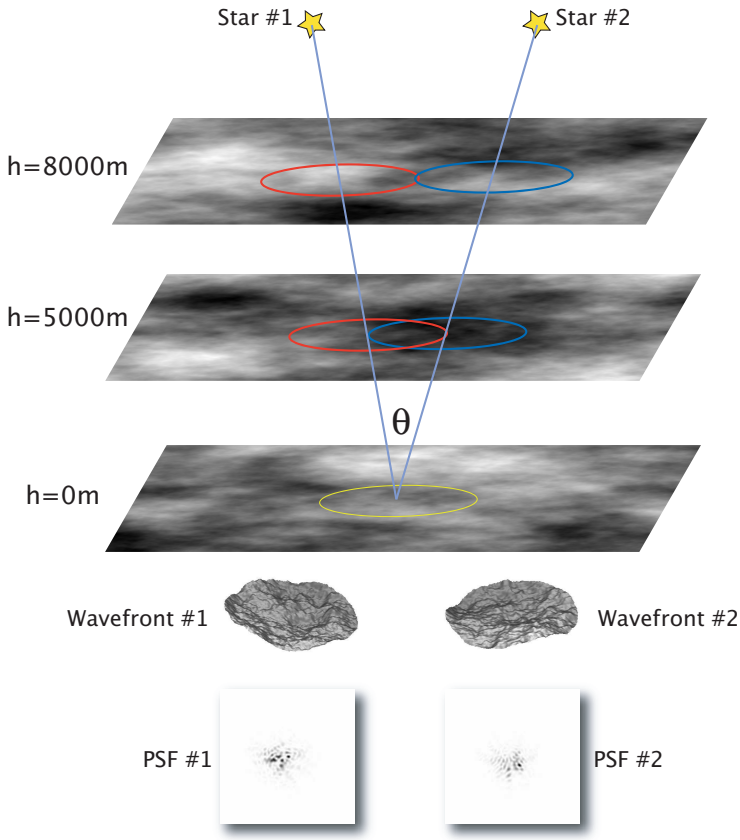

Figure 1.3. *Illustration of anisoplanatic effects due to turbulent layers at different heights. The telescope aperture and the ground layer in this example would be at a height of 0 m. While the footprints of the aperture for observations of two stars with an angular separation θ=1′ still overlap in the mid-altitude layer at h=5000 m, they probe completely different portions of the high-altitude layer at h=8000 m. The different total wavefront aberrations seen in the directions of the two stars lead to different point spread functions in the focal plane.*

Adaptive optics, the most widely used image improvement method (see Section 1.5.2), usually corrects the wavefront of an on-axis reference star to recover the diffraction limit of a telescope. The described anisoplanatic effects cause a decrease of the achieved image quality with increasing angular separation from this reference. The angle at which the variance of the difference between the wavefronts arriving from two objects is 1 rad^2 is called the *isoplanatic angle* θ_e, sometimes denoted as θ_0. If an image improving technique is able to achieve a Strehl ratio of 100% for an on-axis object, the Strehl ratio of an object separated by θ_e will drop to $1/e$, approximately 37%. Figure 1.4 shows simulated example PSFs like they could have been produced by an adaptive optics system. The Strehl ratio of the assumed on-axis reference star is 48%. While

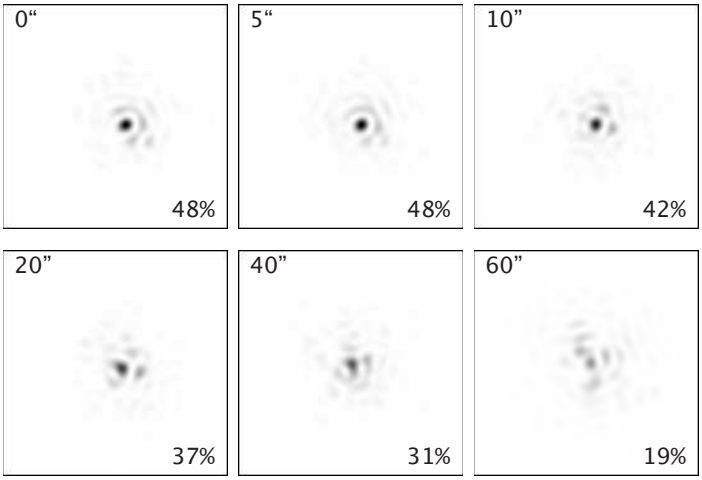

Figure 1.4. *Example PSFs, showing spatial decorrelation of the PSF pattern and Strehl ratio due to anisoplanacy.*

a 5″ separated star shows a nearly identical speckle pattern with the same Strehl ratio, the PSF at 10″ distance begins to exhibit decorrelation effects. At an angular separation of 60″ – the isoplanatic angle used for this simulation – the PSF structure is fully decorrelated with respect to the reference star, and the Strehl ratio has dropped to nearly 1/*e* times the 48% of the reference.

The effectivity of any image improving technique that is based on wavefront correction or Strehl ratio optimisation of a reference object has to be assessed, amongst others, with respect to the isoplanatic angle it can provide. Typical measured values for θ_e in adaptive optics applications range from 1−5″ in the *V*-band, e.g. 2.″3 at the Calar Alto observatory (Ziad et al., 2005). These values scale like the Fried parameter r_0 with $\lambda^{6/5}$, resulting in isoplanatic angles of ≈10−40″ in the *K*-band. The isoplanatic angle can be determined either directly on adaptive optics images by measuring the Strehl ratios of stars with different angular separations from the reference, or by using dedicated instruments for the characterisation of atmospheric parameters, e.g. the *Generalised Seeing Monitor* (GSM, Ziad et al. (2002)).

1.4.2 Temporal Decorrelation: Speckle and Wavefront Coherence Time

In a simple model with a single Taylor phase screen, the observed wavefront will change as the turbulent layer is blown across the telescope aperture by the wind. The *wavefront coherence time* τ_0 is defined as the time in which the variance of the change of the wavefront is $1\,\mathrm{rad}^2$. For a single turbulent layer with a wind speed v it depends only on the Fried parameter r_0 (Roddier et al., 1982):

$$\tau_0 \approx 0.31\frac{r_0}{v} \tag{1.18}$$

At an assumed wind speed of 12 m/s, the expected τ_0 in *V*-band is ≈3 ms under a 1″ seeing. E.g. at the Calar Alto observatory, a value of τ_0=3.7 ms was measured in *V*-band under a 0.″9 seeing (Ziad et al., 2005). If the above expression is to be used for a multi-layered turbulent atmosphere, the wind speed has to be substituted by an equivalent horizontal velocity of the turbulence pattern, which can be derived from measurements of the wind speed and turbulence strength at different heights. The wavefront decorrelation timescale is relevant for image improvement techniques that aim at the correction of the incoming wavefront, such as adaptive optics.

Another important timescale is the *speckle coherence time* τ_e. Instead of the wavefront evolution, this timescale describes the temporal decorrelation of the speckle pattern in the focal plane. It is the time difference at which the normalised autocorrelation function of the intensity at a fixed position in the focal plane drops to $1/e$. If the high-frequency components of the short-exposure speckle pattern are of interest, individual exposure times have to be shorter than the speckle coherence time. Otherwise the speckle pattern will be smeared out, and information at high spatial frequencies will be lost.

Tubbs (2003) conducted detailed simulations of the speckle coherence time for different telescope diameters and values of r_0, both for single layer and multi-layer atmospheres. While Roddier et al. (1982) predict τ_e as

$$\tau_e = 0.36\frac{r_0}{\Delta v} \tag{1.19}$$

where Δv is the dispersion of the wind velocities in the atmosphere, Tubbs (2003) found that this value is by a factor of 1.4 higher for a simulated two-layer atmosphere and telescope diameters larger than $6r_0$. This is slightly longer than the wavefront coherence time τ_0, implying that speckle-based observing techniques are subject to more relaxed temporal decorrelation effects. Since both coherence times as defined above scale with r_0, they also scale with $\lambda^{6/5}$. Observations at longer wavelengths will thus benefit from an even slower wavefront and speckle pattern evolution.

Figure 1.5 shows real observational data. The $0\farcs52$ separated double star WDS 14139+2906 was observed with a time resolution of 30 ms at the Calar Alto 2.2 m telescope at an effective wavelength of 980 nm. The expected speckle coherence time for a V-band seeing of $0\farcs7$ is $\approx$100 ms at typical wind speed dispersions in the order of 10 m/s. Indeed, the speckle patterns show good correlation for at least 2−3 frames, corresponding to 60−90 ms time difference. The images show another interesting feature of the temporal behaviour of atmospheric seeing: the absolute turbulence strength, and with it the image quality, varies considerably during the 0.75 s covered by this image series. While the first diffraction ring is partly visible around the stars in the first two images, the last few frames hardly allow to detect that this is a double star at all. The Strehl ratio in this image series varies from $\approx$25% in the first image to only 3% in the worst one.
Apparently, if one would acquire a large series of such short exposure images, it might be possible to select only the best ones with the highest Strehl ratios to generate a high-resolution and high-Strehl image. This is the concept of "Lucky Imaging", described in more detail in Section 1.5.3.

1.5 High Resolution Imaging Techniques

The most consequent method to obtain image resolution close to the diffraction limit is to send a telescope to space. While this avoids the effects of atmospheric turbulence completely, costs and effort exceed what is needed for ground-based astronomy by far.
Before diffraction limited imaging from space became an issue in astronomy, the resolving power of large telescopes could be at least partly recovered. This section briefly summarises speckle methods and adaptive optics techniques, and concludes with an introduction to Lucky Imaging, a simple and effective method for diffraction limited imaging in the visible at medium sized telescope.

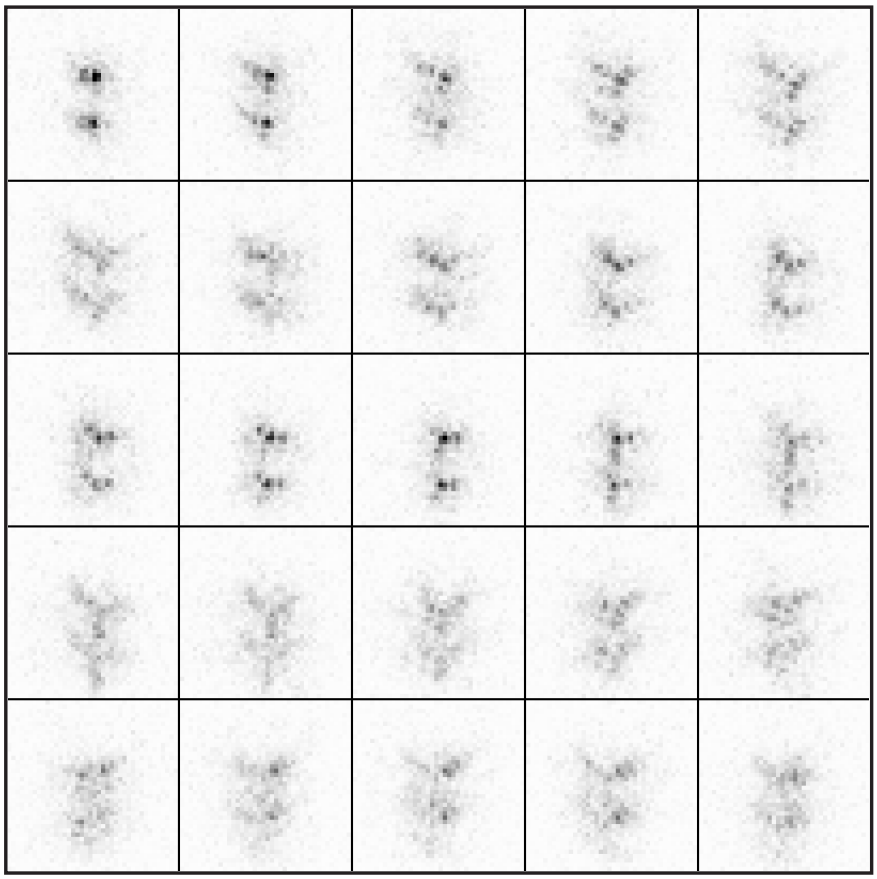

Figure 1.5. *Short exposure series of the double star WDS 14139+2906. The images show consecutive frames with an exposure time of 30 ms, acquired at an effective wavelength of 980 nm at the Calar Alto 2.2 m telescope. The field of view is 1.″9×1.″9, East is up and North to the right. Display scaling is linear with identical cuts for all images.*

1.5.1 Speckle Imaging

The comparison between the simulated long- and short-exposure examples in Figure 1.2 shows that high spatial frequencies are preserved at short exposure times. Though the image of a single star is dispersed into many speckles, each of these is a nearly diffraction limited copy of the star's point spread function. For a double star, the speckle pattern would appear twice in the image, shifted by the binary separation and in the direction of the position angle. Speckle Imaging in its most simple form can recover the separation, position angle, and brightness ratio of the double star components by autocorrelation analysis of many short exposure frames (e.g. Labeyrie, 1970, 1974). Advanced processing methods, based on bispectrum and triple-correlation techniques, are able to reconstruct two-dimensional images at the cost of increased computational effort (e.g. Knox and Thompson, 1973, 1974; Lohmann et al., 1983).
These techniques have produced a large number of valuable astronomical results in the last decades and they are still widely used especially for routine astrometric measurements of double stars. Their main limitation is the required brightness of the observed objects, typically $V \approx 10-12$ mag (e.g. Prieur et al., 1998).

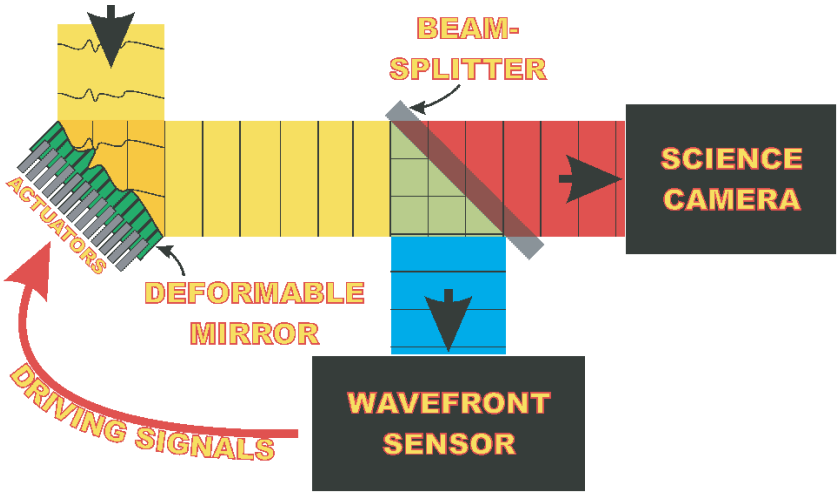

Figure 1.6. *A typical AO system. A wavefront sensor, including a high-performance computer, determines the shape of the incoming wavefront and drives the actuators of a deformable mirror. Wavefront sensor and science camera work in different wavelength ranges, splitted by a dichroic. From Egner (2003).*

1.5.2 Adaptive Optics

Adaptive optics (AO) techniques actively compensate the wavefront aberrations caused by atmospheric turbulence. First invented for military applications, adaptive optics systems are nowadays available at most larger astronomical observatories. They provide nearly diffraction limited imaging with Strehl ratios up to ≈50% in the *H*- and *K*-band, i.e. at wavelengths longer than 1.5 µm. A typical adaptive optics system consists of three main components. First, a wavefront sensor is needed to measure the shape of the incoming wavefront. Second, a high-performance computer is necessary to process the wavefront sensor output and to control the third element, a deformable mirror that is used to compensate the wavefront aberrations that were introduced by the atmosphere. Figure 1.6 shows the layout of such an AO system.
Common wavefront sensors like the Shack-Hartmann sensor (Shack and Platt, 1971), the curvature sensor (Roddier, 1988), or the pyramid sensor (Ragazzoni, 1996) measure the first or second derivative of the wavefront. The control computer has to reconstruct the true wavefront shape in real-time, which requires substantial computational effort. This shape is then converted to voltage signals for the actuators of the deformable mirror. The surface of this mirror is adjusted such that the incoming distorted wavefront is flattened upon reflection. A thorough calibration of the system has to be performed in advance to know the response of the wavefront sensor to specific wavefront aberrations and the relation between actuator signals and resulting mirror shapes.

Since the wavefront aberrations, measured in units of length, are nearly independent of the wavelength in the optical, wavefront sensing can be performed at a different wavelength than the observation. Most adaptive optics systems include a dichroic beamsplitter which directs the visible light to the wavefront sensor and the near infrared part to the science camera. This has the advantage that wavefront sensing and correction can be performed on a coarser grid. For a working AO system, the number of mirror actuators and sensor elements has to be roughly $(D/r_0)^2$. At an 8 m telescope and under a *V*-band seeing of 0.″6, this number is ≈2300 in the *V*-band, but only ≈66 in the *K*-band. Typical AO systems nowadays work with up to 400 actuators and sensor elements, providing sufficient wavefront correction only in the *H* and *K*-band. Besides the spatial aspects

of wavefront sensing, temporal aspects also limit AO to the near infrared. Sensing and correction have to be performed on timescales of one tenth of the atmospheric wavefront coherence time. In the near infrared, this results in required correction frequencies of at least 100 Hz, increasing towards shorter wavelengths with $\lambda^{-6/5}$.

All wavefront sensors have in common that they need a reference source in the field of view that provides the signal necessary for wavefront sensing. The limiting magnitude for this source is V≈14 mag for full AO performance (e.g. Kasper et al., 2000; Rousset et al., 2003), though image improvements can still be achieved with fainter references. For the Shack-Hartmann sensor, the reference does not have to be pointlike, i.e. does not necessarily have to be a star. The maximum separation between reference and science object, the isoplanatic angle, is typically 10−40″ in *K*-band. Until recently, astronomers that wanted to use AO were limited to science objects that were either bright enough to serve as the reference source itself or had a suitable natural guide star nearby.
This limitation has been overcome with the development of laser guide stars, that produce artificial reference sources by exciting sodium atoms in the earth's atmosphere at a height of ≈90 km. This allows to create an artificial guide star virtually anywhere on the sky. What is still needed is an additional natural reference star for measurements of the tip-tilt image motion. This star can be as faint as V=18 mag and may be separated from the science target by up to 60″. Due to this relaxed requirements, laser guide stars allow AO observations with a sky coverage of nearly 100% (e.g. Rabien et al., 2002; van Dam et al., 2006).

Alternative AO concepts aim at the correction of the wavefront aberrations caused by the ground layer only. Though these *ground layer adaptive optics* systems (GLAO, e.g. Tokovinin (2004)) do not reach the on-axis performance of a conventional AO system, they provide a reduction of the stellar FWHM by a factor of 2−3 over a wide field of typically 5′ diameter.
More complex systems reconstruct the wavefront aberrations separately for each turbulent layer. In these *multi-conjugate adaptive optics* systems (MCAO, e.g. Johnston and Welsh (1994); Berkefeld et al. (2001)), multiple deformable mirrors are conjugated to these layers, effectively eliminating anisoplanatic effects. MCAO systems are principally able to provide Strehl ratios >50% over a field of several arcminutes in the near infrared. Both approaches require multiple reference stars to allow the separation of the ground layer contribution or the three-dimensional reconstruction of the atmospheric turbulence.

Though AO is still technologically challenging today, with typical instrument development times of 5 years and costs of several 100000 Euro per instrument, it has evolved to the de-facto standard of astronomical high resolution imaging. For a comprehensive overview of AO systems and their history, the reader is referred to Hardy (1998) and Roddier (1999). An overview of recent scientific results can be found in Brandner and Kasper (2005).

1.5.3 Lucky Imaging

The turbulent nature of atmospheric seeing does not only result in a steady change of the observed speckle patterns. Also the total strength of the wavefront aberrations varies over time, and with it the image quality. Lucky Imaging exploits this fact by selecting only the best, least distorted images from large sets of short-exposure frames. The selection process requires the availability of a pointlike reference object, e.g. a star, in each image to determine the image quality. The high-quality images are then registered and combined to generate an improved high-resolution result. In contrast to adaptive optics, Lucky Imaging is a fully passive technique.

In 1978, David Fried published an analytic expression for the "probability of getting a lucky short-exposure image through turbulence" (Fried, 1978). A "lucky" image in the sense of Fried has a Strehl ratio of ≥37%, corresponding to a total wavefront variance of less than one rad^2 over the telescope aperture. This probability depends on the ratio of telescope diameter D over the Fried parameter r_0, and can be approximated by:

$$P \approx 5.6 \exp\left[-0.1557\left(\frac{D}{r_0}\right)^2\right] \tag{1.20}$$

Under a 1″ V-band seeing, the corresponding r_0 at 500 nm is approximately 10 cm. The "good-image-probability" computed from Fried's formula above would be 0.0027 at a 70 cm telescope. In a series of e.g. 10000 frames one would hence expect 27 "lucky exposures". This does not sound very promising, but one should keep in mind that this number of 27 images refers to a Strehl ratio of >37% at an angular resolution of 200 mas – this is exactly what one would get with a full adaptive optics system in the H-band at a 2−3 m telescope.
Still, the single frame exposure time has to be short enough to "freeze" the atmospheric turbulence, i.e. shorter than the speckle coherence time introduced in Section 1.4.2. At a typical value of 5−10 ms in the V-band, the total effective integration time of the 27 lucky exposures would be only 135−270 ms. This is indeed very short, but might be already fully sufficient to image bright, close double stars for astrometric purposes.

In practice there is no limitation to use only the images with a Strehl ratio >37%. Depending on the ratio of D/r_0, using the best 1% or even 10% of several thousand short exposures might still allow a substantial improvement of image resolution and Strehl ratio compared to a seeing limited long-time exposure.
Figure 1.7 shows histograms of the Strehl ratios in short exposure frames, simulated for observations with a 2.2 m telescope under a V-band seeing of 0.″7 – quite a typical combination for the conditions at professional observatory sites. These histograms were simulated for different filter passbands, corresponding to different Fried parameters r_0. Since r_0 depends on the wavelength with $r_0 \propto \lambda^{6/5}$, observing at longer wavelengths results in smaller values of D/r_0, thus a higher probability for a lucky exposure. The Strehl ratios for the histogram calculation were measured in simulated short-exposure speckle images by determining the ratio of peak flux over total flux of a single star. This value, the so-called Pseudo-Strehl, was converted to the true Strehl ratio by dividing it by the Pseudo-Strehl of a diffraction limited image with the same simulated telescope diameter, wavelength, and pixel scale. All simulations were performed with the CAOS software package (Code for Adaptive Optics Systems, Carbillet et al. (2005)).

For a V-band seeing of 0.″7, the Fried parameter in this filter is ≈17 cm, already 31 cm in the I-band, and 92 cm in K-band. This corresponds to values for D/r_0 of 12.6, 7.0, and 2.4, respectively, at a 2.2 m telescope. If these values are inserted into equation 1.20, the lucky exposure probabilities turn out to be $9{\cdot}10^{-11}$ in V-band, 0.0027 in I-band, and 2.32 in K-band. Obviously, a probability larger than 1 is nonsense, and equation 1.20 is indeed only valid for D/r_0>3.4.
The numbers for the V- and I-band match the simulations quite well. None of the 20000 V-band speckle images that were generated for the histogram plot had a Strehl ratio larger or equal than 0.37. In the I-band, 61 out of 20000 fulfilled this criterion, compatible with the predicted value of 54 if a Poissonian error of 7 is assumed. Such histogram simulations have been performed by Tubbs (2003) for a range of D/r_0 combinations, confirming that equation 1.20 predicts the probability of lucky exposures correctly for D/r_0>4.5.

All histograms show an exponential tail towards the high-Strehl regime. If the image selection

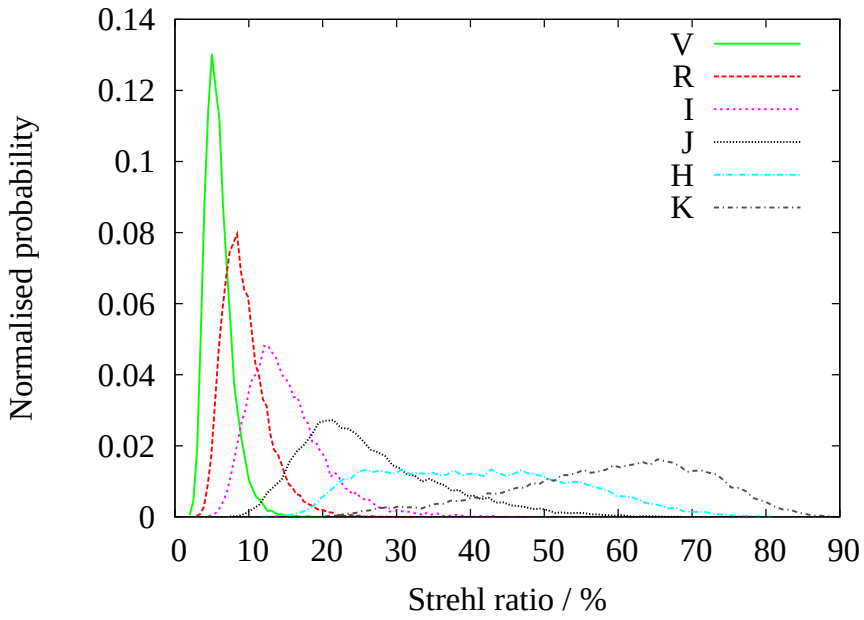

Figure 1.7. *Histograms of Strehl ratios in short exposure frames. The simulations were performed for a V-band seeing of 0.″7 at a 2.2 m telescope. This corresponds to values for the Fried parameter r_0 of 17, 23, 31, 47, 65, and 92 cm in the V, R, I, J, H, and K-band.*

is not restricted to Strehl ratios better than 37%, the number of useable images increases rapidly. For example, selecting the best 5% of all *I*-band images will result in a mean Strehl ratio of ≈21% – a factor 10 better than in the seeing limited case. If this selection was based on 10000 frames with 30 ms single frame exposure time, the effective integration time of the Lucky Imaging result would be 15 s. At a telescope with 2.2 m diameter, and with such a high Strehl ratio, it would be easily possible to detect stars as faint as I=18 mag.

One may ask if there is an ideal combination of telescope diameter, seeing, and filter bandpass for Lucky Imaging. It has been shown by Hecquet and Coupinot (1985) that the so-called "Strehl resolution" $\mathcal{R}$ reaches its maximum at D/r_0=7 if the best 1% of short exposures are selected. The Strehl resolution is defined as

$$\mathcal{R} = \frac{\pi S}{4}\left(\frac{D}{\lambda}\right)^2 \tag{1.21}$$

where S is the resulting Strehl ratio and D the telescope diameter. The Strehl resolution is a measure for the image quality, including both the Strehl ratio and the image resolution, roughly corresponding to terms like contrast and sharpness. Both higher and lower values for D/r_0 than the supposed optimal value of 7 lead to a loss of image quality. If the telescope diameter is increased at a fixed r_0, equivalent to fixed wavelength and seeing conditions, then the probability for a lucky image will decrease, leading to a smaller resulting Strehl ratio. If the telescope diameter is *de*creased, the higher resulting Strehl ratio is achieved at the cost of image resolution.

Figure 1.8 illustrates what is meant with the above considerations. The bottom row shows simulated lucky exposures of a binary star with an angular separation of 150 mas. These images are the best single short exposures from a set of 20000 frames, generated for the *V*, *I*, and *K*-band in a *V*-band seeing of 0.″7 at a 2.2 m telescope. The top row shows diffraction limited images of the same object. While the *V*-band image has the highest image resolution, its Strehl ratio is

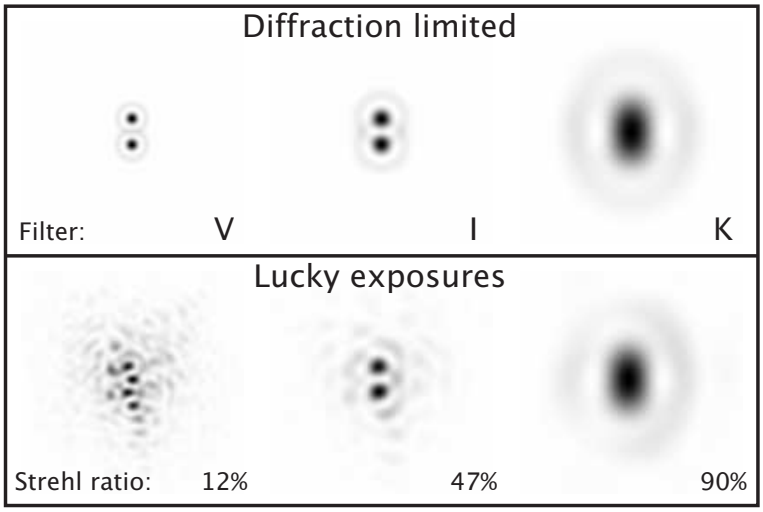

Figure 1.8. *A simulated binary star with 150 mas angular separation and equal component brightnesses. The top row shows diffraction limited images at a 2.2 m telescope in the V, I, and K band. The bottom row contains the best single frames, selected from 20000 short exposures in a V-band seeing of 0.″7.*

only 12%. Though this is not too bad, there is no dominant brightest speckle for each component in this image. The selection and combination of many of such exposures would result in a very noisy image with a strong speckle halo around the binary.
The *K*-band image on the right is just the opposite. At a Strehl ratio of 90% it is almost diffraction limited, with a clearly visible diffraction ring and no additional speckles around the object. But: the theoretical resolution of a 2.2 m telescope in *K*-band is only 250 mas, almost twice the separation of the binary system. This image would not be very useful for astrometric purposes.
The *I*-band image with D/r_0=7 is just in between these two extremes. The binary system is clearly resolved and the surrounding speckles are much fainter than the central peaks. The diffraction rings around the two components are partially visible.

At values for D/r_0 below ≈4, like in the *K*-band example, tip-tilt image motion is the dominating source of any remaining blurring effects in long-time exposures. In this case, the diffraction limit of a telescope can be fully recovered by registering and adding many short exposure frames or by correcting image motion in real-time with a tip-tilt mirror (e.g. Christou, 1991; Close and McCarthy, 1994).

To achieve high image resolution and an acceptable Strehl ratio at the same time, Lucky Imaging should be performed at values of $D/r_0 \approx 7$. This corresponds to an optimal observing wavelength of 800−1000 nm for most medium-sized telescopes at professional sites. The most widely used photometric bands in this regime are the Johnson/Cousins *I* and the SDSS z' filters, with effective wavelengths of ≈850 nm and ≈910 nm. For a 2.2 m telescope, as it is operated by MPIA at Calar Alto and La Silla, a *V*-band seeing of 0.″7−0.″8 would be required to meet the D/r_0 criterion. Though the seeing at e.g. Calar Alto has a median value of 0.″9 (Ziad et al., 2005), conditions are frequently good enough to allow effective Lucky Imaging at this site.

Since the Fried parameter depends on the wavelength with $r_0 \propto \lambda^{6/5}$, all statements above as well as the example images and Strehl ratio histograms can be scaled to other combinations of filter, telescope and seeing. A telescope with only 70 cm diameter, like it is available at MPIA

on Königstuhl mountain, could be used for Lucky Imaging in the *I*-band under a seeing as bad as 2−2.″5 – a typical value at this site. Telescopes larger than 2−3 m would need superb seeing conditions to provide reasonable Lucky Imaging results. Alternatively, observations could be performed at longer wavelengths, e.g. in the *J*-band at 1.2 μm.

Though the concept of Lucky Imaging has been published almost thirty years ago, professional astronomers did not care much about the potential benefits until recently. The reason for that are the short exposure times needed for success. At typical values of 10−50 ms, only bright stars provide enough signal to be detectable with the commonly used CCD cameras. While modern CCD chips provide quantum efficiencies of more than 90%, the noise that is added during the readout phase renders Lucky Imaging of sources fainter than V≈10 mag impossible. As explained at the beginning of this section, the quality of each single frame has to be measured on a reference object, preferably a star. Since the highest quality images are most efficiently selected by determining the Strehl ratio of the reference, this star has to be detected with a sufficient signal-to-noise-ratio to allow a reliable measurement of the peak value and total flux – the ingredients for Strehl ratio calculation.
In addition, most CCDs are not capable of acquisition rates higher than one or two frames per second – but typically several thousand frames are necessary for successful Lucky Imaging, demanding a high speed camera.
Actually, amateur astronomers have applied the Lucky Imaging technique for almost a decade by using standard webcams at small telescopes. Their high resolution images of the moon and the brighter planets can be frequently admired in astronomical magazines.

With the advent of high-speed, low-noise cameras, Lucky Imaging of faint sources, using faint reference stars, has experienced rapid progress and raised considerable interest among professional astronomers. First experiments with electron multiplying CCDs (EMCCD, see Chapter 3.2) by Baldwin et al. (2001), Tubbs et al. (2002), and Tubbs (2003) at the 2.5 m Nordic Optical Telescope proved that diffraction limited imaging of faint sources in the *I*-band is possible.
Encouraged by these success reports, own experiments at the MPIA 70 cm and Calar Alto 2.2 m telescope were started in 2006.

1.6 Overview of the Thesis

Chapter 2 describes a simple Lucky Imaging setup at MPIA's 70 cm telescope on Königstuhl mountain and summarises the early results of double star observations.

The design of AstraLux, a dedicated Lucky Imaging instrument for the Calar Alto 2.2 m telescope, is presented in Chapter 3. This includes a full characterisation of the detector and an introduction to electron multiplying CCDs (EMCCD).

Chapter 4 outlines the data reduction pipeline that is used both for on-site generation of Lucky Imaging preview results as well as for offline post-processing of the observations.

The performance of the instrument at the telescope is summarised in Chapter 5. The dependency of the achievable Strehl ratio and image resolution on seeing conditions and wavelength is investigated. Examples of double star and globular cluster observations are used to determine temporal and spatial coherence characteristics of the Lucky Imaging data.

Chapter 6 is dedicated to the astrometric calibration of AstraLux. The instrumental stability and

the (dis)advantages of using double stars and globular clusters as calibrators are discussed. Specific recommendations for efficient calibration are given to guide potential users of the instrument in planning their observing strategy.

The scientific observing programmes that were started already during the first observing run in July 2006 are summarised in Chapter 7.

Chapter 8 is an extended version of the first publication that has emerged from AstraLux observations. The close binary HD 160934 was discovered with AstraLux in July 2006. Additional Hubble Space Telescope archive data and unresolved photometric measurements at the MPIA 70 cm telescope allowed a tentative physical characterisation of this system.

Chapter 2

Lucky Imaging with a Conventional CCD

2.1 Introduction

As a first approach to the Lucky Imaging observing technique and the reduction of Lucky Imaging data, test observations with a conventional laboratory CCD camera were conducted in January 2006 at MPIA's 70 cm telescope on Königstuhl mountain. The typical V-band seeing at this site in winter is $3-4''$, but occasionally $2''$ can be reached. Though this is considerably worse than the average $0\farcs6-1\farcs0$ usually expected at professional observatory sites, it matches the fact that the 70 cm telescope is much smaller than the telescopes in these locations – e.g. the Calar Alto 2.2 m telescope's primary is 3.1 times larger in diameter. As the crucial number for successful Lucky Imaging is the ratio of telescope diameter over r_0, it is possible to scale the results obtained at the 70 cm telescope to other setups with larger apertures and better atmospheric conditions. Results from observations under a seeing of $2\farcs5$ with this instrument are in principle comparable to what can be expected at the Calar Alto 2.2 m telescope in a typical $0\farcs8$ seeing, if the temporal aspect of atmospheric turbulence is left aside.

The instrumental setup and the very first experiences with the Lucky Imaging observing technique at MPIA are briefly summarised in the following.

2.2 Instrumental Setup

2.2.1 The Camera

The camera used in these first experiments was a DVC-1412 from DVC Company, Austin, Texas. This model is based on a Peltier-cooled 1392×1040 pixel, front-illuminated interline CCD chip with a physical pixel size of 6.45×6.45 µm. The peak quantum efficiency is ≈60% at 550 nm, dropping to ≈25% at 800 nm and ≈11% at 900 nm. In the standard configuration, the camera is equipped with a C-mount thread, including an IR-blocking filter. This filter was removed prior to the observations. Connection to a control computer – a normal Linux PC – is established via a CameraLink interface. The basic properties of the system are listed in Table 2.1.

Exposure times are defined by electronic shuttering. Depending on the internal timing mode of the control electronics, integration times as short as 93 µs and as long as 102 s can be realised.

Table 2.1. *Basic properties of the DVC camera and the MPIA 70 cm telescope*

DVC-1412 CCD Camera			
Chip size:	8.98×6.7 mm	*Chip type*:	Interline
Chip model:	Sony ICX285		
Pixels:	1392×1040	*Pixel size*:	6.45×6.45 µm
QE@550nm:	62%	*QE@650nm*:	53%
QE@750nm:	34%	*QE@850nm*:	16%
Readout frequencies:		2.25, 4.5, 9, and 18 MHz	
Readout noise at 9 MHz:		6 e^-	
Readout noise at 18 MHz:		9.5 e^-	
Pixel scale at the MPIA 70 cm telescope:		0.″238 / px	
Field of view at the 70 cm telescope:		5.′5×4.′1	
The MPIA 70 cm Cassegrain Telescope			
Primary ⌀:	0.70 m	*Secondary ⌀*:	0.27 m
Focal length :	5.6 m	*Focal ratio*:	f/8
Usable field of view:		≈ 20’ diameter	
FWHM of diffraction limited PSF at λ=650nm:		0.″195	

Exposure time, bias level, and gain factor can be set with a command line software tool.
In principle, frames rates of several 10 Hz are possible by reading out only subarrays of the chip, but the actually reached maximum value during the observations was ≈12 Hz due to software limitations.

2.2.2 Telescope and Filters

The MPIA telescope in the eastern dome of the Elsässer laboratory is a Cassegrain system with a primary mirror diameter of 0.7 m and a focal length of 5.6 m. A telescope control system based on incremental encoders allows manual pointing with an accuracy of typically 10′. This uncertainty is approximately twice the size of the field of view (FOV) of the DVC camera and would have severely complicated target acquisition. In order to allow efficient observing, a telescope pointing model was developed, calibrated, and applied as part of the preparatory work for this thesis. The model reliably reduced the residual pointing error to less than 1’. It is briefly described in Appendix A.

During normal operations the telescope is equipped with a manual filter slider and a 2k×2k liquid-nitrogen cooled, thinned, and back-illuminated CCD for scientific observations. The maximum frame rate of this camera is ≈1 Hz at a pixel scale of 0.″55/px. Though the high sensitivity of the camera would have been very beneficial, the low frame rate and the gross undersampling of the theoretical PSF made it unsuitable for Lucky Imaging observations.

Mechanical and optical constraints did not allow to mount the DVC camera behind the filter slider. Instead, a single filter was mounted in the flange connecting the camera to the telescope. At the time of the observations, a set of Johnson/Cousins *UBVRI* filters was available. Due to the limited quantum efficiency of the camera towards longer wavelengths, the *R* filter was used for most observations, and only very bright targets could be acquired through the *I* filter.

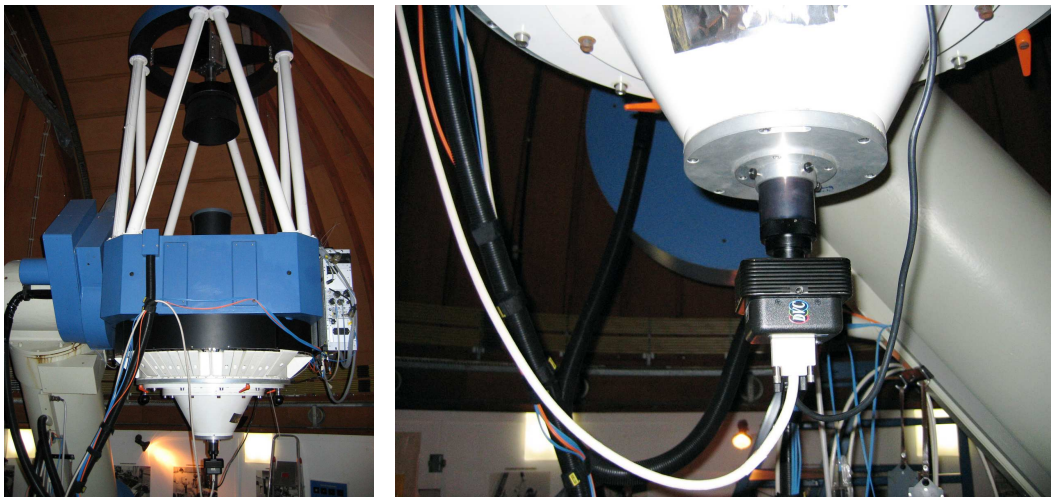

Figure 2.1. *The MPIA 70 cm telescope on Königstuhl mountain and a closeup of the DVC camera attached at the Cassegrain focus.*

The filter design and filter curves are given in Appendix B. Figure 2.1 shows the telescope with the mounted DVC camera, whereas Table 2.1 contains a short overview of the telescope characteristics.

2.3 Observations

All observations were carried out in January 2006. While the first experiments on January 23−24 were hampered by a seeing as bad as 5″, values down to 2″ were attained on January 30−31. Test observations of the star $\alpha\,Ari$ in the *I*-band showed, that the camera's quantum efficiency did not allow single frame exposure times shorter than 500 ms even for this bright ($V \approx 2$ mag) object at wavelengths >800nm. For this reason, all following observations were performed in the *R* band, with exposure times of 250 ms for all objects.

Focusing was achieved by taking test exposures with typical integration times of 5 s. A large fraction of the observing time was spent on checking for focus-drifts and on test acquisitions of fainter objects like the Orion Trapezium or globular cluster centres. Here the term 'faint' actually refers to their appearance when looked at with our setup. While the Orion Trapezium could have been imaged with exposure times of >500 ms, useful data was only obtained for the objects listed in Table 2.2.

2.4 Data Reduction

The raw data, typically 5000 single FITS files, was reduced in a very simple approach compared to the AstraLux pipeline as it is today. The reduction steps largely follow the prescription of Tubbs (2003), but in our case no noise filtering was applied.

After automatically locating the star in each single image, a subarray of 64×64 pixels, corresponding to 15″×15″, was extracted around the intensity's center of weight. The outermost columns and rows were used to estimate and subtract the sky background and bias. The subarray

Table 2.2. *Log for the January 2006 test observations at the MPIA 70 cm telescope*

Object name	UTC	Nr. of frames	Integration time [ms]	Filter
23 January 2006				
α Ari	18:23	5000	242	*I*
α Ari	18:43	5000	534	*I*
α Ari	19:03	5000	952	*I*
α Ari	19:21	5000	100	*I*
α Ari	19:54	5000	100	*R*
α Ari	20:13	5000	250	*R*
24 January 2006				
6 Tri	20:49	5000	250	*R*
30 January 2006				
HD 37098	19:44	10000	250	*R*
SAO 25938	20:33	10000	250	*R*
31 January 2006				
WDS 01535+1918	18:56	7500	250	*R*
PPM 000697	19:47	6000	250	*R*

was Fourier-resized by a factor of four (see Chapter 4.3.2 for an example of Fourier-resampling). The peak flux in a circular aperture of 3.″8 diameter (or 64 pixels in the resampled image) was divided by the total flux within this aperture to determine the "Pseudo-Strehl", i.e. a number that should be linearly related to the actual Strehl value. This value was finally used to select the best images of each set.

The processed result was obtained by resampling all images with Pseudo-Strehl values above a chosen cutoff value, registering them by integer-pixel shifting with the brightest pixel as reference position, and averaging them. The resampling lead to a pixel scale of 60 mas in the reduced images, which provided proper spatial sampling in the *R* band (the effective wavelength in the setup was ≈650 nm, resulting in a FWHM of the diffraction limited PSF of ≈195 mas).

A seeing limited image was simulated by averaging all frames, regardless of their quality. To compensate telescope tracking errors, the frames were divided in subsets corresponding to an observing time of ≈1 min. Each subset was averaged without applying pixel shifts, and this intermediate results were registered before the final averaging step.

2.5 Results

Observations in the first two nights suffered from seeing values of ≈5″, derived from measuring the FWHM of stars on the focusing exposures. At λ=650 nm this seeing corresponds to r_0≈2.7 cm, equivalent to D/r_0 of nearly 26. The probability for getting a diffraction limited exposure is effectively zero, according to Equation 1.20. Still, Lucky Imaging can provide image quality improvements under such conditions as illustrated in the example of 6 *Tri* in Figure 2.2. This wide binary with a separation of 3.″9 and component brightnesses of *V*=5.3 and *V*=6.7, respectively, is not resolved in the seeing limited image, though the PSF appears slightly elongated.

The best single image already shows the binary nature of this star, although the PSF is heavily distorted. Using the best 5% of all 5000 frames leads to a resolved image with a stellar FWHM of ≈1.″4. While this is still a factor of seven worse than the theoretically possible value, it is also 3.6 times smaller than the natural seeing.

The nights of January 30−31 provided much better atmospheric conditions, with seeing values ranging between 2″ and 3″. The 1″ separated binary HD 37098 with nearly equal component magnitudes of V=6.5 was observed under 2.″5 seeing, and the results are shown in Figure 2.3. While the seeing limited image provides no hint to the star's binary nature, it is clearly resolved in the Lucky Imaging result, with a stellar FWHM of only 430 mas. This is more than two times worse the theoretical resolution, but almost a factor of six better than the seeing limited value. The corresponding D/r_0 for this observation was 12.8, still considerably higher than the supposed optimal value of 7.

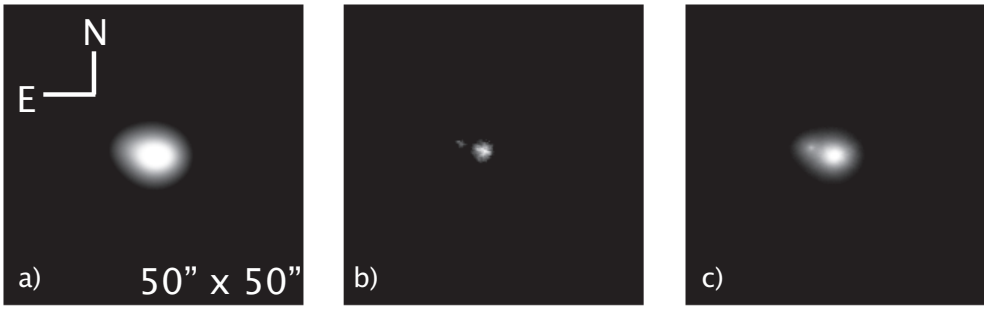

Figure 2.2. *Observations of the 3.″9 separated binary 6* Tri. *The simulated seeing limited image* ***(a)*** *to the left has a stellar FWHM of ≈5″. The middle and the right images* ***(b, c)*** *show the best single frame and the Lucky Imaging result using the best 5% of all 5000 images. All images are displayed on a logarithmic scale.*

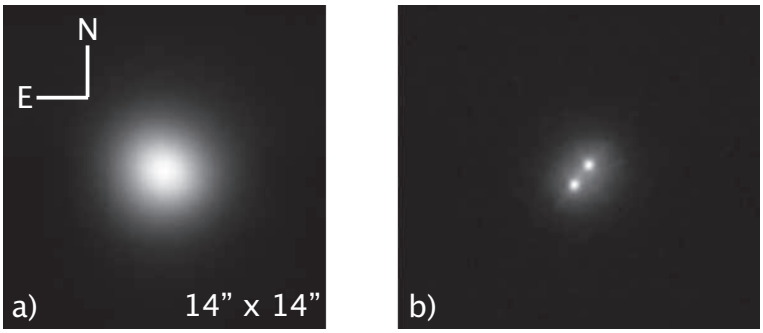

Figure 2.3. *Observations of the 1.″0 separated binary HD 37098.* ***a)*** *Simulated seeing limited image with a stellar FWHM of ≈2.″5.* ***b)*** *Lucky Imaging result, generated from the best 2% of all 5000 images.*

The reduction of other double star observations under comparable seeing conditions lead to similar results. While the diffraction limit could not be reached in any case, a remarkable improvement of the image resolution in terms of FWHM of the stellar PSF was always observed.
Despite the low sensitivity of the camera, the undersampling of the theoretical PSF, and the unfavourable seeing conditions, this test observations indicated that the Lucky Imaging technique can provide improved image resolution with a minimum of hardware and software effort.

Chapter 3

The AstraLux Instrument

The encouraging results of the 70 cm telescope test observations triggered the decision to build a dedicated Lucky Imaging instrument for the Calar Alto 2.2 m telescope. This chapter summarises the key requirements that determined the final design, gives an overview of the instrument's components, and includes a characterisation of the AstraLux camera.

3.1 Design Constraints

The constraints that had to be considered during instrument design were partly dictated by the available time and infrastructure, but may to some extent apply to any Lucky Imaging instrument in general. They are summarised in the following to give a guideline for anyone intending to build a similar instrument, and to make the component selection more transparent.

Sensitivity and Speed

The early experiments at the 70 cm telescope demonstrated that a conventional, back-illuminated CCD does not provide enough sensitivity to observe objects other than the brightest double stars. The final camera should have a high quantum efficiency up to long wavelengths and a readout noise as low as possible. At the same time it should be capable of short exposure times down to a few ten milliseconds, with duty cycles as high as possible. This narrows down the range of suitable detector types to frame transfer or interline, thinned, and back-illuminated CCDs. These provide high frame rates with nearly zero dead-time between consecutive frames and run at typical pixel clocks of several MHz. On the other hand, high readout frequencies cannot be achieved without increasing the readout noise. A way out of this is the choice of electron-multiplying CCDs (EMCCD), where the photoelectrons are multiplied via impact ionisation before they enter the readout amplifier.

Spatial Sampling

Since the ultimate goal of Lucky Imaging is to reach the diffraction limit of the telescope, proper sampling of the theoretical PSF should be provided. 'Proper sampling' means in the first instance

that the Nyquist criterion should be fulfilled, i.e. the theoretical FWHM should cover at least 2 pixels on the detector. Depending on the physical CCD pixel size and the resulting pixel scale at the chosen telescope, magnification by a fore-optics may be necessary.

Stability

Stability in the sense of a rugged mechanical construction is important for instruments that should produce reliable astrometry, e.g. allow precise measurements of angular separations and position angles of binary stars. An unstable instrument requires more calibration effort, resulting in larger overheads. In the worst case, unstability will lead to larger measurement uncertainties and less reliable data. A design without any moving parts – at least where they are not absolutely necessary – is probably the best option.

Development Time

The fact that this project had to fit within the timeframe of a diploma thesis put a firm constraint on the selection of the hardware components. For example, one year is probably not enough time to develop and test a CCD camera, so buying one "off-the-shelf" is the preferred solution. The same holds for optics and camera mount. If these parts can not be readily bought from a supplier, but have to be manufactured in-house, their design should be restricted to a baseline as simple as possible. This implies that the final instrument might be less flexible than a full-grown system, e.g. it might be impossible to easily change the field of view during operation, or to access the pupil plane for experiments with aperture masking techniques.

3.2 The EMCCD Principle

The CCD cameras usually found at astronomical telescopes provide high sensitivity in terms of quantum efficiency, low dark current, and low readout noise in the order of a few electrons. Readout times are – depending on the detector size – in the range of tens of seconds, defined by the number of pixels that have to be read and the readout clock. Speeding up the readout process by increasing the pixel readout frequency is principally possible, but cannot be achieved without accepting higher readout noise at the same time. Depending on the readout electronics, noise of several $10\,e^-$ is typical for readout clocks in the 10 MHz regime. A camera with such high noise can obviously not be used in applications where the average photon flux per frame and pixel is in the order of a few photons – but this is exactly the case for Lucky Imaging, where exposure times of few ten milli-seconds are typical.

Electron multiplying CCDs implement an elegant workaround for this problem. Rather than using external image intensifiers in front of the camera or special low-noise (and hence expensive) readout electronics, these cameras can multiply each single photoelectron on-chip by a factor of 1000 or more (e.g. Jerram et al., 2001; Hynecek and Nishiwaki, 2002). This is accomplished by using a special readout register rather than modifying the sensor area of the CCD. The major difference between this electron multiplication (EM) register and a standard readout register consists in the applied clock voltage levels. While conventional readout registers use voltages of ≈ 10 V, the EM register is typically operated at $30-50$ V. Under these conditions the electrical

field in the register is high enough to provide a small probability for impact ionisation to occur. Each time an electron is clocked to the next register cell, it will produce a secondary electron in typically 1% of clock cycles. Since electron multiplication registers usually consist of several 100 multiplication stages, even this small probability of μ=0.01 will result in appreciable total gains of $g=(\mu + 1)^s$, where s is the number of register cells. This results in high signal-to-noise ratios (SNR) even for single photons: if one photon generates 1000 electrons in total, it can be easily detected even if the readout amplifier adds a noise of 100 e^- to the output signal. This allows to operate the readout electronics at high pixel clocks, with high readout noise.
If an electron multiplication register is combined with a frame-transfer CCD that allows integration during readout, high speed cameras with high duty cycles and single-photon detection capability can be built. Figure 3.1 illustrates the layout of such an electron multiplying frame transfer CCD.

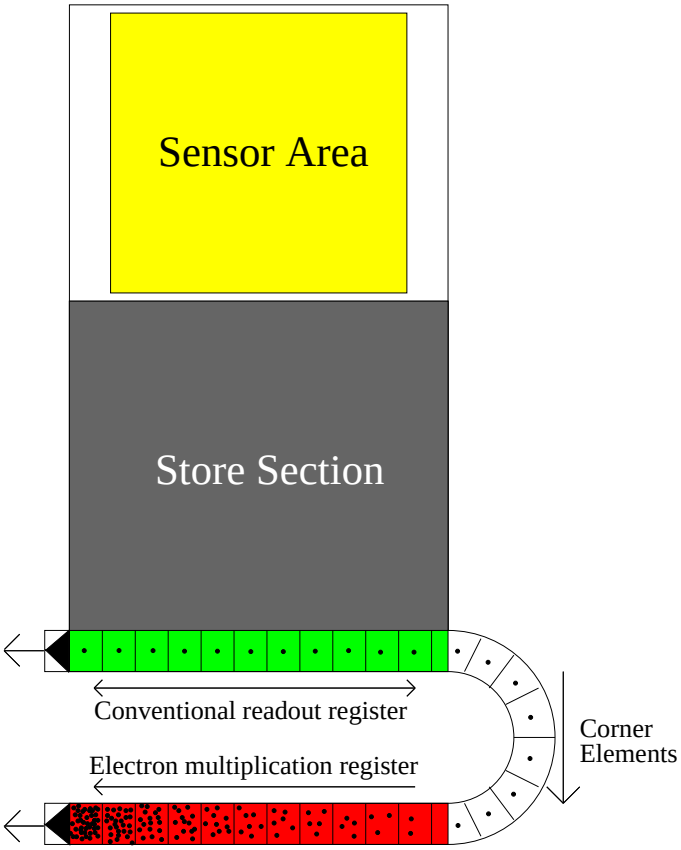

Figure 3.1. *Schematic layout of a frame transfer CCD with conventional and electron multiplying amplifier. Photoelectrons are vertically shifted from the sensor area into the store area at the end of an integration cycle. While the next frame is acquired, the image from the store area can be read out either through the conventional horizontal register (green) or the electron multiplication register (red). The two registers are connected by corner elements, and the horizontal readout direction is reversed to switch between the two outputs.*

The multiplication process itself and the fact that single photons (or better: single electrons) will be detectable with an EMCCD are the reason for important differences between the noise characteristics of a conventional and an electron multiplying CCD. The knowledge of these peculiarities is essential for effective EMCCD operation.

3.2.1 Noise Factor

The total electron multiplication gain is the result of a stochastical process. The random nature of the impact ionisation will multiplicatively increase the overall noise budget.
For a total electron gain g and a probability μ for the impact ionisation process, this so-called

noise factor F is given by Robbins and Hadwen (2003) as:

$$F^2 = \frac{1}{g}\left(\frac{2g + \mu - 1}{\mu + 1}\right) \tag{3.1}$$

At typical overall gains of several hundred and an impact ionisation probability of $\mu \sim 0.01$, the noise factor tends to $\sqrt{2}$.
The signal-to-noise ratio for the detection of S_{ph} photoelectrons per pixel in a single frame with a non-multiplying CCD is given by:

$$SNR_{\mathrm{conv}} = \frac{S_{\mathrm{ph}}}{\sqrt{S_{\mathrm{ph}} + S_{\mathrm{dark}} + \sigma^2}} \tag{3.2}$$

Here S_{dark} is the dark signal and σ^2 is the CCD's readout noise. In the case of an electron-multiplying CCD, the noise factor will affect both the signal related to photon detections and dark current. But at the same time the electron gain will decrease the effective readout noise:

$$SNR_{\mathrm{EMCCD}} = \frac{S_{\mathrm{ph}}}{\sqrt{F^2 S_{\mathrm{ph}} + F^2 S_{\mathrm{dark}} + \frac{\sigma^2}{g^2}}} \tag{3.3}$$

The decrease of the SNR due to the noise factor will be more than compensated by the reduction of the readout noise – but only in the low flux regime. If the contribution of the dark current is neglected, an electron multiplying CCD with $g \gg 100$ and a readout noise of $\sigma = 100\,\mathrm{e}^-$ will perform better than a conventional CCD with the same readout noise only for signals below 10000 photoelectrons. Above this intensity level, the electron multiplication will in fact lead to a worse SNR. This shows that EMCCDs are not meant to be used in other than low-light conditions. For this reason, most available EMCCD cameras today are equipped with both an electron multiplying and a conventional readout register, allowing to choose the appropriate mode for a given illumination level. It should be noted that a dark current of $0.005\,\mathrm{e}^-$/pixel/frame will have the same impact on the SNR as the effective readout noise in this example. This implies that EMCCDs should be properly cooled to get the best possible noise performance.

3.2.2 Clock Induced Charges

The term Clock Induced Charges (CIC) denotes charges that are not produced by incoming photons, but during the clocking of a pixel or pixel row to the next position[1]. Physically, CICs are produced by impact ionisation of holes as they move in and out of the Si/SiO_2 interface during clocking (Jerram et al., 2001). This occurs even with normal clocking voltages, thus this feature is in fact common to all CCDs. Only the electron multiplication gain of EMCCDs allows the detection of such events in the final image. The probability for CIC generation depends on the clocking voltage, the duration of the clock pulse and the pulse shape. In EMCCDs, they are mostly produced during vertical shift operations, but also in the horizontal shift registers as the EM register itself. Since there is no way to distinguish the signal attributed to a CIC from that of an incident photon, the CIC probability sets a limit to the single photon detection capability. In Equation 3.3, the CICs can in principle be treated like the dark current. For SNR calculations it is therefore convenient to use a combined background event probability that includes both CICs and dark current.

[1] Actually, not the pixels but only the charges in them are moved during the clocking.

3.2.3 Single Photon Detection

Single photons can be detected if the electron gain g is high compared to the readout noise σ of the camera. Tubbs (2003) gives the following formula for the fraction of photons correctly discriminated from the noise with 5σ confidence in the absence of CICs and dark current:

$$f = \exp\left(\frac{1-5\sigma}{g-\frac{1}{2}}\right) \tag{3.4}$$

For our example system with g=1000 and σ=100 e^-, this fraction would be f=0.61. At a gain of g=2500, this value increases to f=0.82. If a sufficient single photon detection performance can be reached and the average photon flux is well below 1 photon/pixel/frame, a simple thresholding scheme can be used to operate an EMCCD as a pure photon counting device. In this case, the noise factor F will not have any impact on the SNR anymore (Daigle et al., 2004). It is possible to reduce the effective noise factor for fluxes up to 20 photons/pixel/frame without introducing non-linearities due to coincidence losses (Basden et al., 2003).

3.3 The AstraLux Camera Head

3.3.1 Overview

The AstraLux camera head is an Andor DV887-UVB model from Andor Technologies, Belfast, Northern Ireland (see Figure 3.2). It is an electron-multiplying, thinned, and back-illuminated 512×512 pixel CCD that comes as complete package with a multi-stage Peltier cooler, mechanical shutter, computer interface and software. It can be operated with readout clocks of up to 10 MHz in frame transfer mode, allowing a full frame rate of 34 Hz. Using subarrays, binning, and short vertical shift times allows frame rates of more than 1 kHz. These short exposure times are realised by electronic shuttering, whereas the mechanical shutter is only used for bias and dark frame acquisition and to protect the CCD window against dust.
Critical parameters like electron gain, analogue gain, readout clock, and vertical shift pulse duration and voltage can be changed via the control software.
Starting at room temperature, the typical operating temperature of −75°C is usually reached within 20 minutes. The camera requires neither refill of liquid coolants nor any action to maintain the vacuum inside the CCD head.

Figure 3.2. *The AstraLux DV887-UVB camera head. The connectors for optional water cooling, external triggering, power supply and data transfer are visible on the left side of the camera housing.*

Table 3.1. *Andor DV887-UVB camera head properties*

CCD type:	E2V CCD97 electron multiplying, frame transfer, back-illuminated, thinned and UV-sensitised CCD
CCD size:	Sensitive area with 512×512 pixels; pixel size 16×16 μm^2; chip size 8.192×8.192 mm^2
Cooling:	3-stage Peltier cooler, down to −75°C without liquid coolants
Readout registers:	Conventional and 536 stage electron multiplication register
Electron gain:	Up to 2500 at −75°C CCD temperature, adjustable in 255 steps
Readout clocks:	1, 3, 5, and 10 MHz
Vertical shift times:	0.4, 0.6, 1.0, 1.8, 3.4, and 6.6 µs. Clock pulse voltage adjustable in 5 steps
Readout noise:	Down to 6 e^- in conventional mode and up to 130 e^- in electron multiplication mode
Readout ADC:	14 bit nominal, ≥13 bit resolution at 10 MHz pixel clock
Full well depths:	190 000 e^- in image area pixels, 800 000 e^- in EM register cells
Dark current:	0.009 e^-/pixel/s at −75°C

The quantum efficiency of the CCD is reproduced in Figure 3.3. A UV coating provides good sensitivity down to wavelengths <300 nm, below the atmospheric cut-off. This is a benefit for *U*-band photometry, but a disadvantage of this feature is a slightly decreased transmission of the camera's entrance window due to the lack of an anti-reflection coating. The decision to use exactly this camera was driven by the instant availability of this model, allowing a fast instrument development. Table 3.1 summarises the most important technical specifications of the camera head.

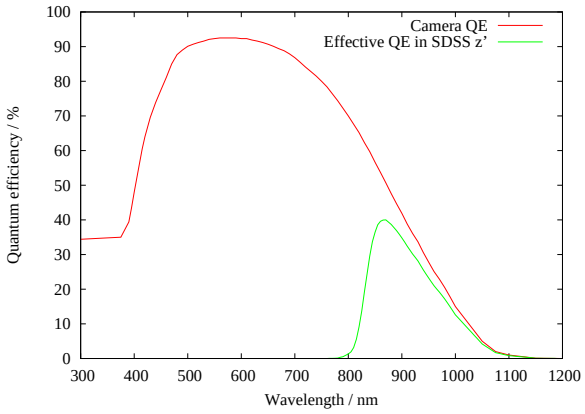

Figure 3.3. *Quantum efficiency of the AstraLux camera head. The camera's QE is plotted in red, and its convolution with the transmission curve of a Schott* RG 830 *filter (used for observations in SDSS z′) in green.*

3.3.2 CCD Characteristics

The Andor DV887-UVB has two different output amplifiers, offers 255 electron gain settings, four readout frequencies, three analogue gain settings, four vertical shift voltage settings and six different vertical shift times. The goal of the characterisation below is not to thoroughly cover the full parameter space, but to give a solid qualitative overview of the impact of the various parameters on the recorded data. Of course, quantitative measurements like analogue gain, electron multiplication gain and readout noise are not omitted.

Table 3.2. *Readout noise and analogue gain of the AstraLux camera. The relative gain refers to the analogue gain at a software gain setting of unity. Nominal values as given by the manufacturer are printed in parentheses where available.*

Pixel clock	Software gain	Conversion factor [e^-/ADU]	Readout noise [e^-]	Relative gain
Conventional amplifier				
1 MHz	1.0	9.21	10.0	
	2.4	3.97	7.0	2.32
	4.6	2.04 (2.07)	5.9 (6.5)	4.51
3 MHz	1.0	9.61	15.5	
	2.4	3.97	10.7	2.42
	4.6	2.08 (2.11)	9.6 (10.5)	4.62
Electron multiplying amplifier at unity electron gain				
1 MHz	1.0	53.1	50.4	
	2.4	22.1	39.7	2.40
	4.6	11.5 (12.26)	22.4 (25.5)	4.63
3 MHz	1.0	53.4	60.9	
	2.4	22.7	38.4	2.35
	4.6	11.9 (12.37)	32.3 (35.4)	4.49
5 MHz	1.0	55.6	95.1	
	2.4	22.7 (24.16)	52.7 (59.8)	2.45
10 MHz	1.0	59.7	135	
	2.4	24.2 (26.25)	80.4 (99.9)	2.47

Readout Noise and Analogue Gain

Readout noise and analogue gain values refer to unity electron gain. They were measured at the typical AstraLux operating temperature of $-75°$C, with 3.4µs vertical shift pulse duration and standard shift voltage setting. Analogue gains were measured in sets of uniformly illuminated images. The readout noise values are based on typically 50 bias frames for each camera setting. Since different authors seem to favour different methods of readout noise and gain determination, Appendix C contains a short description of the algorithms that were used in this work. The results of these measurements are summarised in Table 3.2, both for the conventional and the electron multiplying amplifier. Nominal values taken from the camera datasheet are given where available, but please note that these do not refer to measurements with the same camera system.

The overall impression from the measurements is, that the camera's characteristics are close to the specifications, or even better concerning readout noise[2]. There is a strong dependency of the readout noise on the analogue gain setting, with higher noise at lower gains, indicating that a substantial amount of noise is added by the ADC. The higher gain settings should be preferred whenever the decrease in dynamic range is acceptable.
The readout noise measurements do not include bias structure and bias drift, whereas both effects are important for data reduction. A typical average of 100 single bias frames is presented in

[2]This may be attributed to differences in the applied algorithms. The approach chosen in this work treats readout noise and bias structure separately, whereas this is not known for the values stated by the manufacturer.

Figure 3.4, showing strong column-to-column variations. Figures 3.5 and 3.6 show plots of the row and column averages versus row and column number, respectively, and an FFT analysis of the column signal variations. The row average initially steeply decreases with increasing row number, possibly caused by readout amplifier glow. The column plot and especially the spectral power analysis confirm that the bias structure is dominated by strong column-to-column variations. A possible explanation for this could be timing inaccuracies in the readout electronics, since the amplitude of the bias structure tends to decrease at lower pixel clocks.

The bias structure is unique for each camera setting. Any changes, e.g. choosing a different electron gain or defining a subarray for faster readout, result in a modified bias pattern. Master bias calibration frames have to be generated for each camera setup separately.

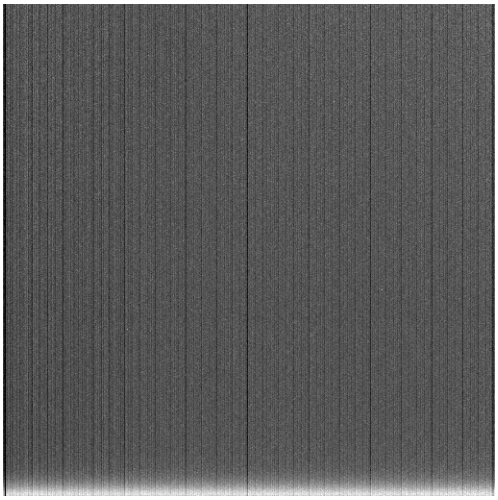

Figure 3.4. *Typical bias frame of the AstraLux camera. The printed image is the mean of 100 dark frames in frame transfer mode, using the electron multiplying amplifier at unity electron gain and a pixel clock of 10 MHz.*

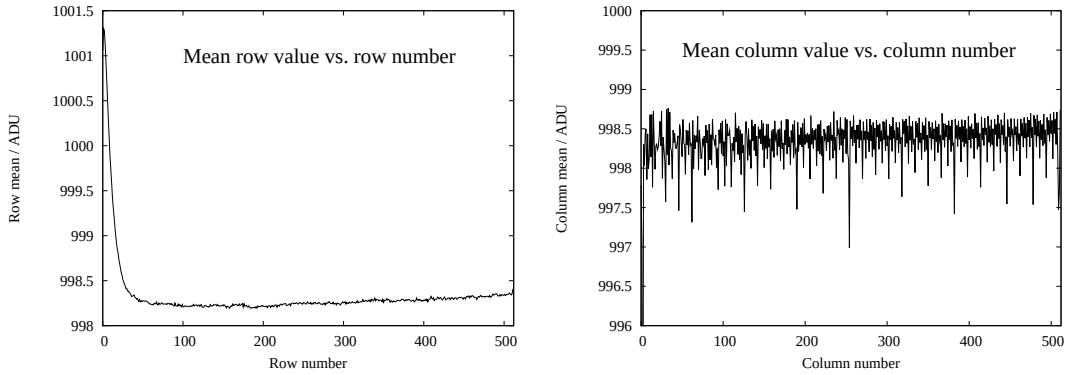

Figure 3.5. *Mean row and column values of the bias frame shown in Figure 3.4.*

Electron Gain

The electron multiplication (EM) gain of the camera can be adjusted by the control software, but the relation between the gain setting and the actual multiplication factor is not linear. Furthermore, the impact ionisation probability has a negative temperature coefficient, i.e. electron multiplication will be more efficient at lower temperatures.
The EM gain of the AstraLux camera was measured at four different temperatures at a pixel clock of 10 MHz by imaging a 5×5 pattern of point sources at different software EM gain settings. The

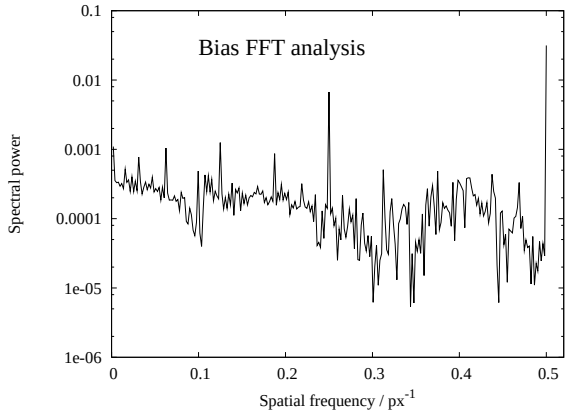

Figure 3.6. *Spatial power spectrum of the average bias frame shown in Figure 3.4. Column-to-column variations are the most prominent feature (spatial frequency 0.5 px^{-1}).*

fluxes of each source at each gain level were extracted by standard aperture photometry. The results are plotted in Figure 3.7, where a gain of unity refers to readout through the EM amplifier, but with normal clock voltages below the threshold for impact ionisation. The maximum gain at T_{CCD}=−75°C is ≈2500 and decreases to ≈500 at −50°C. For electron gains above ∼10 the multiplication factor approximately doubles if the temperature is decreased by 10°C. The measurements clearly indicate that the CCD should be cooled as deep as possible for optimum EM performance.

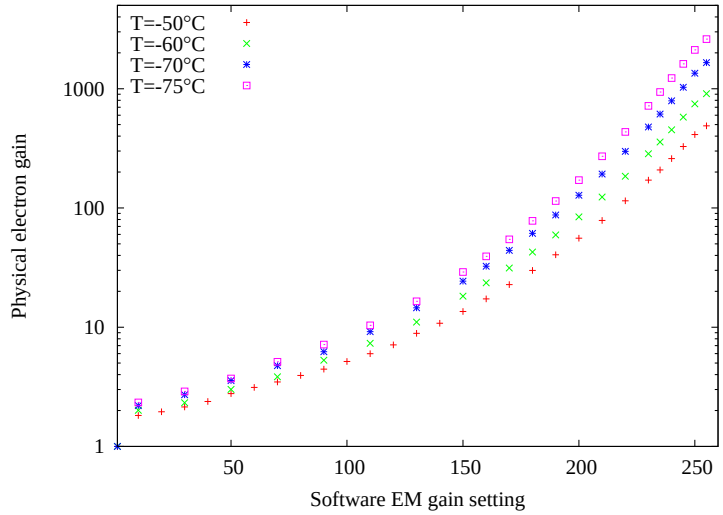

Figure 3.7. *Physical electron gain versus software electron gain setting. Please note that the physical gain is plotted on a logarithmic scale.*

Linearity, Well Depth and Quantum Transfer Efficiency

The standard approach to measure the linearity of a CCD is to image a uniformly illuminated surface at different integration times and to plot the mean image intensity versus the exposure time. Unfortunately, in the case of the AstraLux camera this technique can lead to gross overestimates of the linear range.

Figure 3.8 shows an example for such a measurement. While the mean signal of a 100×100 square pixel area shows perfect linearity up to over 6000 ADU, the linear range actually ends at 4000 ADU as can be seen in a plot of variance versus mean signal. The reason for this strange discrepancy becomes obvious if the flatfield frames used for this analysis are examined visually.

Figure 3.9 shows an image in the linear range at 2000 ADU mean level on the left, and an image with 6000 ADU mean intensity in the middle. While both are supposed to be in the linear range, the middle frame shows strong structure in the form of horizontal, noisy stripes. This noise is responsible for the steep increase of the variance in Figure 3.8. A closer look at these noisy regions reveals that this is largely attributed to pixel-to-pixel variations. Pairs of especially dark/bright pixels can be found everywhere within the affected regions. Apparently, the darker pixels represent small charge traps, where the signal is not fully shifted to the next row within one vertical clocking cycle. The electrons left behind are then attributed to the next pixel position in the column. As the signal is only delayed by one row, this does not change the average value of a larger area.

The data for this example was acquired at a vertical shift time of 0.6 µs. With the chosen camera settings a readout value of 4000 ADU corresponds to ~88000 e^-, whereas the full well depth of the image area pixels is specified as 190000 e^-. But: this specification is only valid at a vertical shift time of 3.4 µs, which is the recommended value for optimal charge transfer efficiency.
Therefore, the end of the linear range of the AstraLux camera strongly depends on the clocking parameters. A shorter vertical shift time will decrease the range, whereas using a higher clock voltage can partly compensate this.
The large scale structure of the noisy stripes in the overexposed frame could be attributed to periodic changes of the vertical clock pulse length or to fluctuations of the physical pixel sizes as a result of the manufacturing process.

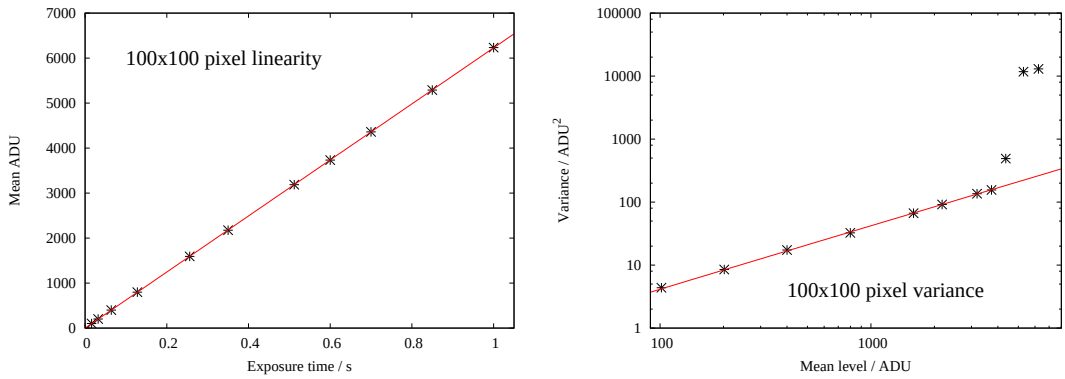

Figure 3.8. *Example linearity plots. While the plot of mean value versus exposure time suggests a large linear range >6000 ADU, the variance-mean relation indicates that the true linear range ends at values around 4000 ADU.*

Further measurements of the linearity were performed with a vertical shift time of 3.4 µs, using electron gains of 1 and ~2500. The linearity was measured in a single pixel to account for effects of charge-trapping.
Figure 3.10 shows the result for the high EM-gain measurement. The linear range ends at ~8000 ADU, where the linearity plot starts to flatten out. Saturation is reached at ~14900 ADU, which corresponds to the true ADC limit of 14 bit after adding the previously removed bias value of 1400 ADU. The nonlinear behaviour between these two values seems to have multiple reasons. First, the linear range of the ADC at the chosen readout clock of 10 MHz is only ~13 bit according to the manufacturer. Second, similar measurements without electron multiplication gain show a slightly larger linear range, pointing to nonlinear effects in the electron multiplication register itself. The register cells should behave linear up to 400000 e^- according to the CCD datasheet. At this value the contribution of the electrons to the electric field in the multiplication

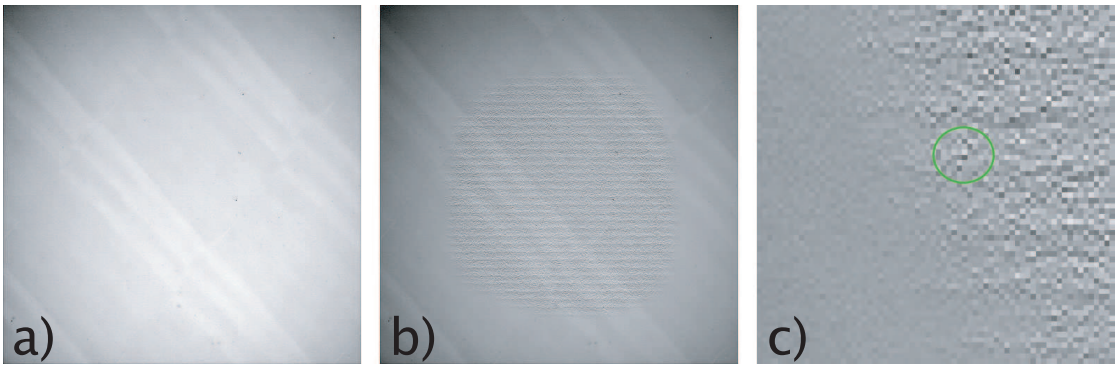

Figure 3.9. ***a)*** *Typical flatfield image in the linear range.* ***b)*** *Overexposed flatfield with strong nonlinearities in the central part.* ***c)*** *Close-up of the overexposed part. At least three vertical dark/bright pixel pairs can be identified in the encircled area.*

register starts to have significant effects on the multiplication gain. However, this value would correspond to more than 17000 ADU in the chosen setup, well above the end of the measured linear range. The value of 400000 e^- given in the detector datasheet refers to a specific readout timing and voltage scheme, and it is not known how closely the actual camera readout electronics follows these recommendations.

At the moment the reason for the nonlinear behaviour cannot be conclusively attributed to a particular part of the camera. It is recommended to stay within the measured linear ranges whenever possible, or to perform dedicated calibration measurements to establish a linearity correction allowing recovery of the full dynamic range. As a guideline, the linear ranges for different vertical clocks and shift voltages at full electron gain and a pixel readout frequency of 10 MHz are given in Table 3.3. For vertical shift times below 3.4 µs, the linear range is always limited by the vertical charge transfer efficiency if standard vertical clock voltages are applied.

The linearity measurements were performed on images of the 5×5 spot pattern with typically 2 pixels per FWHM. The pixel positions of the spots were measured over a wide range of illumination conditions and with different vertical clock pulse durations and clock voltages. No significant changes of the spot positions were observed for spot intensities within the linear range. This indicates that charge transfer inefficiency does not have a negative impact on astrometric measurements.

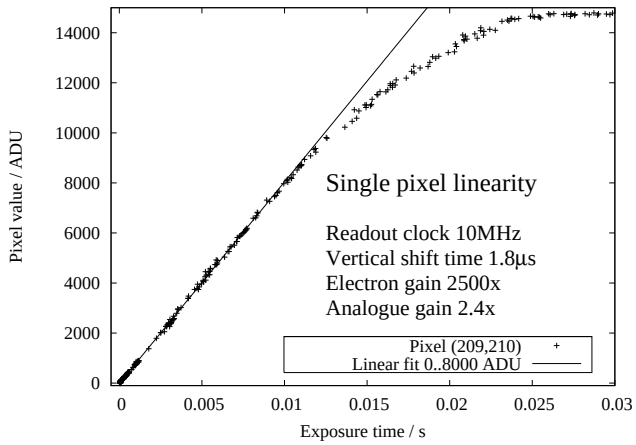

Figure 3.10. *Linearity plot for a single pixel position.*

Dark Current and Clock Induced Charges

As explained in Section 3.2.3, large electron gains allow the detection of single photons. Unfortunately the same is true for single dark current (DC) electrons and clock induced charges (CIC). In a first approach, the dark current was measured in the conventional way, i.e. by taking long dark exposures. The dark current at $T_{CCD}=-75°C$ was found to be 0.009 e^-/pixel/s, which would correspond to 80 events in a typical 33 ms frame transfer image. However, applying a simple thresholding algorithm detects a much higher number of pixels that deviate significantly from the background value, attributed to clock induced charges.
Even if no CICs were present, this dark signal estimate would probably be wrong, as a substantial fraction of dark current is actually generated during the readout phase, independently of the exposure time. This contribution is underestimated by simple scaling of the dark current measured in a long-exposure frame.

For the AstraLux camera, the combined probability of dark current and CIC events was measured for each possible combination of vertical shift time and clock voltage, at a fixed analogue gain of 2.4, a pixel clock of 10 MHz, and a temperature of −75°C. The histogram of the raw AD values in 100 bias frames was computed for each combination of parameters. Figure 3.11 shows the result for four different camera settings. All distributions deviate from a pure Gaussian, in contrast to the expectation for measurements with a conventional CCD. These differences increase with longer vertical shift times and higher shift voltages.

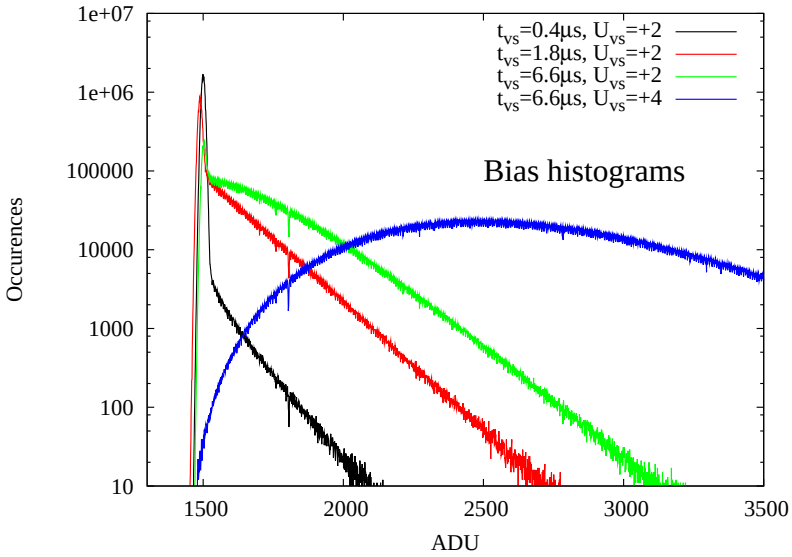

Figure 3.11. *Bias frame histograms at different vertical clock and voltage settings.*

The combination of a Gaussian peak and an exponential decay can be fitted to the histograms in the case of short shift times and low clock voltages. While the Gaussian part represents the readout noise, the exponentially decaying tail stems from single dark current electrons and CICs. If a single electron from the image area enters the electron multiplication register with a gain of g, then the probability for getting $n \geq 1$ electrons at the output is given by Tubbs (2003) as:

$$P(n) = \left[\exp\left(\frac{1}{g-\frac{1}{2}}\right) - 1\right] \cdot \exp\left(\frac{-n}{g-\frac{1}{2}}\right) \tag{3.5}$$

The slope of the exponentially decaying part is defined only by the electron multiplication gain, and this can be determined from the bias histogram in return, if the analogue conversion factor is known. A small software was written to iteratively fit the measured bias histograms with a model consisting of a delta function at the position of the bias value and the exponentially decaying tail computed from Equation 3.5. The fraction of DC and CIC events was varied by giving different weights to the delta function and the exponential part. This model was finally convolved with the readout noise, i.e. with a pure Gaussian. Electron gain, DC/CIC probability, and bias level were fitted iteratively until the global minimum of the residuals was found.
An example for such a fit is given in Figure 3.12. While the decay at high ADU values and the Gaussian peak are well fitted by the simple model (red line), strong residuals are left in the transition between these two regions.

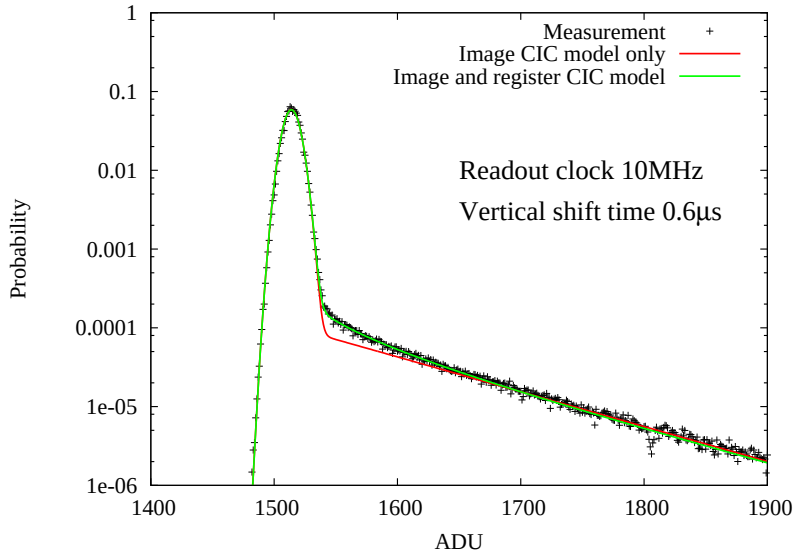

Figure 3.12. *Bias histogram fits considering only image pixel background events (red) and register CICs as well (green).*

These residuals are attributed to the fact that CICs may not only be generated in the image area during vertical shifts, but also during the readout process in the electron multiplication register itself. Since this can happen in any of the 536 stages of the register, using the total electron gain in Equation 3.5 leads to an incorrect result. If a CIC is produced in the i^{th} register cell, the effective gain will be only:

$$g_i = (1 + \mu)^{536-i} \tag{3.6}$$

Here μ is the probability for the impact ionisation process, which can be calculated from the known total electron gain as:

$$\mu = 1 - g^{\frac{1}{536}} \tag{3.7}$$

An improved model considers these register CICs under the assumption that the CIC probability is the same for each register cell. The model does not account for multiple DC or CIC electrons per image area pixel or the possibility of getting more than one additional electron in the impact ionisation process.

The two component fit in Figure 3.12 (green line) reproduces the measured histogram over the full range, confirming the validity of this approach. This is not entirely true if the model is applied to measurements with long shift times and higher shift voltages. The histograms for 6.6 µs shift time in Figure 3.11 cannot be fitted properly without considering multiple CIC events per pixel, and only lower limits for the CIC probability were derived for such camera settings. The results are summarised in Table 3.3. The given values are the combined probability for dark current and CIC events per pixel and frame. Values are given in parentheses in case the model delivered only a lower limit, and are completely omitted where no stable fit could be achieved. It is visible that background event rates as low as one percent can be reached with short vertical clock pulses – if a dynamic range of 1000 ADU is sufficient. This corresponds to only 9 photoelectrons at an electron gain of g=2500 and an analogue gain setting of 2.4. The choice of the optimal setting will always be the result of a trade-off between dynamic range, speed and background event probability.
If the dynamic range is an issue, then a vertical shift time of 1.8 µs at the standard voltage level will be a good choice: at a CIC probability of 11% the linear range is ≈7000 ADU, close to what is possible at 10 MHz pixel clock. Shorter vertical shift times may be used for high-speed photometry or in photon counting applications with known low photon fluxes.
The fitting algorithm also delivered independent measurements of the electron gain for each dataset, confirming the maximum value of g=2500 as plotted in Figure 3.7.

Table 3.3. *Linear ranges and combined background event (DC and CIC) probabilities for different vertical shift times t_{vs} and vertical shift voltage settings. All measurements are valid for T_{CCD}=−75°C, a pixel readout frequency of 10 MHz, and an analogue gain setting of 2.4. The linear range refers to a linearity better than 3%. The given values are accurate to 0.5% and 500 ADU, respectively.*

Vertical shift voltage setting:	0	+1	+2	+3	+4
t_{vs}=0.4µs	1.0% 1000 ADU	1.5% 2000 ADU	2.0% 3000 ADU	3.0% 3500 ADU	6.0% 4000 ADU
t_{vs}=0.6µs	1.5% 3000 ADU	2.5% 4000 ADU	4.5% 5500 ADU	8.5% 6500 ADU	14% 7000 ADU
t_{vs}=1.0µs	4% 5000 ADU	9% 6000 ADU	19% 7000 ADU	(35%) 8000 ADU	(50%) 9000 ADU
t_{vs}=1.8µs	11% 7000 ADU	23% 8000 ADU	(40%) 9000 ADU	9500 ADU	10 000 ADU
t_{vs}=3.4µs	16% 8000 ADU	(35%) 8500 ADU	9000 ADU	9500 ADU	10000 ADU
t_{vs}=6.6µs	21% 9500 ADU	(43%) 10000 ADU	10000 ADU	10000 ADU	10000 ADU

Oddities and Caveats

Potentially Missing Codes of the Analogue-Digital-Converter (ADC)

Figure 3.13 shows a small section of a bias histogram. Visual inspection reveals that every 8th AD value is significantly under-represented. This phenomenon can be observed in all bias frames and slightly depends on the readout frequency, with a more even distribution at 1 MHz. The drop of the distribution at 1807 ADU is present with any camera setting. Statistical analysis of the data exhibits that odd AD values are over-represented compared to even values. These observations point to decreased performance of the ADC at high readout clocks and explain the strong contribution of the ADC to the overall readout noise.

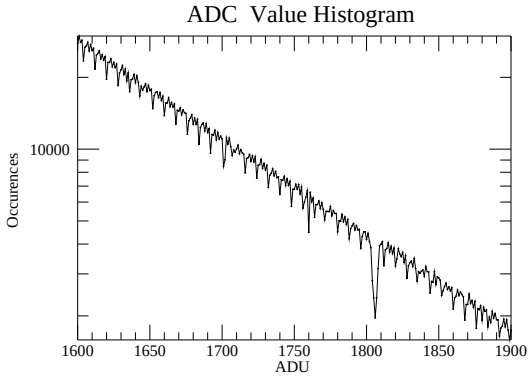

Figure 3.13. *Close-up of a bias frame histogram. Each 8th value is under-represented, caused by decreased ADC performance at high pixel clocks.*

Charge Trap in Column 244

Column 244 of the CCD suffers from a charge trap that can produce severe artefacts, depending on camera setting and illumination level. The trap retains just few electrons per clock cycle, but this will be visible at high electron gains. Figure 3.14 shows the appearance of the affected column in a uniformly illuminated image and with a rectangular light source on a dark background. Using higher vertical clock voltages and longer shift times will improve the transfer efficiency, but result in more CIC events.

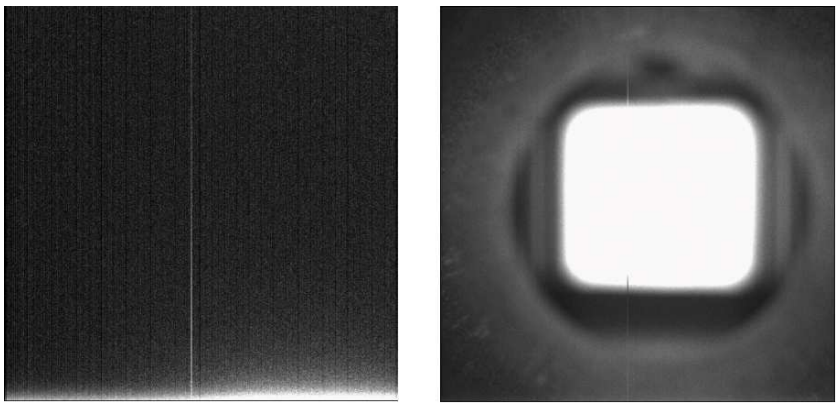

Figure 3.14. *Charge trapping in column 244. The left image is the average of 100 exposures at full electron gain and an illumination level of ~1 photon/pixel/frame. The rectangular area in the right image was illuminated with ~10 photons/pixel/frame.*

Bias Drift

Especially during EM operation, the bias level will drift due to small temperature changes induced by the readout register. Figure 3.15 shows a typical example for this behaviour. The exponential decrease at the beginning of the acquisition is common to most image series, but there is no possibility to predict the drift quantitatively. In longer exposure series it can be observed that the bias slowly increases towards the end of the acquisition. The only reliable way to achieve proper image calibration is to use blank areas of the image to scale a previously acquired bias frame. To suppress noise in the scaling process, an exponential model may be applied to the measured bias levels. For most observations a multi-component exponential model with additional linear trend can be used to fit the dependency of the bias level on the time t since acquisition start:

$$Bias = \alpha + \beta \exp\left(\frac{-t}{\tau_1}\right) + \gamma \exp\left(\frac{-t}{\tau_2}\right) + \delta t \tag{3.8}$$

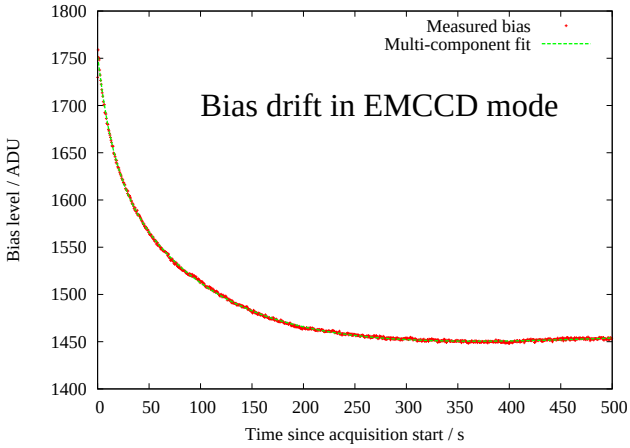

Figure 3.15. *Example measurement of drifting bias. A two-component exponential fit with a long-term linear trend is overlayed (see Equation 3.8). The measurement is based on a high-speed acquisition with 1.6 ms single frame exposure time and 8×8 pixel binning.*

Bias-Clamping Produces Inverted Images

The “Bias Clamping” feature is advertised by the camera manufacturer as an effective way to fix the bias level at a defined value. While this appears as a tempting way to overcome image calibration problems related to the drifting bias in electron multiplying operation, it should be strongly avoided in low-light-level situations. Laboratory experiments with a rectangular illuminated surface on dark background have shown that illumination levels of few photons per pixel and frame will cause the illuminated area to appear *darker* than the background, which is an extreme form of non-linearity.

Image Flip between Conventional and EM Operation

Switching between the conventional amplifier and the EM output does not change the image orientation on the control software’s live display, but the raw data in the FITS files will be horizontally flipped. This has caused some initial confusion, because flatfield images acquired through the conventional amplifier obviously resulted in unsatisfactory correction of EM-data. It has been confirmed though, that the image flip is exact and no additional pixel shift is introduced. The physical explanation simply is that the readout occurs as indicated in Figure 3.1: the horizontal shift direction is reversed in EM operation and the electrons make a U-turn in the corner elements.

Image Smear

This is a common feature of all frame-transfer CCDs. When pixels are vertically clocked into the store area, they will pick up signal of light sources in the same column. The impact on the final image depends on the ratio between exposure time and vertical shift duration. Figure 3.16 shows typical examples for frame-transfer image smear.

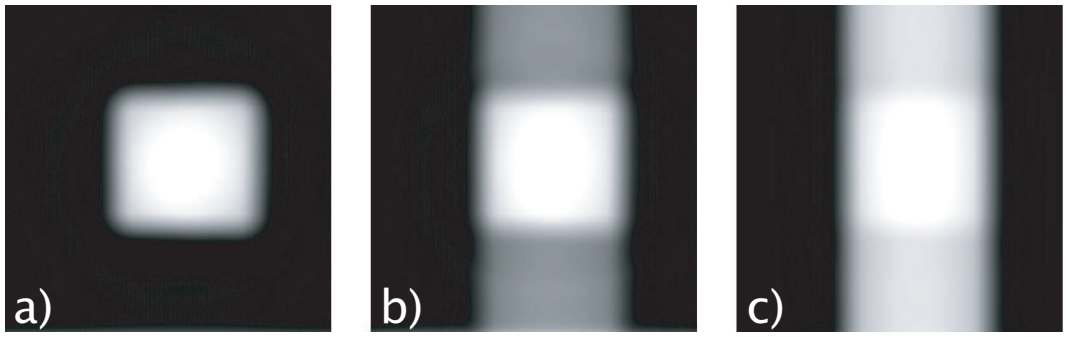

Figure 3.16. *Image smear examples.* ***a)*** *Vertical shift time 0.6* μ*s, single image with 10 ms exposure time.* ***b)*** *Same settings, but average of 100 images with 100* μ*s single frame exposure time.* ***c)*** *Same as middle image, but now with a vertical shift time of 3.4* μ*s.*

EM-Gain Drift and Ageing

It is known that the EM-gain is subject to changes depending on the illumination history. High signal levels close to the saturation level will cause gain variations on timescales of seconds to minutes, and saturation over longer periods can permanently reduce the maximum achievable electron multiplication gain. While EMCCDs are not as sensitive to saturation conditions as image intensifiers, improper handling will affect their performance. The EM amplifier should always be switched off if it is not really needed to avoid performance degradation. Even under perfect conditions and careful operation, a gradual decrease of the EM gain with time has to be expected, though.

3.4 Fore-Optics and Filter Wheel

At the MPIA 70 cm or Calar Alto 2.2 m telescope, the camera's physical pixel size of 16 μm roughly corresponds to almost twice the size of the theoretical PSF at 910 nm (SDSS z' band). Diffraction limited imaging is thus not possible without some kind of magnification optics that increases the effective focal length. Table 3.4 gives the basic optical parameters of the Calar Alto 2.2 m telescope and lists the PSF sizes and pixel scales for different magnification factors.

Proper sampling in the sense of the Nyquist criterion can only be reached with a magnification factor of 5 in SDSS z', and even larger factors are necessary for observations at shorter wavelengths. For the final design, a value of 4 was adopted as a good compromise between spatial sampling and the size of the field of view.

With lenses, there are in principle two ways to realise such a magnification. The first possibility is to use a combination of two positive achromats to re-image the focal plane of the telescope onto the detector. The ratio of the focal lengths of these achromats will then define the actual

Table 3.4. *Angular and linear PSF sizes, PSF sampling, pixel scale, and size of the field of view for different magnification factors at the Calar Alto 2.2 m telescope. The PSF sizes refer to the full width at half maximum.*

	PSF size [μm]		Pixel/PSF		Pixel scale	FoV
Magnification	λ=650 nm	λ=910 nm	λ=650 nm	λ=910 nm	[″/px]	[″]
1	5.3	7.4	0.33	0.46	0.188	96
2	10.7	14.9	0.66	0.93	0.094	46
3	15.9	22.3	0.99	1.39	0.063	32
4	21.2	29.7	1.33	1.89	0.047	24
5	26.5	37.1	1.66	2.32	0.038	19

Optical properties of the Calar Alto 2.2 m Cassegrain telescope:

Primary mirror diameter:	2.2 m
Central obstruction:	0.89 m
Focal length and ratio:	17.6 m, f/8
FWHM of diffraction limited PSF:	0.″062 at λ=650 nm, 0.″087 at λ=910 nm

magnification. This configuration has on one hand the advantage that both the focal and the pupil plane are accessible for aperture masking and coronagraphic experiments. On the other hand, such a re-imaging optics will not be very compact and usually add several 10 cm to the total instrument length. This problem could be overcome by introducing folding mirrors, but only at the cost of more surfaces in the optical path.

The alternative chosen for the AstraLux instrument is a single negative achromat in Barlow configuration, i.e. placed in the optical path before the nominal focal plane of the telescope. This lens widens up the beam, effectively increasing the focal length. If the distance between the lens and the nominal focus position is kept very small, and if the lens has a short focal length, such a magnification optics can be built very compact. It should be mentioned though, that this design does not allow access to the focal or pupil plane anymore – if this is demanded, only a two-lens re-imaging optics can be used.

The AstraLux Barlow lens is a Thorlabs ACN127-030-B achromat with a diameter of d=12.7 mm and a focal length of only f=−30 mm. It is optimised and coated for the wavelength range 650−1050 nm. Figure 3.17 shows the actual position of the lens in the 2.2 m telescope beam behind the filter wheel. Spot diagrams for three wavelengths and four positions on the detector are reproduced in Figure 3.18 as well as field curvature and distortion curves. If placed at the calculated optimal position in the telescope beam, the lens provides diffraction limited image quality over the full field of view and the whole specified wavelength range. Field distortion of up to 0.5% is the result of using a lens with such a short focal length in a non-telecentric configuration. Though this poses an instrumental limit to the astrometric accuracy if it is not properly calibrated, it allows a very compact construction of the fore-optics.

The lens is held in a standard C-mount tube – bought “off-the-shelf” like the lens itself – that is mounted directly on the camera. This guarantees a high stability of the pixel scale, which strongly depends on the distance between lens and CCD. Tolerances for tilt and de-centre of the lens were found to be 2° and 1 mm, respectively, referring to a geometric spot pattern size smaller than the diffraction limited PSF. The direct connection between camera and lens tube helps to achieve a good alignment, and eases dis- and reassembly of the camera system. The lens

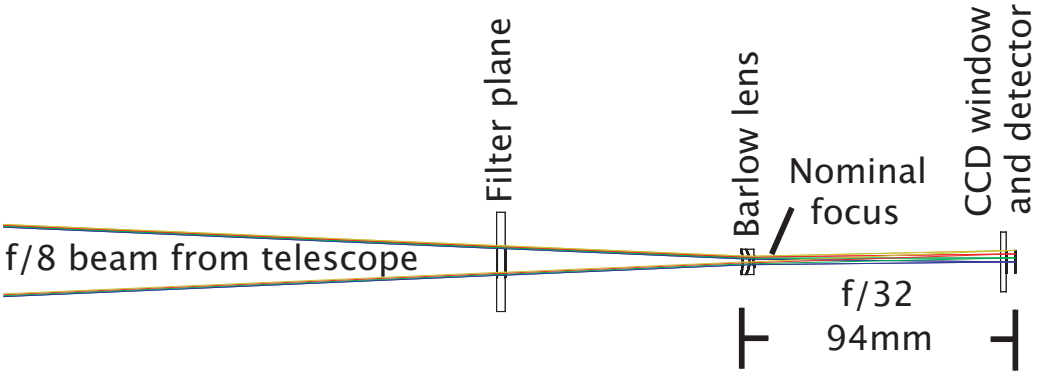

Figure 3.17. *Layout of the magnification optics. The given dimensions refer to the setup at the Calar Alto 2.2 m telescope.*

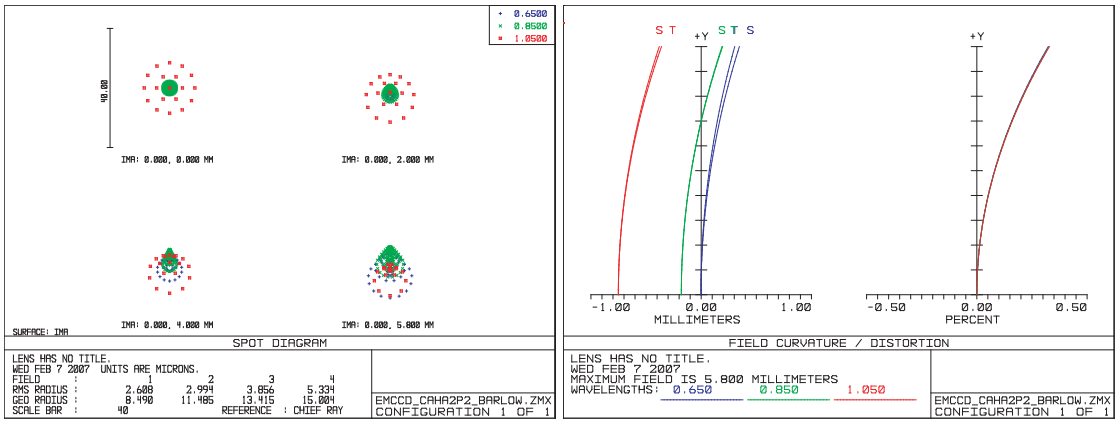

Figure 3.18. *Spot diagram of the Barlow lens and field distortion curves.*

tube also holds four pinholes that were added to prevent straylight from the lens edges and the tube walls from reaching the detector.

For operations at the Calar Alto 2.2 m telescope it was decided to refurbish the so-called *Instrumenansatz 1* (IA1), an adapter that was used for mounting conventional CCDs in the past (see Figure 3.19). This device can be mounted behind the video guider unit at the Cassegrain focus of the telescope and includes a filter wheel with 8 positions. This wheel can hold virtually any filter that is available at the observatory, allowing observations at a wide range of wavelengths. The filter wheel comes with a control electronics providing an RS 232 communications interface to receive commands and to output status information. A small graphical user interface was written by the author to remote control the wheel position, log any filter changes to a file, and to monitor fault conditions of the wheel, e.g. timeouts and communication errors.

3.5 Camera Mount

The camera mount can be attached to the Königstuhl 70 cm telescope as well as to the IA-1 at the Calar Alto 2.2 m telescope with the same flange. The camera is fixed between two L-brackets using four of the six mounting holes of the camera housing. These mounting holes lie below the

Figure 3.19. *The* Instrumentenansatz 1. *The filter wheel* FI-8 *is mounted in the lower part of the* IA 1 *and can be rotated either remote or manually via the black knob on its top.*

surface of the plastic camera housing, thus a set of steel adapters was manufactured to provide a direct metal-to-metal connection between L-brackets and camera structure.

A solid aluminium tube between camera and flange defines the camera's position in the optical path and guarantees proper alignment. This tube is bolted to both the flange and the frontside of the camera[3]. Tubes with different lengths were manufactured to allow optimal positioning of the camera at both telescopes.
The mount is very rigid and probably suitable for cameras with a much higher weight than the 3.1 kg of the Andor camera. Figure 3.20 shows the complete assembly of camera, Barlow lens and mount.

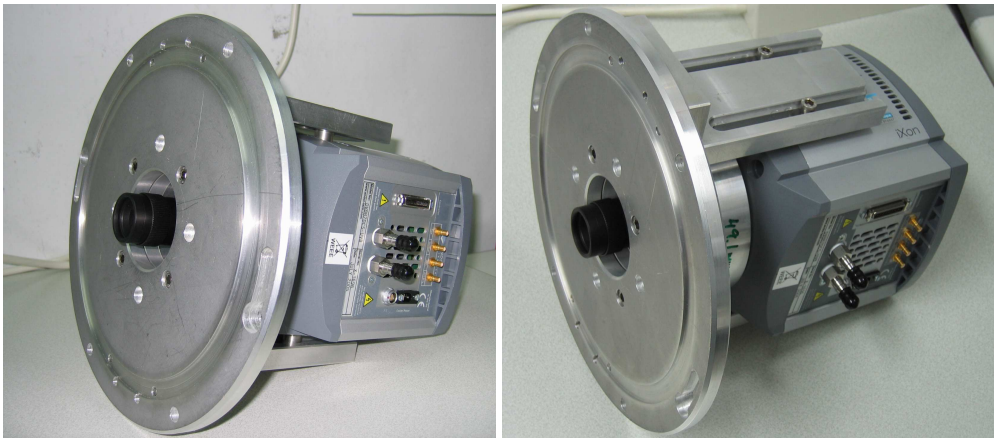

Figure 3.20. *The camera in its mount. The Barlow lens is held in the front of the black C-mount tube attached to the camera.*

[3]Fortunately, there are four threaded holes on the front of the camera for this purpose, though they do not appear in any camera datasheet.

3.6 Computer and Software

In principle, AstraLux can be operated with a single computer that controls both the camera and the filter wheel. In practice, the maximum allowed camera cable length of 6 m requires to mount this computer directly at the mirror cell of the Calar Alto 2.2 m telescope. The system that actually runs the camera and filter wheel software is therefore remote controlled by a standard PC located in the telescope control room. This second computer does not only display the desktop contents of the camera computer, it also serves as the primary storage for the raw data. Depending on the camera settings, the data rate reaches up to 18 MB/s, too high for a normal copper-cable 100 MBit/s link. The connection is actually established via a dedicated 1 GBit/s fibre cable, allowing simultaneous data storage and remote control without noticeable delays or slow-down of data acquisition.

Data storage requires additional hardware. It is possible to produce up to 400 GB of raw data in a single night with AstraLux, but the remote control computer can hold only up to 1 TB, not enough for more than two or three nights. Furthermore, there is the problem of getting the data from the observatory to the home institute of the observer – the 8 MBit/s Internet link of Calar Alto does not provide the necessary bandwidth for this.
The data storage problem was addressed by adding a 2 TB network storage server to the system. This device is used to back up data from the previous night during the day, so that the primary storage disks can be freed in the afternoon. The transport problem was solved by using external harddisks with 400 GB capacity each. These can be connected to the computer network via an USB 2.0 interface, and easily transported in the observer's luggage or sent by air-mail. The backup possibility on the network storage server ensures that no data is irrecoverably lost if one of the external disks gets damaged during transport – which actually happened after the first observing run.

In November 2006, a third computer was added to the AstraLux network. This system is a high-performance multi-processor machine running the online version of the AstraLux pipeline (see Chapter 4). It is now equipped with 2.2 TB of harddisk space, serving as additional backup facility and data reduction terminal during daytime.

An overview of the complete AstraLux computer and data storage system as it was in February 2007 is shown in Figure 3.21. At the moment, all components except the camera computer are located in the telescope control room of the dome building. For future operations it is planned to relocate at least the remote control computer to the library building downhill, from where most other 2.2 m telescope instruments are operated nowadays.

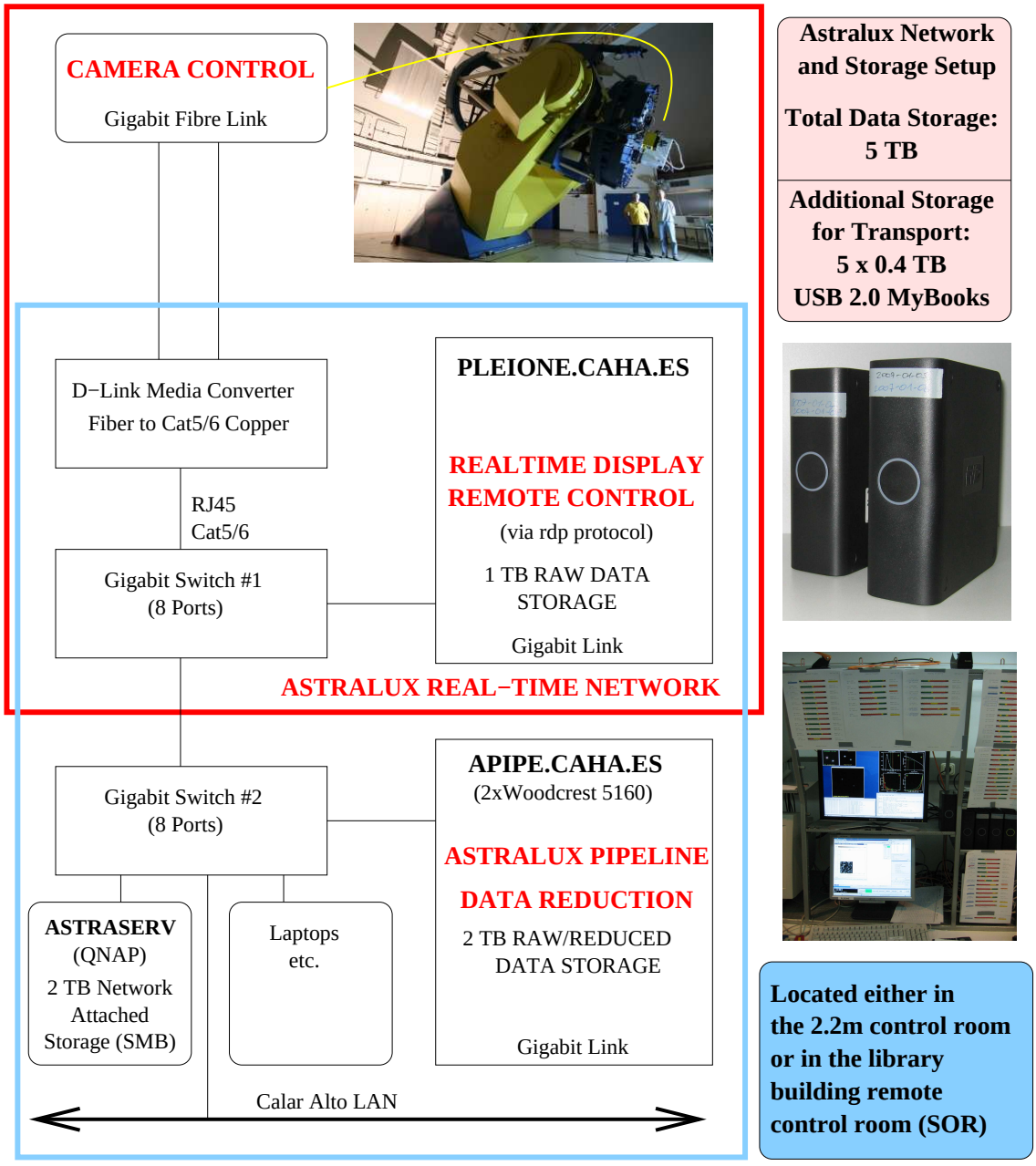

Figure 3.21. *Overview of the AstraLux computer and storage network.*

Chapter 4

The AstraLux Pipeline

4.1 Introduction

Since the early Lucky Imaging experiments at the MPIA 70 cm telescope, the data reduction tools have matured from a set of simple scripts to an integrated data reduction environment. This software suite is written in IDL[1], and provides all necessary tools and commands to process an AstraLux observation from raw FITS data cubes to a final Lucky Imaging result. The AstraLux software can be configured to run in pipeline mode, providing near real-time reduction capability directly at the telescope. For the observer, this offers the flexibility to dynamically decide if e.g. a newly discovered binary should be re-observed in a different filter or if an observation has to repeated under better seeing conditions.

This chapter describes the layout of the pipeline and the basic reduction steps. While the general construct of the AstraLux data reduction environment will probably not undergo major redesigns, certain data analysis and image reconstruction steps will most likely be improved in the future, and additional capabilities may be added. The software development depends on the input provided by AstraLux users, and is certainly not finished for the time being.

As of March 2007, the AstraLux data reduction software is running on a dedicated pipeline computer, equipped with two dual-core Woodcrest processors and 8 GB of memory. This system produces quicklook results of Lucky Imaging observations in approximately the same time that is needed for data acquisition. The final AstraLux pipeline will be available in two versions. The so-called "online version" will be optimised for the fast automatic generation of preview results at the telescope, while the "offline version" will provide better data reduction results at decreased processing speed. Both versions have their own right: while the online version is essential for effective observing and on-site assessment of the data quality, only the offline version can provide final data products with highest quality.

[1] Integrated Data Language, `http://www.ittvis.com/idl/`

4.2 Communication with Telescope, Camera, and Filter Wheel

The current setup at the Calar Alto 2.2 m telescope does not provide a unified method to gather status information from the telescope control system, the camera software, or the filter wheel. Nevertheless, all vital parameters are queried and stored each time a new acquisition is started.
The pipeline's *Data Fetching Module* continuously monitors the raw data directory for the appearance of any new FITS file. When this happens, the telescope's position, focus value, and environmental parameters are retrieved from the telescope control system in the form of a FITS header. This header is completed with the current filter wheel position, read from a text file that is updated by the filter wheel software on each filter change. The FITS header is stored as one of the pipeline products, together with the name of the data cube that triggered its creation.
The processing stage of the pipeline cannot be started before the data acquisition is complete. In the case of large raw data sets, the camera software will not create a single FITS cube, but break the observation up into numbered files with 2 GB size each. In principle, the end of data acquisition could be recognised by monitoring the data directory. If the observation is complete, no FITS files with the same prefix will be created, and the existing ones will not change in size. However, this method frequently failed and started the pipeline too early in the past, probably because of delays in the update of the file system information. Fortunately, the camera software can be configured to execute an external program or batch file when the acquisition is complete. In the current setup, this mechanism is used to signal the data fetching module that the pipeline process can be initiated.
Before this actually happens, all files belonging to the finished observation will be copied to a local directory on the pipeline computer. This does not interfere with camera operation and is an effective way to create a backup of the raw data already during the night.

4.3 Pipeline Steps

Before an observation can be processed, it has to be decided which of the processing options is the correct one for the given data. Currently, this decision is entirely based on the filenames of the FITS cubes. The *Branching Module* will simply check if a filename ends on e.g. `_Bias.fits` or `_Flat.fits`, and then start the routines for the master calibration file generation. It is also possible to define filename endings that will cause a dataset to be ignored by the pipeline. This is a useful feature to prevent a high-speed photometry observation from being processed as Lucky Imaging data. In this case, data reduction is skipped and only an entry in the pipeline logfile created. All other files are assumed to be Lucky Imaging observations and consequently fed into the *Science Module*. Figure 4.4 visualises this first part of the pipeline data flow.

4.3.1 Calibration Data

Both bias and flatfield cubes are combined to master calibration images using a kappa-sigma clipping algorithm. In the case of flatfield images acquired through the conventional amplifier, this will prevent cosmics from appearing in the final product. Since bias frames are usually acquired with the same camera parameters as the corresponding science observation, i.e. at high electron gains, they will most likely be contaminated by clock induced charges (CICs). With typically 50−100 single frames in a bias cube, these background events are removed by kappa-sigma clipping as well.

All master calibration files are stored in a separate directory, and are part of the final set of pipeline products. Master flatfields are displayed in the pipeline result window to allow visual assessment of the dust contamination on the CCD entrance window and Barlow lens.

4.3.2 Science Data

The layout of the Lucky Imaging reduction module is illustrated in Figure 4.5. First, the position of a suitable reference object for quality assessment has to be determined. This is performed on a stacked image of the first 2 seconds of raw data, and can be done either manually or automatically. While the manual option allows to select any star just by clicking on the image, the automatic reference finding algorithm will always choose the brightest object in the field of view.

The *Quality Assessment Module* determines the Strehl ratio of the reference object in each single image. The *Image Selection* module will then pass the indices of frames with sufficient quality to the *Image Reconstruction* module, which produces the final image products.

Quality Assessment

The *Quality Assessment Module* extracts a small region around the reference object in each frame and performs bias subtraction and flatfielding on this sub-image. This typically 32×32 pixel sized image portions are resampled and noise-filtered before the Strehl ratio of the reference source is measured. The resampling introduces a magnification of typically 4, and serves two purposes. First, since the position of the brightest pixel of the reference object's PSF will be used as input to the image reconstruction algorithm, sub-pixel shifting can only work if the reference position is determined on resampled images. Second, the resampled images allow better estimates of the Strehl ratio. The Strehl value is derived from measurements of the ratio between peak flux and total flux of the reference object – a simple and fast method. Unfortunately, the peak flux in the slightly undersampled AstraLux images depends on the precise position of the PSF peak within the brightest pixel, while the total flux is independent of the reference object's position. Simulations with the AstraLux pixel scale of $\approx$47 mas showed that Strehl measurements of a perfect PSF would suffer from a jitter of up to 20% (see Figure 4.2). Tubbs (2003) found that this jitter can be reduced to 1% and less by resampling the data before measuring the Strehl ratio. If the data is not only resampled, but also filtered with the telescope's modulation transfer function (MTF), the resampling will not introduce additional noise and single-pixel events like CICs and dark current electrons can be suppressed.

Figure 4.1 illustrates the actual implementation in the AstraLux pipeline. A 32×32 pixel sub-image around the reference star is extracted and fast Fourier transformed (FFT). After multiplication with the telescope's MTF, the FFT array is inserted in a 128×128 pixel image in the Fourier domain. Inverse FFT then results in a noise-filtered and four-fold magnified image of the reference star. The telescope MTF is calculated from a polychromatic theoretical PSF, taking filter transmission curve, camera quantum efficiency, and pupil obscuration due to the secondary mirror into account. Theoretical PSFs can be generated for any filter available at the telescope, and are part of the pipeline products. These PSFs also serve as the reference for the calculation of absolute Strehl ratios during quality assessment.

The *Quality Assessment Module* outputs the Strehl ratio and position of the reference object in each single frame. The *Image Selection* module decides which images are worth to be combined to the final Lucky Imaging result.

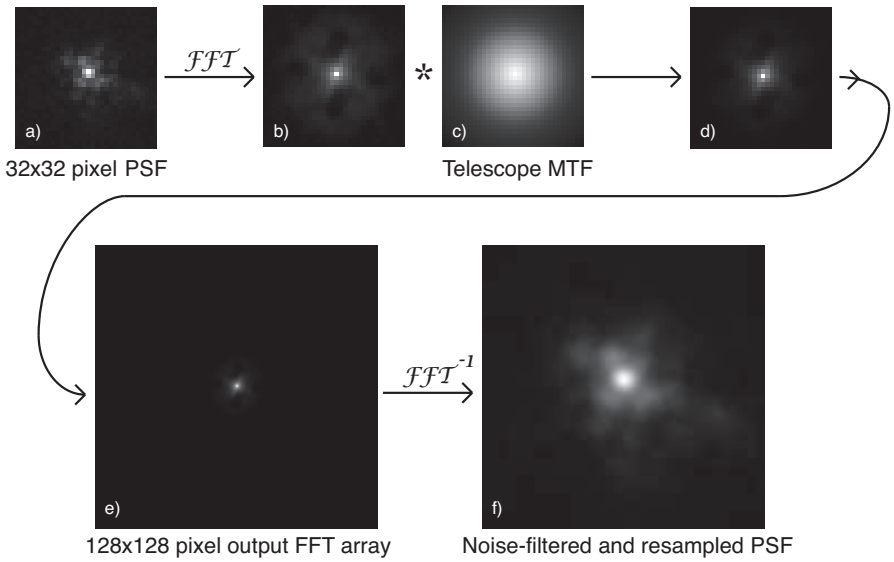

Figure 4.1. *FFT filtering and resizing. The reference source image (a) is fast Fourier transformed (b) and multiplied by the telescope's MTF (c). The spatial frequencies of the filtered image (d) are inserted in a larger array (e), and the resampled real image of the reference star is obtained by an inverse FFT (f).*

Image Reconstruction

The *Image Reconstruction* module performs data reduction in its literal sense. From typically several GB of input data, just a few MB of pipeline results are produced. The most interesting ones – the Lucky Imaging results – are currently generated with the Drizzle algorithm (Fruchter and Hook, 2002). This linear reconstruction method is flux preserving and able to at least partially overcome the slight undersampling that is present in the raw data. It is capable of handling subpixel translations without the need to perform image shifting in the Fourier domain. The current IDL implementation of the Drizzle algorithm is somewhat simplified and does not consider image rotation or field distortions, but just shifts the selected images such that the brightest pixel of the reference star is always positioned at the same pixel coordinates. The drizzling process oversamples the input data twice, resulting in a pixel scale of ≈23.7 mas/px in the final images.

The pipeline does not only provide high-resolution data that is based on the best few percent of all images, but also generates a set of "full-photon" images from 100% of the raw data. A seeing limited image with a simulated autoguider time constant of typically 5 s is produced to allow quick measurements of the seeing conditions, useful at times when the observatory's seeing monitor is switched off, or for later assessment of the data quality. A tip-tilt corrected and a peak-tracking result are generated as well, based on the centre of weight of the reference star's signal and its peak position, respectively. Both images are reconstructed by integer pixel shifting, and the original pixel scale is preserved. Figure 4.3 is a screenshot of the AstraLux pipeline during operation, showing all of the pipeline image products.

Not only the reconstruction method can be fine-tuned, but other parameters like the choice of the reference source or the percentage of images used for the final result, can also be adjusted to get the best possible results. Thus it is essential for the observer to have full access to the raw data. Only then he will be able to fully exploit the capabilities of the instrument and the data reduction

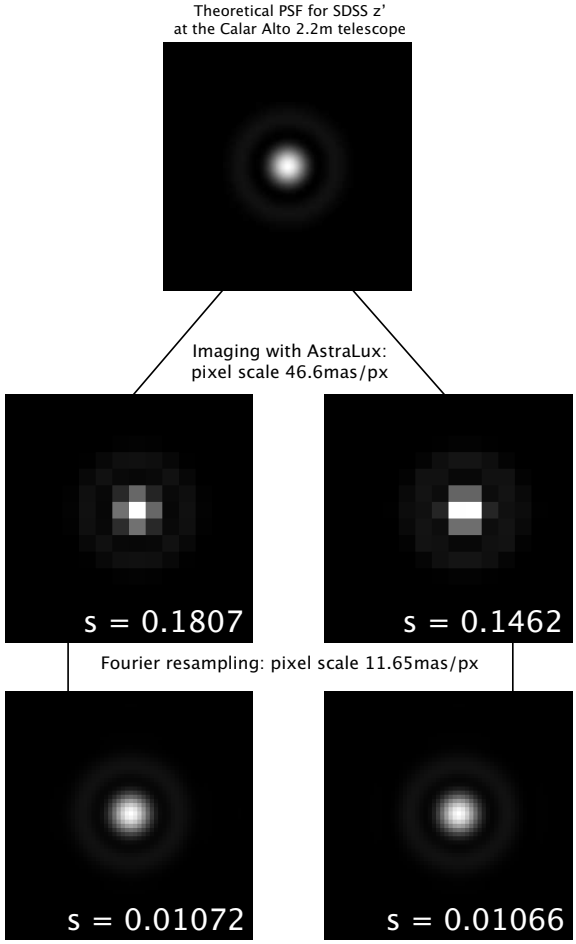

Figure 4.2. *Application of FFT resampling to undersampled images of a perfect PSF. The theoretical PSF for the SDSS z' band (top) is imaged with the AstraLux pixel scale of 46.6 mas/px (middle) and then Fourier resampled with a resulting pixel scale of 11.65 mas/px (bottom). For the images on the left side, the peak of the theoretical PSF was positioned in the centre of the middle pixel, and horizontally shifted by half a pixel for the images on the right side. The "Pseudo-Strehl" ratios* s*, defined as the ratio of peak intensity over total PSF flux, deviate by more than 20% for the undersampled images, and by less than 1% after Fourier resampling.*

software. Though this means that data transport and storage of up to several 100 GB have to be organised, careful post-reduction can never be substituted by blind trust in the pipeline quicklook results.

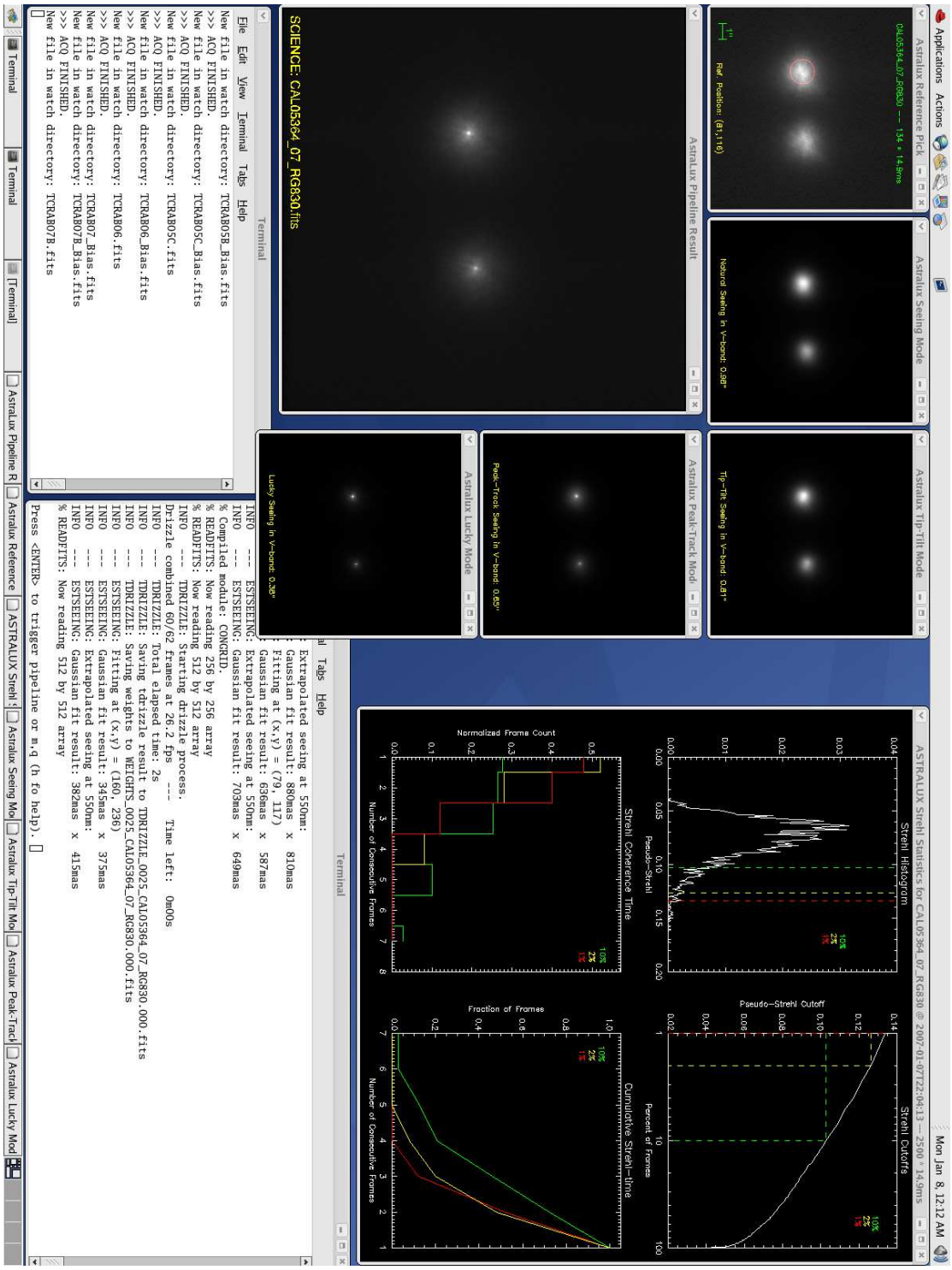

Figure 4.3. *AstraLux pipeline screenshot. The large window to the left contains the logarithmically scaled Lucky Imaging result of a calibration binary observation. The small windows above show the reference source selection frame, the seeing limited image, and the tip/tilt corrected result. The two small windows to the right of the Lucky Imaging result contain the peak-tracking image and a linearly scaled version of the final pipeline output. The Strehl statistics on the right side of the screen, especially the Strehl histogram in the upper left corner of the statistics window, are useful to get a picture of the seeing conditions and the data quality to be expected.*

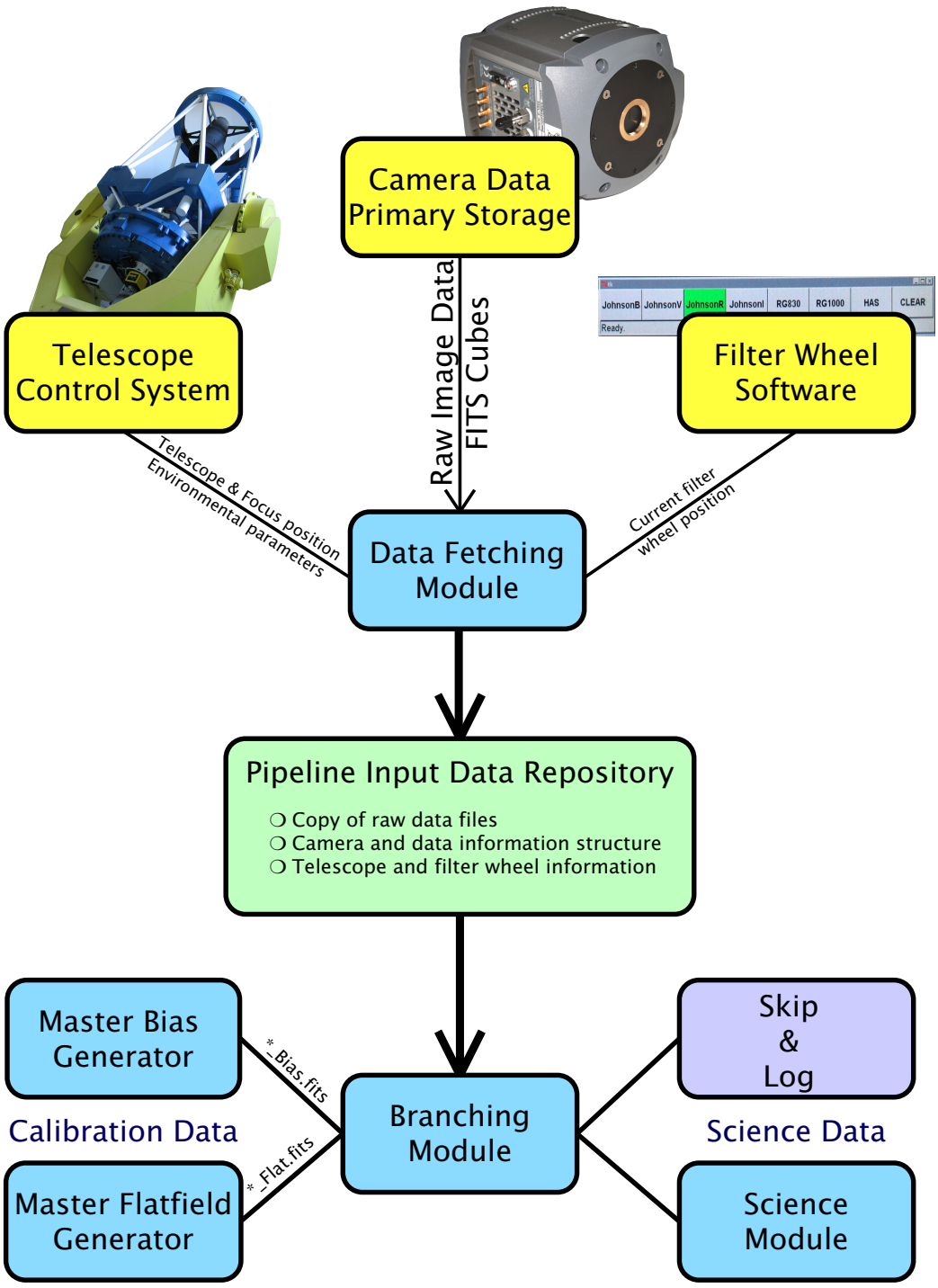

Figure 4.4. *Data flow of the AstraLux pipeline. The* Data Fetching Module *gathers raw camera data, telescope information, and filter wheel status, and deposits all necessary data for the pipeline process in the* Pipeline Input Data Repository. *The* Branching Module *decides which reduction module will actually be invoked for a specific observation.*

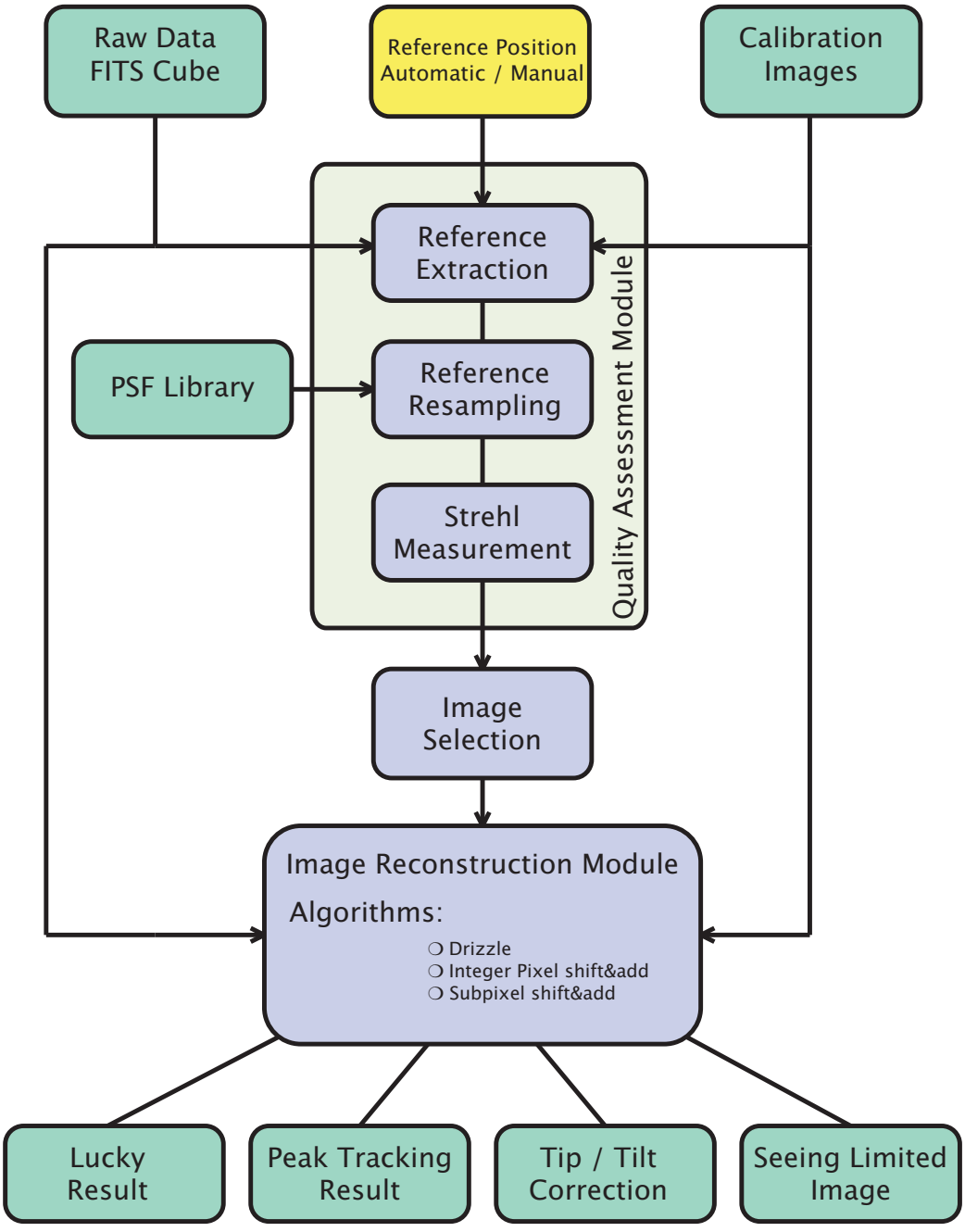

Figure 4.5. *AstraLux pipeline data flow in the* Science Module. *See text for detailed description.*

Chapter 5

AstraLux First Light and Performance

First light at the Calar Alto 2.2 m telescope was obtained on July 6, 2006. From a total of 5 nights during the first observing run, only half a night was lost due to bad weather, and the remaining time provided photometric sky conditions with *V*-band seeing values as low as 0.″6 – well below the Calar Alto median seeing of 0.″9.
The instrument was assembled during the night before the observing run to allow mounting of the camera in the morning. Crucial issues, e.g. electrical connections or cable lengths, were tested in Heidelberg in advance. Figure 5.1 shows the telescope and the instrument as it was in July 2006. The remote control computer was set up in the telescope building's control room, and the data connection to the camera computer was established with a 50 m dual fibre cable. Hardware testing and the acquisition of dome flatfields were completed in the afternoon. All in all, instrument preparation was completed in just a few hours, and all components worked flawlessly.
The following sections give examples of the early Lucky Imaging results and demonstrate the instrument's capabilities. A large part of this chapter handles the quantitative assessment of AstraLux's performance, e.g. detection limits for close companions to brighter stars, the typical isoplanatic angle, or limiting magnitudes for the reference star selection. All Lucky Imaging examples were processed with the AstraLux pipeline (see Chapter 4). At a physical pixel scale of 46.6 mas/px, the Drizzle process resulted in a final pixel scale of 23.3 mas/px.

5.1 First Light

First light observations were obtained on known bright double stars under a 0.″7 *V*-band seeing. Two results with a Strehl ratio of ≈20% and visible first diffraction rings are shown in Figure 5.2. Operating the instrument, and especially acquiring the targets, proved to be much easier than anticipated. Though the pointing accuracy of the telescope was in general not better than ≈10″, the availability of the camera's real time display reduced acquisition overheads to typically 1-2 minutes per object. Tests with AstraLux at the MPIA 70 cm telescope in May 2006 had shown that focusing can be accomplished most effectively by visual assessment of the speckle images on the real time display. There was no measurable advantage in taking focus series with long integration times. The "by-eye" focusing was used throughout the Calar Alto observations, contributing only few minutes per night to the total overheads.

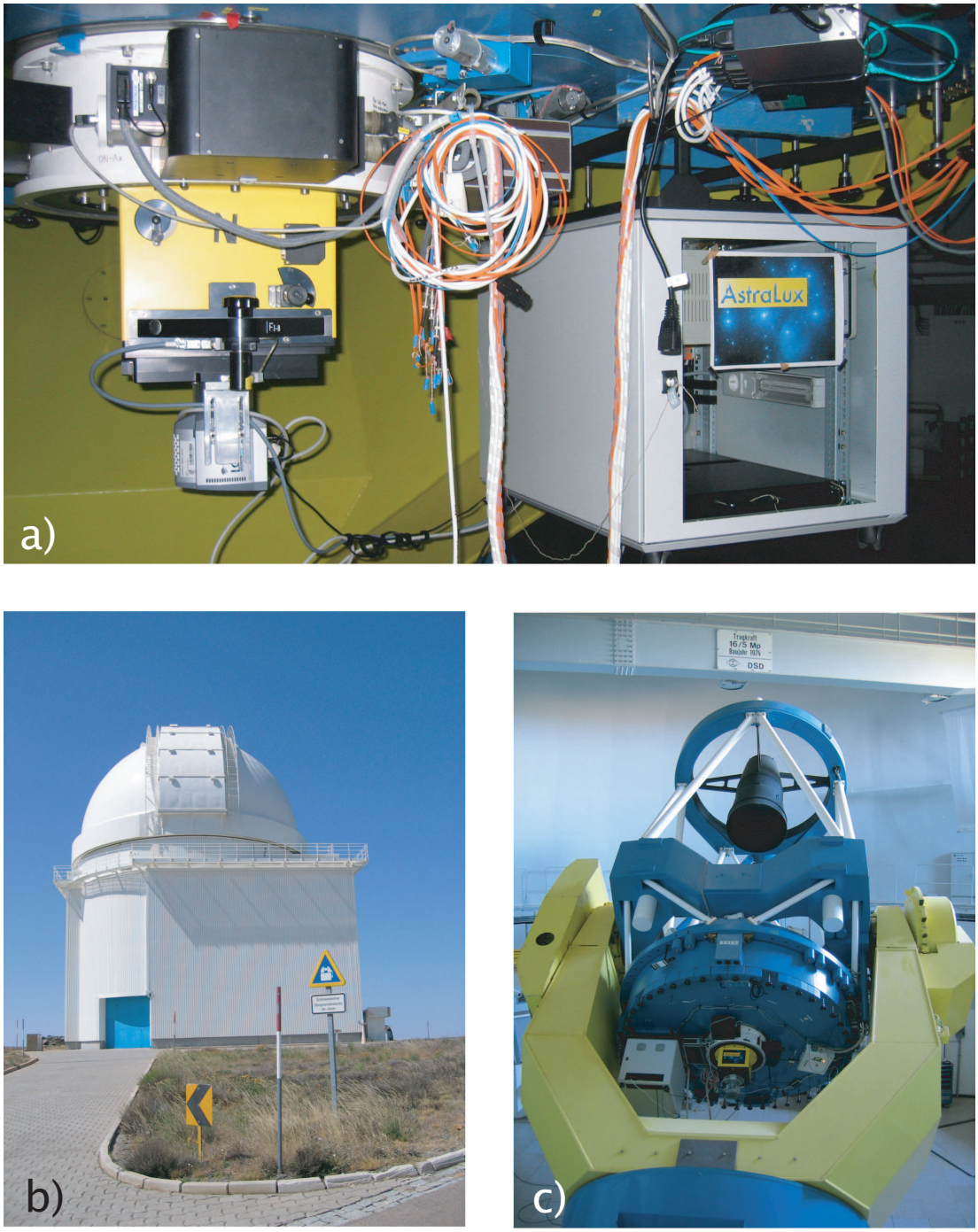

Figure 5.1. *AstraLux and the Calar Alto 2.2 m telescope.* ***a)*** *The instrument at the Cassegrain focus. The AstraLux camera is attached to the – now painted yellow –* Instrumentenansatz IA 1 *below the TV guider. The electronics rack to the right houses the camera control computer, a monitor/keyboard combination and the filter wheel control electronics.* ***b)*** *The 2.2 m telescope building on a perfect Andalusian summer's day.* ***c)*** *The 2.2 m telescope, pointing to the pole.*

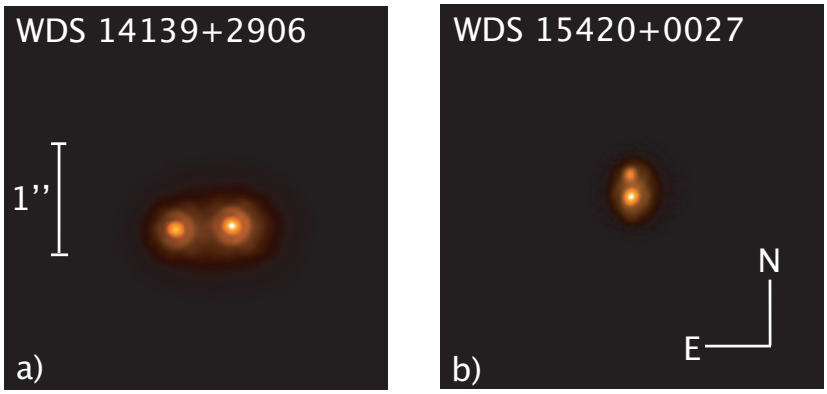

Figure 5.2. *AstraLux First Light double stars:* ***a)*** *The binary WDS 14139+2906 with an angular separation of 0.″52 and component magnitudes V=7.5 and V=7.6 mag.* ***b)*** *The 0.″23 separated binary WDS 15420+0027 with V=8.2 and V=8.8 mag component brightnesses. Both images are based on a 2%-selection from 10000 single frames in the SDSS z′ filter with 30 ms exposure time each. Image scaling is linear.*

5.2 Observations of Single and Double Stars

5.2.1 Radial PSF Profile

In the absence of atmospheric dispersion effects (see Section 5.2.5 for examples) the point spread functions (PSF) of Lucky Imaging results show a remarkable radial symmetry. There are no long-lived speckles due to static aberrations like they are frequently observed in adaptive optics images. Using a sufficiently large number of input images – typically several thousands – averages out any asymmetries. For the quantitative assessment of the PSF shape, it is therefore sufficient to consider the radially averaged profile only.

Figure 5.3 shows the radial PSF profile of ψ *Ser*, observed under a *V*-band seeing of 0.″75 with 15 ms single frame exposure time through the SDSS z' filter. The profile is plotted for a range of selection rates from the 10000 input images. The theoretical and seeing limited PSF profiles are overlayed for comparison. The seeing limited image, the Lucky Imaging result, and two single frame exposures are displayed in Figure 5.4.
The profile of the theoretical PSF was derived from a simulated diffraction limited image with 2.237 mas/px pixel scale, whereas the raw observational data was sampled with ≈46.6 mas/px. Though the Drizzle process of the pipeline results in a final pixel scale of 23.3 mas/px, principally providing proper sampling in the sense of Nyquist, this is not sufficient to reconstruct a perfect PSF even in the absence of any aberrations due to atmospheric turbulence or telescope imperfections. However, for the judgement of image quality and the measurement of Strehl ratios, only the perfectly sampled PSF will be considered throughout this chapter.

To calculate the Strehl ratios, all radial profiles were interpolated on a common two-dimensional radius grid and numerically integrated to derive the total flux. The Pseudo-Strehl, i.e. the ratio of peak flux over total flux, was calculated for each profile, and divided by the Pseudo-Strehl of the theoretical PSF to obtain the real Strehl ratio. Since the radial profile of a source can be reliably

Table 5.1. *Strehl ratios and PSF diameters for SDSS z'-band observations of the single star* ψ Ser. *The selection rates refer to a total of 10000 frames with 15 ms single frame exposure time. The observations were performed under a V-band seeing of 0.″75. Values for the seeing limited image and a diffraction limited PSF are given for comparison.*

Selection rate	FWHM [mas]	Strehl [%]
(Theoretical)	78	100
1%	114	14.2
2.5%	118	12.5
5%	120	11.5
10%	122	10.4
25%	128	8.9
50%	132	7.7
100%	138	6.2
(Seeing limited)	690	1.9

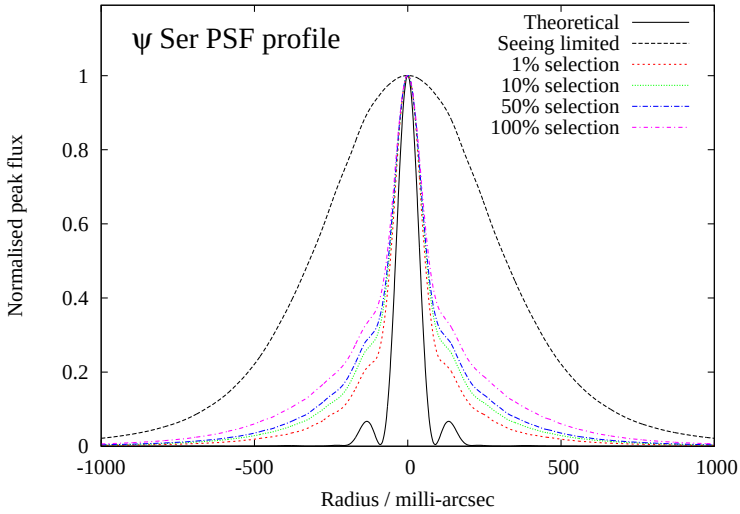

Figure 5.3. *Radial profiles of the stellar PSF for different image selection rates. The seeing limited and diffraction limited PSF are plotted for comparison. All profiles have been normalised to a peak flux of 1.*

reconstructed in the presence of a nearby companion or in a crowded field, this method results in more robust estimates of the total source flux – and hence Strehl ratio – than standard aperture photometry.
Table 5.1 summarises the measured Strehl ratios and FWHM of the radial profiles for ψ *Ser* at different image selection rates.

As already visible in the radial profile plots, an increase of the selection rate causes only moderate broadening of the PSF core's FWHM, but a stronger decrease of the resulting Strehl ratio due to more pronounced PSF wings.
Even at only 1% selection rate, the FWHM is considerably larger than theoretically expected. This is probably a result of the slight undersampling of the raw data. Simulations have shown that with the current setup and pipeline algorithms, the best FWHM to be expected is ≈95 mas.

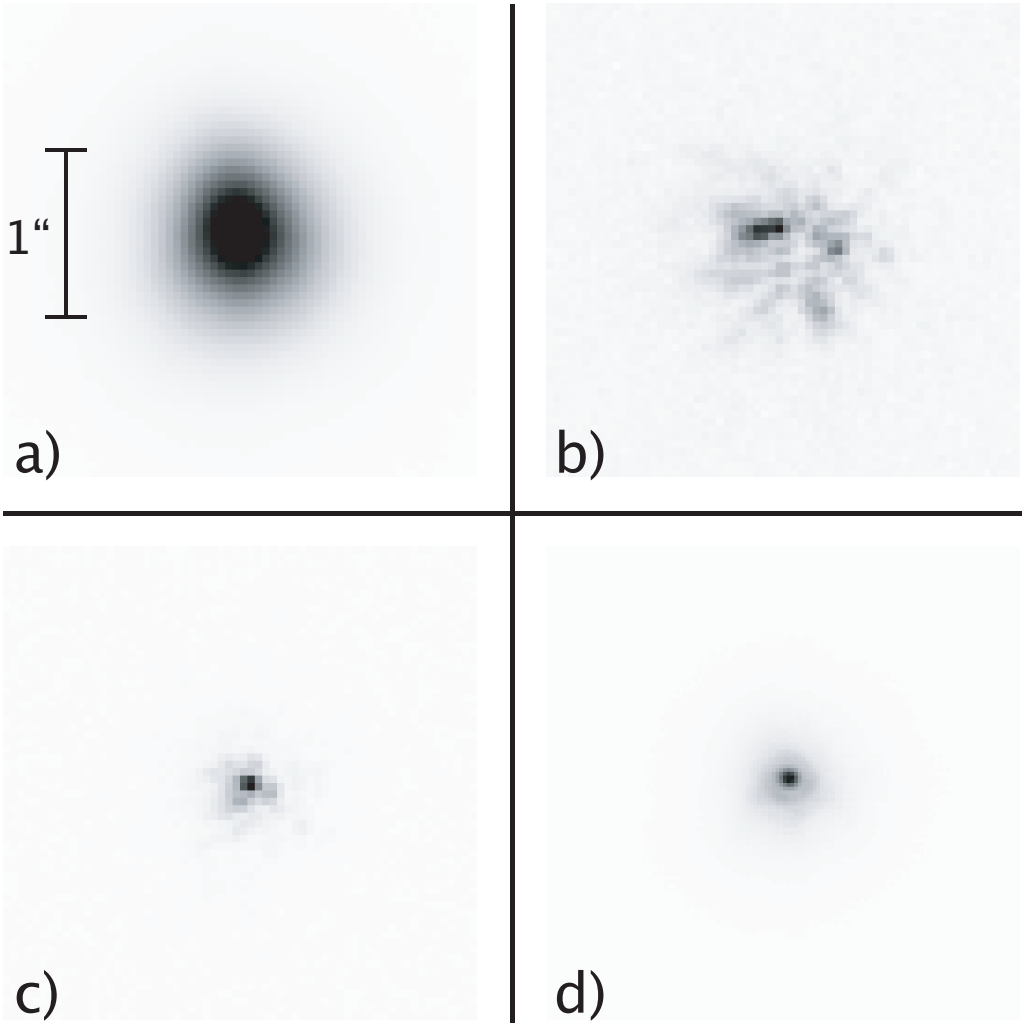

Figure 5.4. *Observations of* ψ Ser. **a)** *The seeing limited image with a FWHM of 0.″66 in SDSS z', corresponding to 0.″75 in the V-band.* **b)** *A typical single 15 ms exposure with a Strehl ratio of 8%.* **c)** *The best single image with a Strehl ratio of 37%.* **d)** *The Lucky Imaging result with a Strehl ratio of 14%, generated from the best 1% of 10000 input images. All images are linearly scaled.*

5.2.2 PSF Modelling

The additional broadening of the Lucky Imaging PSF core and the wings of the radial profiles can be modelled quite accurately as the weighted sum of a broad Moffat profile and a theoretical PSF that was convolved with a Gaussian:

$$\mathrm{PSF}_{\mathrm{obs}}(r) = W\left(\frac{1}{r^2/\sigma_{\mathrm{m}}^2 + 1}\right)^{\beta} + (1 - W)\left(\mathrm{PSF}_{\mathrm{th}}(r) * \exp\left(-\frac{r^2}{2\sigma_{\mathrm{g}}^2}\right)\right) \tag{5.1}$$

Here, W weights the two PSF components, β is the Moffat power law index (see Moffat (1969) for the original definition of the Moffat profile), and σ_g and σ_m define the widths of the Gaussian and Moffat profile, respectively. $\mathrm{PSF}_{\mathrm{obs}}$ and $\mathrm{PSF}_{\mathrm{th}}$ refer to the observed and theoretical radial PSF profiles. This semi-analytical model has been applied to the ψ *Ser* data presented above. The resulting fit parameters are given in Table 5.2, whereas Figure 5.5 shows the residuals.

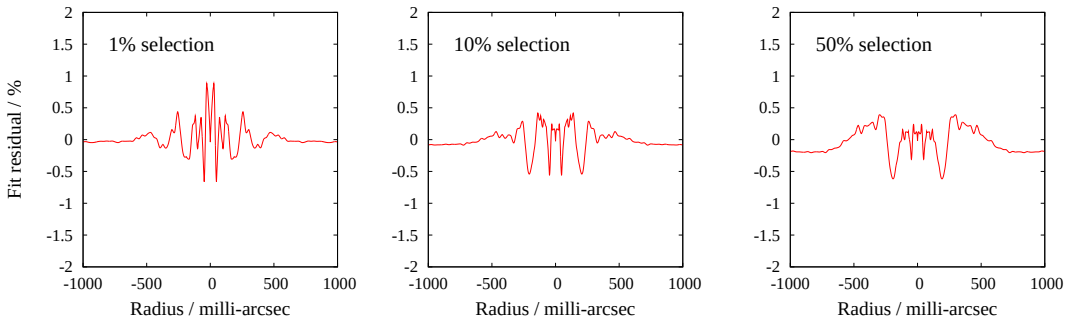

Figure 5.5. *Fit residuals for the application of the model described by Equation 5.1 to the radial profiles of the* ψ Ser *observations. The residuals are given in percent of the peak flux value.*

Table 5.2. *Semi-analytical PSF fit parameters for the* ψ Ser *observations.*

Selection rate	W	σ_g [mas]	σ_m [mas]	β
1%	0.25	23.8	250	1.62
10%	0.31	24.4	270	1.61
50%	0.36	24.7	300	1.63

While the weighting factor and the width of the Moffat profile vary considerably under changing selection percentages, the Moffat power law index and the width of the Gaussian convolution kernel keep nearly constant. The possibility to reconstruct the observed PSF profile from the known theoretical PSF and only two model parameters is particularly interesting for binary fitting and PSF subtraction applications. In larger fields, the dependency of the model parameters on the source position could be determined, allowing PSF based photometry in crowded fields like globular cluster centres.
Figure 5.5 shows that the available theoretical PSF does not reproduce the second diffraction ring correctly, leaving residuals of up to 0.5% at ≈230 mas distance from the PSF centre. This is possibly related to the method used for PSF simulation. Currently, the theoretical PSFs are computed for a circular aperture with central obstruction by the secondary mirror, but do not

include any contributions from the secondary spider or any optics behind the primary mirror. At least the simulated PSFs consider the filter transmission curve, the camera quantum efficiency, and the transmission profile of a model atmosphere.

The described model has been applied only in its radial symmetric form so far. Further developments could include asymmetries due to atmospheric dispersion, and it might be investigated if and how accurately the model parameters can be predicted based on the seeing-limited PSF only.

5.2.3 Impact of Natural Seeing

The radial profiles of single stars were extracted from observational data over a range of seeing conditions. While a Strehl ratio of more than 15% can be reached under a V-band seeing of $0\farcs75$ and better, it rapidly drops to a few percent if the seeing gets worse than $1''$. The radial profiles for a selection rate of 1% in the SDSS z' band and a single frame integration time of 15 ms are plotted in Figure 5.6 for four different seeing values. Table 5.3 lists the corresponding Strehl ratios and FWHM of the PSF cores.

As in the case of larger selection rates, an increase of the natural seeing leads in the first instance to more pronounced PSF wings and has only moderate effects on the FWHM of the PSF core.

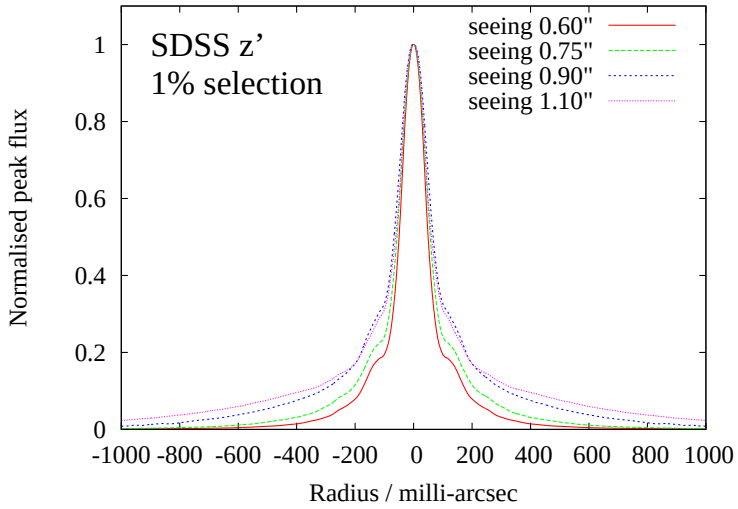

Figure 5.6. *Radial PSF profiles for different seeing conditions. All profiles refer to 1% selection from ≥10000 images with 15 ms single frame exposure time.*

V-band seeing $''$	D/r_0 z'-band	Strehl %	FWHM mas
0.6	6.5	22.4	98
0.75	8.1	14.2	114
0.9	9.6	7.1	119
1.1	12.2	5.2	122

Table 5.3. *Strehl ratios and PSF diameters for Lucky Imaging observations in the SDSS z' band under different seeing conditions. Ratios of the telescope diameter over r_0 at the observing wavelength are given in the second column. All values are valid for an image selection rate of 1% from typically 10000 images with 15 ms single frame exposure time.*

5.2.4 Wavelength Dependency of the PSF Profile

Since the probability for a good image in a series of short exposures decreases with larger $(D/r_0)^2$, observations in different filters should result in different Strehl ratios and PSF profiles. The close binary WDS 19070+1104 was observed in four filters with a constant single frame exposure time of 15 ms under a *V*-band seeing of 0.65 arcsec. The algorithm used for extraction of the radial profile of the brighter primary component effectively filters out the signal of the companion, and the results are comparable to measurements with single stars. Figure 5.7 contains the radial profiles for a selection rate of 1%, whereas Figure 5.8 shows the actual processed images. The corresponding Strehl ratios and PSF widths for a range of selection rates are given in Table 5.4.

Table 5.4. *Strehl ratios and PSF diameters for WDS 19070+1104A. Only the effective wavelengths of the filters are given in this table. Complete filter curves can be found in Chapter B.*

Filter	λ_{eff}	Strehl [%]			FWHM [mas]		
	[nm]	1%	10%	50%	1%	10%	50%
RG 610	768	5.6	4.4	3.5	178	218	282
Johnson I	873	14.0	10.8	8.0	112	120	136
SDSS z'	911	15.9	12.3	8.9	112	122	134
RG 1000	982	18.0	13.6	10.0	114	122	134

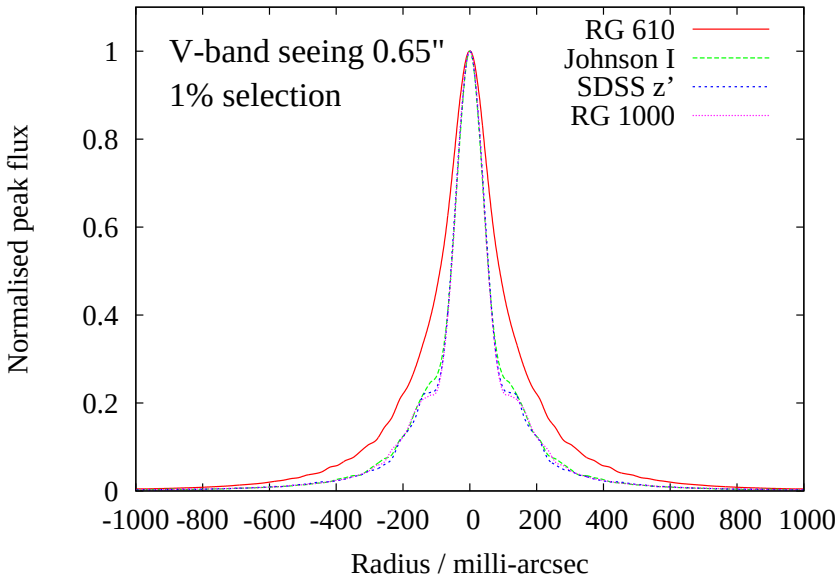

Figure 5.7. *Radial profiles of the primary component of WDS 19070+1104A for observations through four different filters. The 1% selection rate refers to 10000 input images with 15 ms single frame exposure time.*

Observing at longer wavelengths results in considerably better Strehl ratios without significant broadening of the PSF core[1]. There are only minor differences between the radial profiles, and the increase of the measured Strehl ratio mainly reflects the wavelength dependency of the theoretical resolution and PSF shape.

[1]This indicates that the broadening of the PSF core is attributed mainly to the finite sampling of the raw data and not the telescope's diffraction limit.

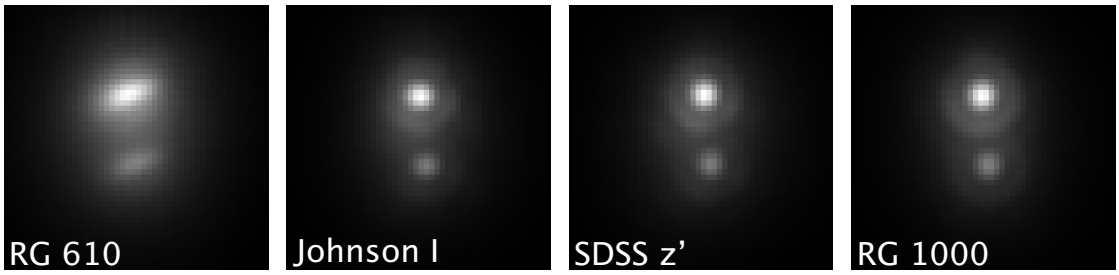

Figure 5.8. *The 300 mas separated double star WDS 19070+1104, imaged in four different filters. The field of view is 1×1″, East is up and North to the right. All images are linearly scaled. The observation through the RG 610 longpass filter shows strongly elongated PSFs due to atmospheric dispersion effects at a zenith angle of 27°.*

In practice, the longest useable wavelength is defined by the source brightness. Even so the RG 1000 filter provides the best results in this example, the camera's quantum efficiency at $\lambda > 1\,\mu$m and the filter throughput limit its use to objects brighter than $I \approx 9$ mag.
Observations at shorter wavelengths have been performed on few targets. Strehl ratios of more than 6% were never achieved at effective wavelengths ≤700 nm, and atmospheric dispersion effects limited the useable elevation range to >80°.

5.2.5 Atmospheric Dispersion Effects

In high angular resolution observations, the dependency of the atmosphere's refractive index on the wavelength can reduce the image quality. The atmosphere acts like a prism with a very low, but measurable dispersive power. Stellar PSFs appear as little spectra, elongated parallel to the parallactic angle, especially when observing at high zenith angles, at short wavelengths, or through filters with broad transmission profiles.
For dry air with a temperature of 15°C, the refractive index at sea level is given by Filippenko (1982) as:

$$(n(\lambda) - 1) \cdot 10^6 = 64.328 + \frac{29498.1}{146 - (1/\lambda)^2} + \frac{255.4}{41 - (1/\lambda)^2} \tag{5.2}$$

Precise calculations have to consider temperature, pressure, and humidity as well, and may even account for different fractions of carbon dioxide (e.g. Filippenko, 1982; Ciddor, 1996; Stone, 1996). The *observed* zenith angle z' of a monochromatic point source at a true zenith angle z due to atmospheric refraction is:

$$z' = \arcsin \frac{\sin z}{n} \tag{5.3}$$

Equations 5.2 and 5.3 together mean that blue light will experience more refraction than red light. If a polychromatic source is observed through the atmosphere, the light will be dispersed and its image is a small spectrum with the blue end pointing towards the zenith.

Figure 5.10 shows the amount of angular displacement for different wavelengths over a range of zenith angles. Wavelengths were chosen to allow the prediction of PSF broadening for observations through the SDSS r', i', and z' filters (see Fukugita et al. (1996) for the definition of the SDSS filter bandpasses). Figure 5.9 shows model PSFs for the Johnson I and SDSS z' filters. At z=45°, the I-band PSF is strongly elongated, and subtle dispersion effects are already visible at z=30°. Simulations at shorter wavelengths indicate that e.g. R-band observations are limited to

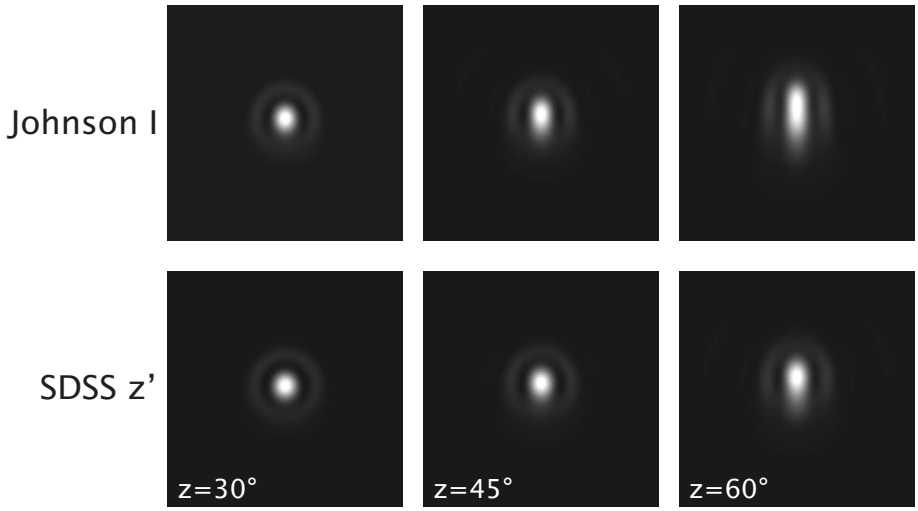

Figure 5.9. *Simulations of atmospheric dispersion effects at zenith angles of 30°, 45°, and 60 ° for observations through the SDSS* z' *and Johnson* I *filters. The parallactic angle is aligned with the vertical axis and the horizon is at the bottom. The field of view has a size of 1″×1″ and image scaling is linear.*

Figure 5.10. *Simulation of atmospheric dispersion effects for the SDSS* r', i', *and* z' *filters. An angular displacement of zero refers to the central wavelength of each filter, whereas the upper and lower curves give the angular displacement at the central wavelength plus/minus the filter bandpass half width at half maximum.*

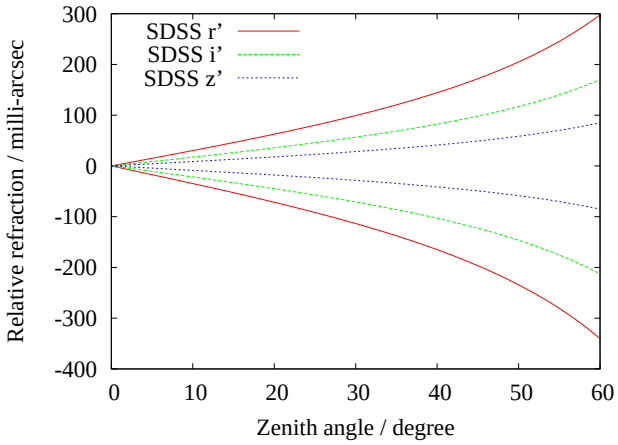

zenith angles smaller than 15°, whereas the PSF deformation is still acceptable at z=45° in the SDSS z' filter.

It is possible to build atmospheric dispersion correctors to restore full resolution over a wide range of wavelengths and zenith angles. These devices usually consist of a pair of rotating wedge prisms or meniscus lenses (e.g. Wynne, 1993; Phillips et al., 2006; Avila et al., 1997) and have been built for a large number of telescopes and instruments over the last decades. However, the design effort for adding a dispersion corrector to AstraLux was considered as too high to make this option really interesting.

5.3 Close Companion Detection Limits

The knowledge of detection limits for close companions to brighter stars is crucial for the evaluation of binarity surveys, or to determine the upper limits for the non-detection of a known companion.

Such limits were measured on final pipeline results of SDSS z' band observations under different seeing conditions. All observed stars had an I-band magnitude of ≈10 mag. The achievable magnitude differences for a 5σ peak detection are based on measurements of the noise in concentric rings around these stars. This method suffers from the low number of available pixels in the innermost 100 mas, but is quite robust at larger angular separations. Simulations with observed PSFs were carried out to check the reliability of the numerical results.
Figure 5.11 shows typical detection limit plots for three different V-band seeing values. As visible in the plots of radial profiles for different atmospheric conditions, the main differences occur in the wings of the PSF. At angular separations larger than 2″, the detection limit is determined by readout noise and the Poisson noise of the sky background. Using more input images, i.e. increasing the effective exposure time of the Lucky Imaging result, will increase the maximum achievable magnitude difference at large separations.

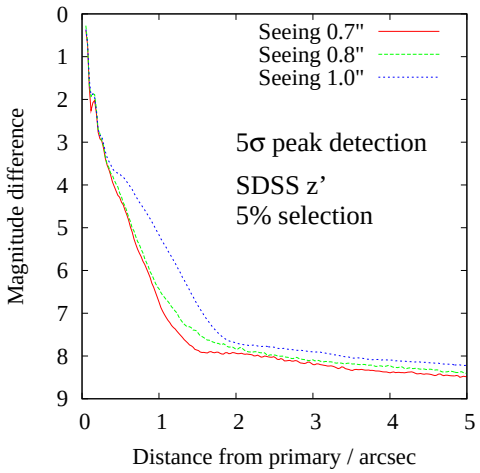

Figure 5.11. *Achievable magnitude differences for a 5σ peak detection of a fainter companion to the reference star. All curves refer to a 5% selection rate from 10000 input images with 30 ms single frame exposure time, resulting in an effective integration time of 15 s. The I-band magnitude of all three reference stars was ≈10 mag.*

Observational results impressively confirm these findings. Figure 5.12 shows the young active star EK *Dra* with its 4.6 mag fainter companion at an angular separation of 580 mas. This object has been extensively studied with near infrared speckle techniques by König et al. (2005) at the Calar Alto 3.5 m telescope. The AstraLux data is probably the first resolved observation at wavelengths <1 μm, and the photometric information is complementary to all published measurements.

Another remarkable result is shown in Figure 5.13. The brown dwarf multiple system GJ 569B is resolved into two components with only 90 mas angular separation. This system has been successfully observed only with adaptive optics in the near infrared so far and is believed to be a triple brown dwarf (Forrest et al., 1988; Simon et al., 2006). Preliminary photometric reduction of the AstraLux data supports this assumption. The host star GJ 569A at an angular separation of 4.″2 is ≈6.4 mag brighter than GJ 569B in the SDSS z' band and was used as the Lucky Imaging reference object for this observation.

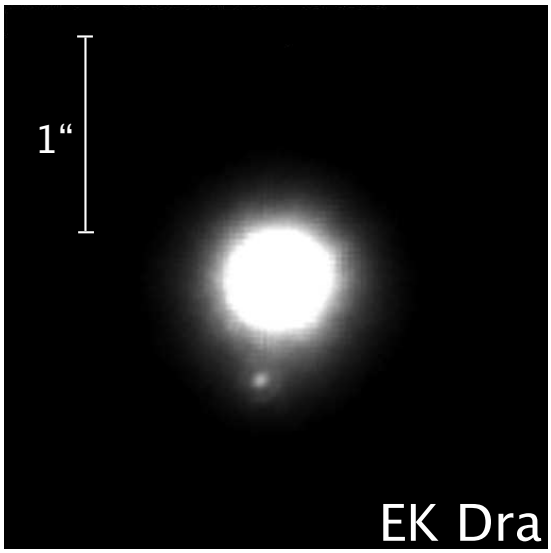

Figure 5.12. *AstraLux observation of the young active binary star EK* Dra *in the SDSS* z' *band. The image was generated from the best 2.5% of 10000 frames with 15 ms single frame exposure time. The brightness difference between the* I=*9.8 mag primary component and the 580 mas separated companion is 4.6 mag. North is up and East to the left.*

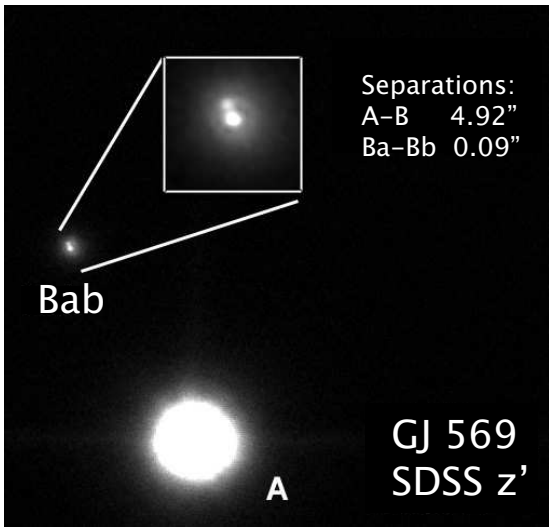

Figure 5.13. *AstraLux observation of the nearby (≈10 pc) M dwarf GJ 569A and its companion. GJ 569B itself is a multiple system and resolved into two components with only 90 mas separation. The brightness difference between GJ 569A and B is 6.4 mag in SDSS z'. This image is based on a 5% selection from 15000 frames with 15 ms exposure time each. North is up and East to the left.*

5.4 Temporal Characteristics

5.4.1 Telescope Tracking Errors

Most AstraLux observations at the Calar Alto 2.2 m telescope were hampered by periodic tracking errors of the telescope. They were visible on the real-time display as an oscillation of the object's position along the right ascension axis. Peak-to-peak amplitudes as large as 2″ were observed, depending on the position of the telescope on the sky. Figure 5.14 shows the distribution of the brightest pixel position of the reference star in an observation of the globular cluster M15. While atmospheric seeing is responsible for the scatter in declination, the telescope tracking error leads to a significant elongation of the distribution in right ascension.

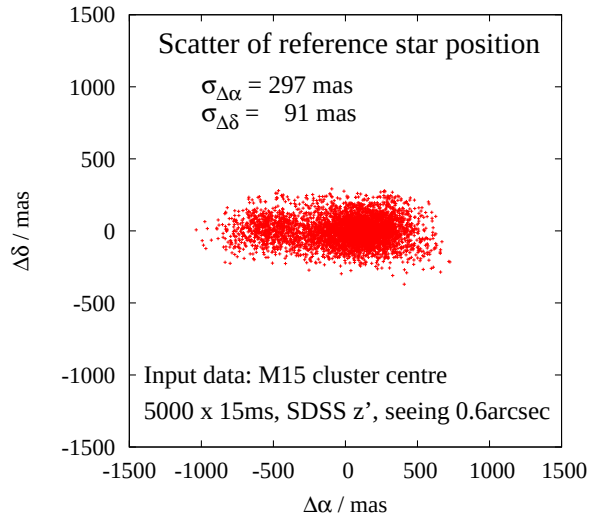

Figure 5.14. *Position of the reference star in a 5000×15 ms series of the M15 cluster centre. The positions are given as offset from the mean position in the tangential plane.*

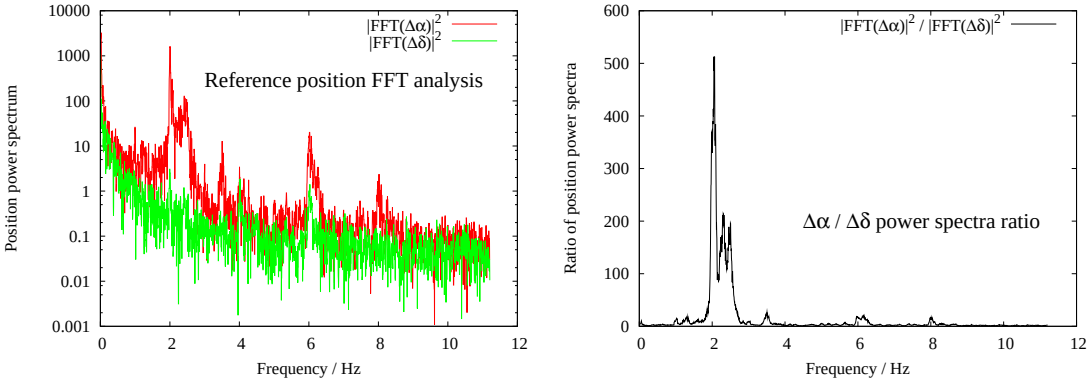

Figure 5.15. *Temporal analysis of the reference positions from Figure 5.14.* **Left:** *Logarithmic power spectra of the right ascension and declination component of the reference position motion.* **Right:** *Linear plot of the ratio of right ascension over declination power spectrum. The peak at ≈2 Hz is caused by periodic tracking errors of the telescope.*

A power spectrum analysis of the data – separately for declination and right ascension – is presented in Figure 5.15. The dominant peak at ≈2 Hz corresponds to the visual impression on the real-time display. There is significant crosstalk between the two motion axes at 4 Hz and 6 Hz, possibly related to resonances.

According to Calar Alto staff, the tracking problem seems to be less severe when heavier instruments like CAFOS or BUSCA are mounted on the telescope. However, experiments with an additional weight for AstraLux in January 2007 did not improve the oscillation behaviour.

5.4.2 Speckle and Strehl Coherence Times

A series of 10000 images of the bright star β *And* with a time resolution of 4.6 ms was used to investigate the temporal behaviour of speckle patterns. In a first approach, the intensity at a fixed pixel position was measured and Fourier transformed. This was repeated for 25 pixels around the brightness maximum in the seeing limited image, and the resulting power spectra were averaged to improve the signal-to-noise ratio. The result is plotted in Figure 5.16. According to Aime et al.

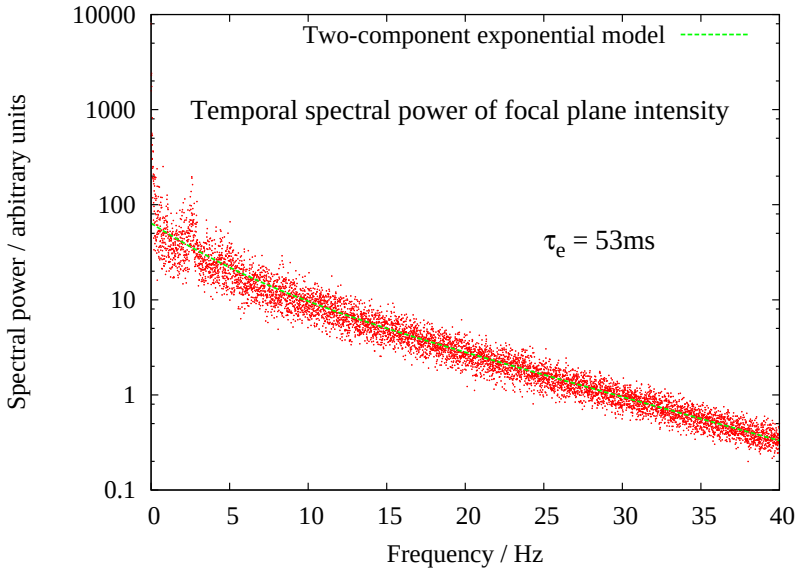

Figure 5.16. *Power spectrum of the focal plane intensity at a fixed pixel position, measured in the SDSS z' band with a time resolution of 4.6 ms. The data was fitted with a two-component exponential model to account for long-term drifts of the star's position due to tracking errors. The speckle coherence time τ_e=53 ms was derived from the high-frequent component of the fit.*

(1986), such a power spectrum P(ν) can be fitted as the sum of two exponential functions of the form:

$$P(\nu) = A \exp^{-a\nu} + B \exp^{-b\nu} \tag{5.4}$$

This two-component model accounts for excess power at low frequencies, caused e.g. by the telescope tracking error, and fits the high-frequent component which represents the temporal variability of the speckle pattern alone. Aime et al. (1986) showed that the slope of the high frequent part can be used to calculate the speckle coherence time τ_e, defined as the time where the autocorrelation function of the focal plane intensity drops to $1/e$. For the β *And* measurements, a value of τ_e=53 ms was derived[2].

The temporal autocorrelation plot for the same dataset is shown in Figure 5.17. The contribution of the 2 Hz telescope oscillation is well visible at time lags larger than 200 ms. Scaddan and Walker (1978) showed that such an autocorrelation function can be renormalised by subtracting a linear fit to the wings of the function and rescaling to a value range of 0...1. This is similar to the application of the two-component fit to the power spectrum above and removes influences of long-term variations. Such a "cleaned" autocorrelation function $C(t)$ can be fitted with a Lorentzian profile:

$$C(t) = \frac{a^2}{a^2 + t^2} \tag{5.5}$$

The speckle coherence time τ_e is then given by:

$$\tau_e = a\sqrt{e-1} \tag{5.6}$$

[2]This is valid under the assumption that the autocorrelation function of the focal plane intensity has a Lorentzian shape. In this case the slope of the power spectrum defines the equivalent width of the autocorrelation function and can be used to calculate the speckle coherence time.

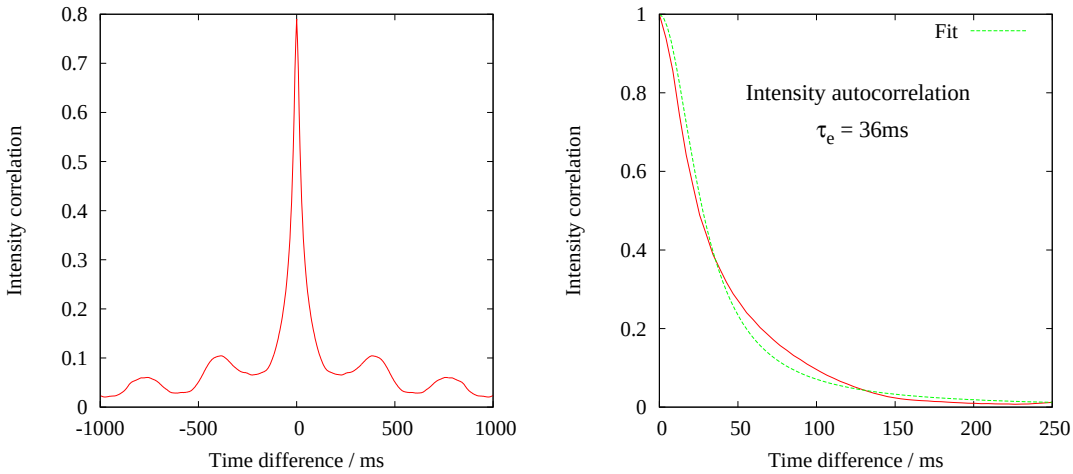

Figure 5.17. *Autocorrelation analysis of the focal plane intensity in a SDSS z' band observation with 4.6 ms time resolution.* **Left:** *Result for a time range of ±1 s. The sinusoidal wiggles in the wings of the autocorrelation profile are caused by periodic tracking errors of the telescope.* **Right:** *A close-up of the normalised autocorrelation function. The data was fitted with a model according to Equation 5.5, resulting in an estimated speckle coherence time of τ_e=36 ms.*

The right side of Figure 5.17 shows a Lorentzian fit to the renormalised autocorrelation data. The measured τ_e is 36 ms, only two third of the value derived by power spectrum analysis. This difference is most likely caused by residuals of the telescope oscillation in the autocorrelation data.

The telescope's tracking error has a measurable impact on the achievable Lucky Imaging data quality. The maximum useful single frame exposure time for Lucky Imaging at the Calar Alto 2.2 m telescope is not only limited by atmospheric turbulence, but additionally reduced by the telescope performance itself. A simple estimate confirms this: if the telescope oscillation has a peak-to-peak amplitude of 2″ and a frequency of 2 Hz, this results in changes of the object's pixel position with a speed of up to 160 px/s. This corresponds to a PSF broadening by ≈110 mas at a single frame exposure time of 15 ms. While these extreme oscillations do usually not occur permanently during an observation, they will decrease the fraction of high quality exposures that can be used for the final Lucky Imaging result.

The derived speckle coherence time of τ_e=53 ms is comparable to timescales published by other authors. Tubbs (2003) measured a value of 65 ms at the Nordic Optical Telescope, and values in the range from few milliseconds to several ten milliseconds were reported by e.g. Roddier et al. (1990), Vernin and Munoz-Tunon (1994), and Dainty et al. (1981).

5.4.3 Strehl Correlation

The spatial and temporal correlation of Strehl ratios was measured for the two components of WDS 22280+5742 (see Figure 5.18 for a seeing limited image, single frame examples, and the Lucky imaging result).

The left side of Figure 5.19 shows a plot of the Strehl ratio of the secondary component versus the Strehl ratio of the primary. Without noise and in the absence of any anisoplanatic effects, the two values should be perfectly correlated. The real measurement has a linear correlation coefficient

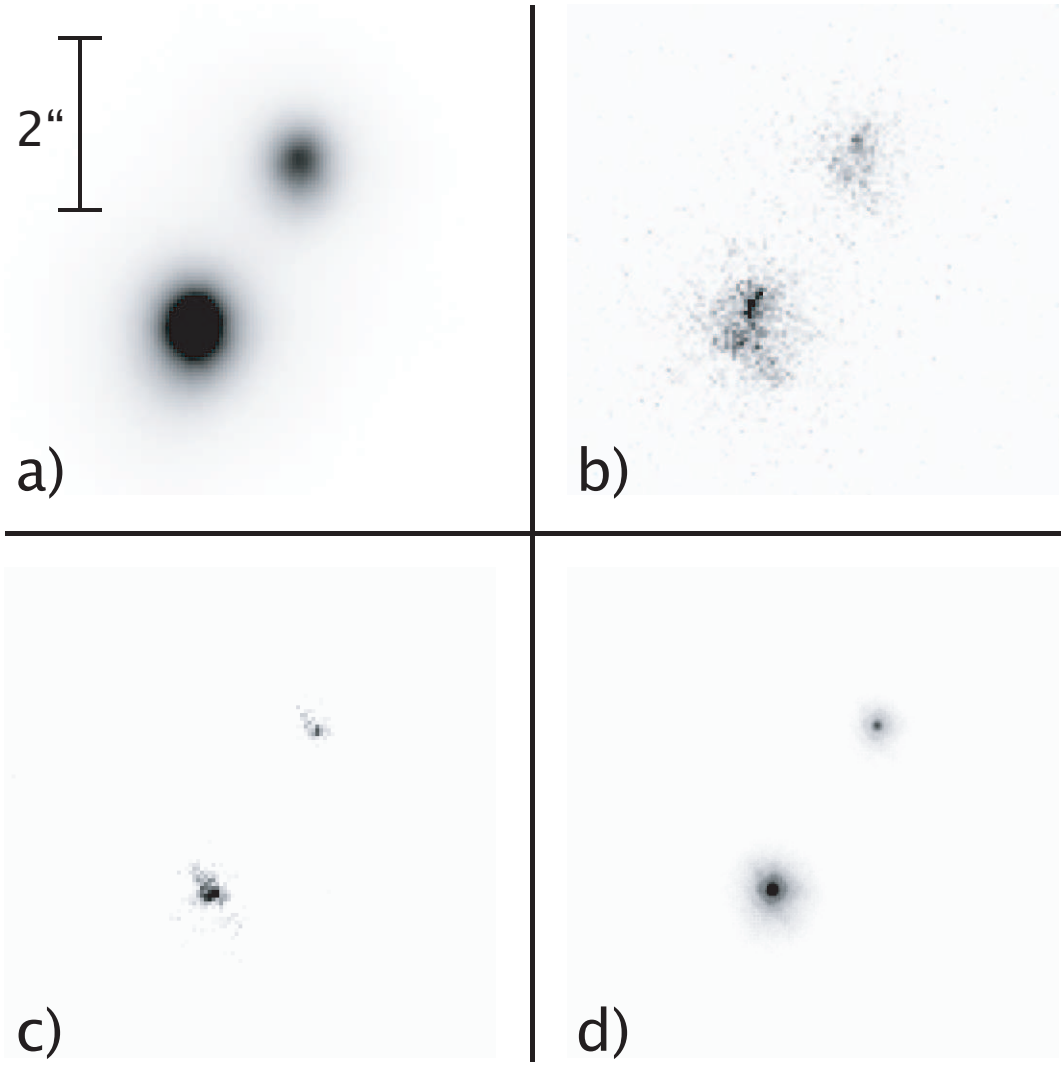

Figure 5.18. *Observations of the 2.″4 separated double star WDS 22280+5742.* **a)** *The seeing limited image with a FWHM of 0.″68 in SDSS z', corresponding to 0.″77 in the V-band.* **b)** *A typical single 14.7 ms exposure with a Strehl ratio of 0.09.* **c)** *The best single image with a Strehl ratio of 0.27.* **d)** *The Lucky Imaging result with a Strehl ratio of 0.15, generated from the best 2.5% of 5000 input images. All images are linearly scaled up to saturation. East is up and North to the right.*

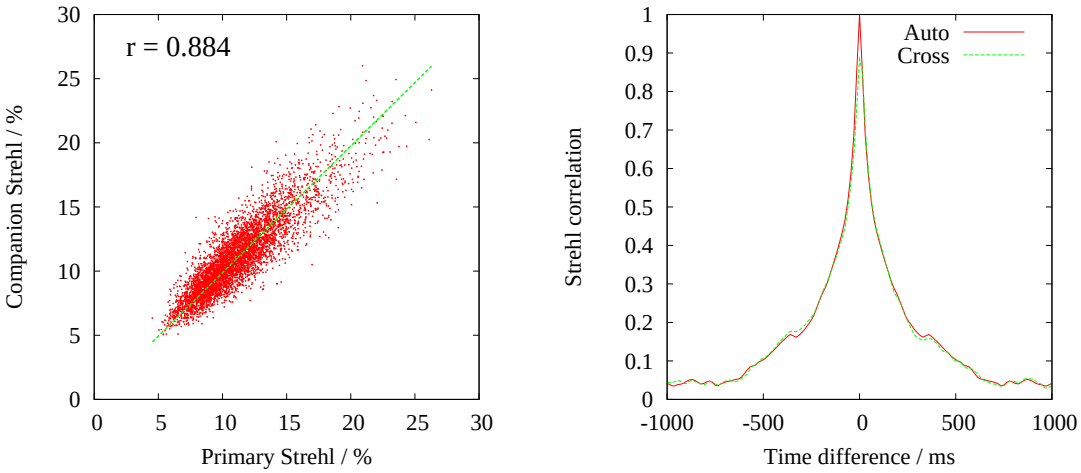

Figure 5.19. *Strehl ratio analysis for WDS 22280+5742.* **Left:** *Plot of the primary component's Strehl ratio versus the measurement for the fainter companion. The line is a linear fit with a slope of 1. The linear regression coefficient for this dataset is r=0.884.* **Right:** *The temporal auto-correlation of the primary's Strehl ratio is plotted in red, whereas the green line is the cross-correlation between the Strehl ratios of both components.*

of 0.884, and the RMS for a linear fit is ≈5%, expressed in Strehl ratio. The autocorrelation of the primary's Strehl ratio (see right side of Figure 5.19) indicates a coherence time of ≈150 ms. This implies that the image quality, or the total variance of the incoming wavefront, changes on a longer timescale than the position of the brightest speckle – the speckle coherence time above was in the order of 50 ms.
This is consistent with the assumption that telescope motion contributes to the focal plane intensity autocorrelation, and related to the fact that low-order wavefront aberrations, i.e. tip-tilt image motion, contribute mostly to atmospheric seeing. This finding could be exploited to improve Strehl measurements of faint reference stars in the pipeline process. The single exposures could be rebinned in groups equivalent to 150 ms exposure time and recentred on the individual peak positions to increase the signal-to-noise ratio of the Strehl ratio estimates.

The shape of the temporal cross-correlation of the Strehl ratios for both components is remarkably similar to the auto-correlation, indicating that the isoplanatic angle has to be much larger than the component separation of 2.″4. The cross-correlation peaks at a time lag of 0 ms, but is slightly skewed with respect to the auto-correlation curve. A detailed analysis of such subtle differences for double stars with a range of separations and position angles could in principle be used to derive wind-speed profiles of the atmosphere's turbulent layers.

5.5 Observations of Globular Clusters

AstraLux observations of globular cluster centres enabled the characterisation of the image quality over the full field of view. Choosing different stars with a wide range of magnitudes as the Lucky Imaging reference allowed to estimate brightness limits for the reference selection and to measure the dependency of the Strehl ratio on the reference magnitude. Among the globular clusters M3, M13, and M15, the latter has been observed most extensively with AstraLux. Figure 5.20 shows a Lucky Imaging result together with a close-up of the central region and a

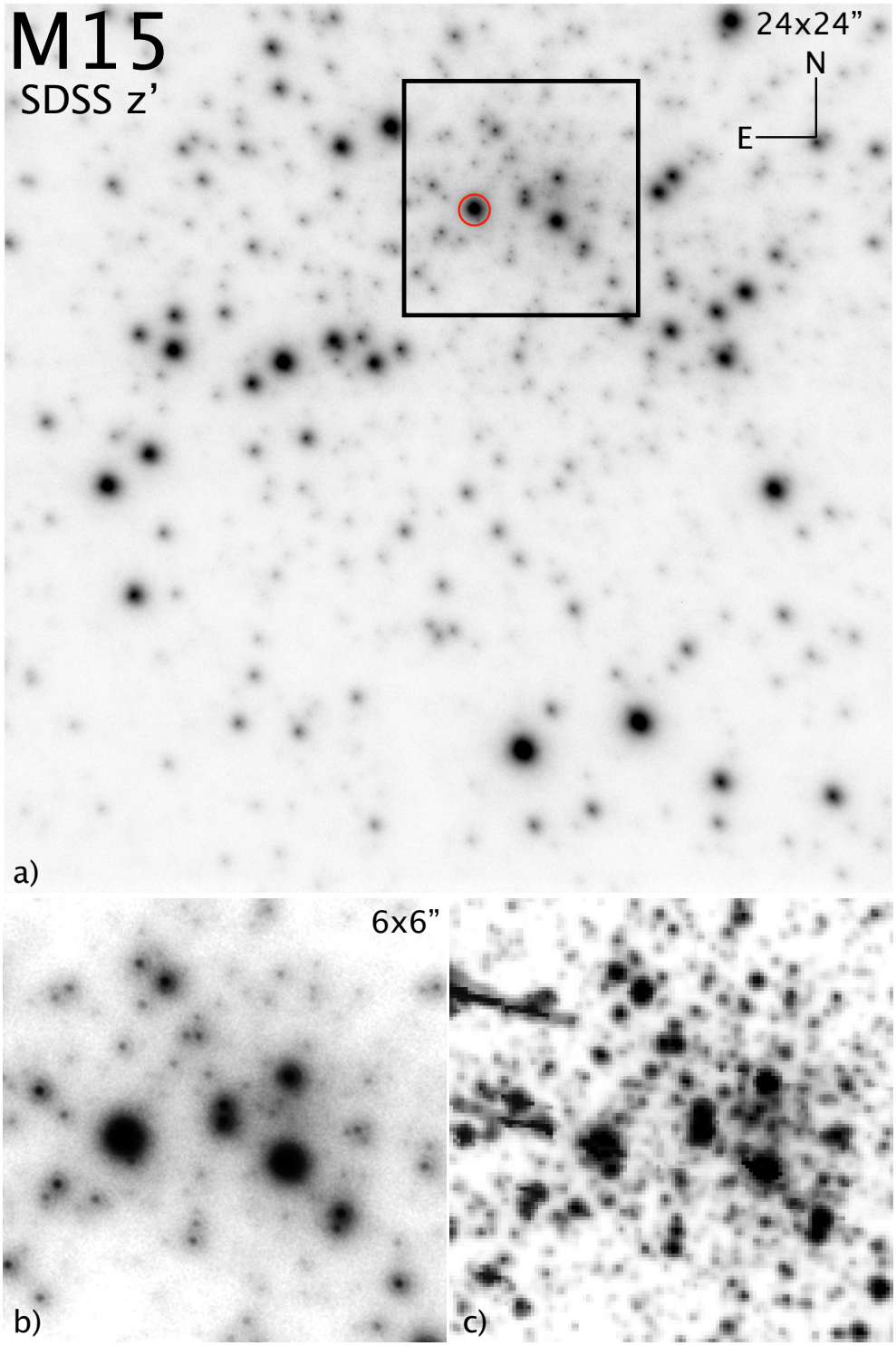

Figure 5.20. *The centre of the globular cluster M15 (NGC 7078).* **a)***The 10% Lucky Imaging result from 10000 raw images with 30 ms single frame exposure time in the SDSS* z' *filter. The effective integration time is 30 s. The red circle marks the star used as the Lucky Imaging reference.* **b)** *The inner 6×6″ of the centre, as marked by the black rectangle in the larger image.* **c)** *A HST archive image of the same region, taken with the Advanced Camera for Surveys (ACS/WFC) in the F814W filter. The total integration time was 615 s.*

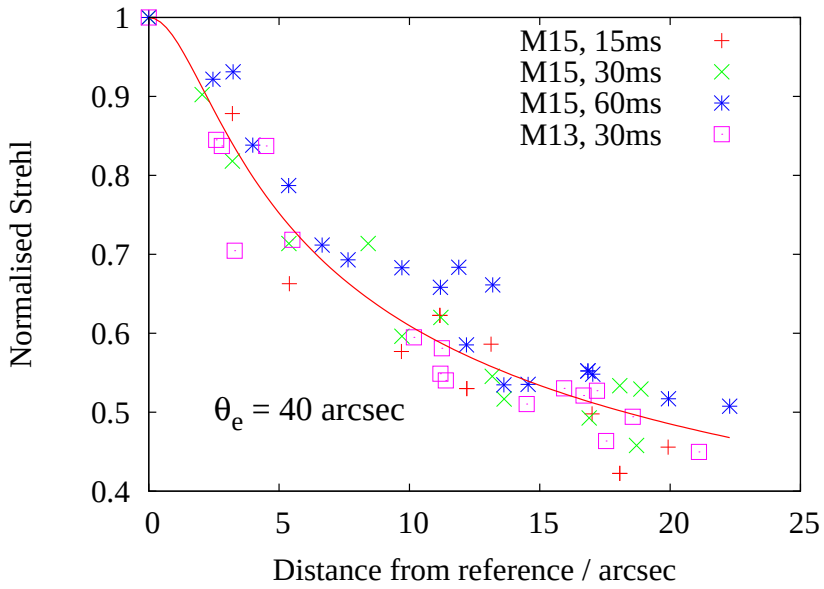

Figure 5.21. *Normalised Strehl ratios versus angular separation from the reference source for various single frame exposure times. All values refer to globular cluster observations in the SDSS z' band and a 1% image selection rate. The given isoplanatic angle of* θ_e*=40″ was derived by fitting a Moffat profile (red line).*

Hubble Space Telescope (HST) archive image for comparison. Stars as faint as I=18 mag can be detected in the AstraLux data, close to the confusion limit in such a dense cluster core. The effective integration time of the AstraLux result was 30 s, whereas the HST image has a total exposure time of 615 s, more than 20 times longer. An astrometric reduction of the AstraLux data is presented in Chapter 6.

5.5.1 Isoplanatic Angle

In the following, the isoplanatic angle θ_e is defined as the angular separation from the reference star, where the observed Strehl ratio drops to the fraction 1/e of the reference star's Strehl ratio. The observations of globular cluster centres allowed measurements of the Strehl ratio for a large number of stars, well distributed over the field of view. Figure 5.21 shows the normalised Strehl ratios, i.e. the measured Strehl ratios divided by the reference Strehl, for three different M15 and one M13 observation. The images used for this plot are based on a 1% selection from 10000 frames in the SDSS z' band. M15 was observed with three different single frame exposure times, without a significant impact on the *normalised* Strehl ratios. The *absolute* Strehl ratio slightly decreases with increasing exposure time, though, dropping from ≈22% at 15 ms to 18% at 60 ms.

Principally, like in the case of temporal autocorrelation data, a Lorentzian function should provide a good fit to the normalised Strehl ratio (e.g. Tubbs, 2003). However, the experimental data is only poorly reproduced by such a profile. For the measurements shown in Figure 5.21, a Moffat profile has been found to give good fit results, allowing extrapolation to the 1/e point, and hence an estimate of the isoplanatic angle θ_e. For the SDSS z' band observations, θ_e has been found to be ≈40″, larger than the diagonal field of view size of 34″.

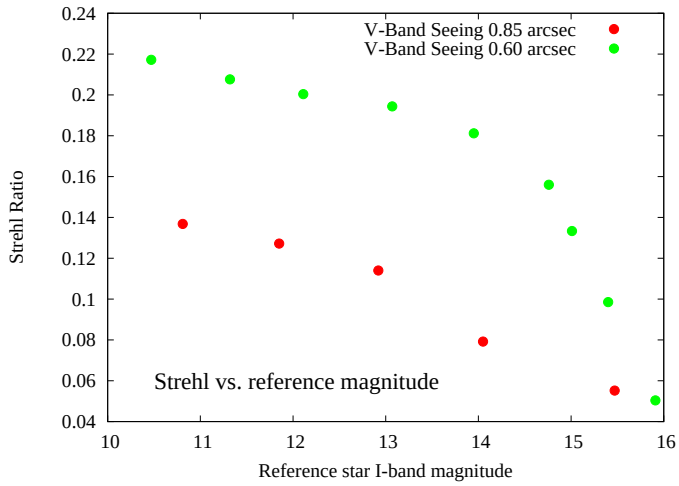

Figure 5.22. *Dependency of the final Strehl ratio on natural seeing and reference star magnitude. The plot is valid for observations with 30 ms single frame exposure times in SDSS z' and 1% image selection rate. All Strehl ratios were measured on stars that were less than 2″ separated from the reference source.*

This measurement has been repeated for an observation of M15 in the Johnson *I* band. No significant difference between the isoplanatic angles extrapolated from the z' and *I* band data was found. Theory predicts a decrease of θ_e by a factor 1.05 when switching from z' to *I*-band, too small to be reliably detected in the available data.

The expected isoplanatic angle in *V*-band is ≈2-5″ (e.g. Roddier et al., 1982; Ziad et al., 2005), equivalent to ≈4-10″ in the z'-band. Vernin and Munoz-Tunon (1994) have found that the isoplanatic angle in speckle observations is typically about 1.7 times larger.
The AstraLux data and comparable measurements by Tubbs (2003) suggest that the selection process of the Lucky Imaging technique can further increase θ_e to values as large as 40−50″.

5.5.2 Reference Star Limiting Magnitude

The M13 and M15 observations were re-analysed with different choices of the Lucky Imaging reference star to assess the impact of the reference magnitude on the final Strehl ratio. Figure 5.22 shows the results for measurements under two different seeing conditions. While reference stars as faint as *I*=15.5 mag still allow a substantial improvement of image quality under a 0.″65 seeing, the same performance cannot be reached with stars fainter than 13.5 mag in 0.″85 seeing.

5.6 Conclusions

AstraLux is able to reach Strehl ratios as high as 25% at the Calar Alto 2.2 m telescope in the *I*-band. While this is only possible under a superior seeing of 0.″6 or better, the median Calar Alto seeing of 0.″9 still allows to achieve Strehl ratios of more than 10%. The typical seeing limited Strehl ratio in SDSS z' under such conditions is ≈1.1%. In general, Lucky Imaging provides an improvement of the Strehl ratio by a factor of 10, corresponding to an increase of the signal-to-noise ratio for point sources by a factor of 10−20, depending on atmospheric conditions. Thus a selection of only the best 5−10% of all images does not have a negative effect on the detection limit for point sources.

The requirements for the reference star magnitude are similar as for observations with adaptive optics. The performance starts to significantly decrease at I=14 mag, but improvements of the image quality are still possible with stars as faint as 15−16 mag. The measured isoplanatic angle in I-band is with $\approx$40″ as large as typical values in K-band for adaptive optics observations. This means that Lucky Imaging with AstraLux at the Calar Alto 2.2 m telescope provides the same sky coverage as adaptive optics observations in the near infrared at e.g. the 3.5 m telescope.
Lucky Imaging performs considerably better than speckle imaging techniques. The typical magnitude limit for these methods is $V\approx$12 mag, and the isoplanatic angle in I-band is only half as large.

The measured close companion detection limit at an angular separation of 1″ is on average 6 mag. This is worse compared to the performance of AO systems, where usually 8−10 mag are reached (e.g. Mugrauer et al., 2005). But: adaptive optics provides this capability only in the H and K-band at wavelengths >1.5 μm. The achievable contrast ratio in speckle imaging observations is typically two magnitudes less than for Lucky Imaging.

Single frame exposures are limited to integration times below the speckle coherence time of $\approx$50 ms in SDSS z'. At these exposure times, image motion due to periodic errors of the telescope tracking is expected to reduce the percentage of usable frames. This is a serious technical problem that needs to be addressed to increase AstraLux's performance in the future.

Still, the early measurements indicate that AstraLux is comparable to LuckyCam at the Nordic Optical Telescope in terms of limiting magnitude and isoplanatic angle (see Tubbs (2003)).
Detector, optics, electronics, and software worked as expected. The simple design of the instrument certainly contributed to a smooth and satisfactory start of observations at Calar Alto.

Chapter 6

Astrometric Calibration of AstraLux

6.1 Introduction

One of the most easily accessible results from Lucky Imaging data is relative astrometry, i.e. angular separations and position angles (PA) between two or more objects in the same image. In contrast to absolute astrometry, where object positions are referenced to a frame of astrometric calibrators, e.g. the FK4/5 or ICRS standard system, relative astrometry requires only the precise knowledge of pixel scale and rotation angle of the instrument.

These two values have to be calibrated at least for each observing run, and definitely after any changes of the optical configuration or un- and remounting of the camera. Optimally, pixel scale and rotation angle should be monitored for changes during the observing run, preferably several times per night.

The pixel scale and PA calibration determines the actual precision of any following astrometric measurements. It is therefore important to choose calibration methods that yield accurate results and reliable error estimates. Ideally, they should not require additional instrumental effort, and should not consume too much valuable observing time.

In principle it is possible to use single stars for calibration purposes by observing them through a slit mask placed in front of the telescope. Measurements of the resulting interference pattern in the image plane allow precise pixel scale and rotation angle calibration if the true dimensions of the slits and their orientation with respect to the polar axis of the telescope are known. This method has been described by e.g. McAlister (1977), McAlister et al. (1987), Hartkopf et al. (1997), and Douglass et al. (1997) and is widely used at smaller telescopes. For the Calar Alto 2.2 m telescope, such a slit mask would be a very unwieldy device, and (un)mounting it would consume too much time and manpower to make it a really feasible solution.

Two different calibration methods that were applied to AstraLux will be described in the following. A third method, based on measuring the angular motion of well-observed asteroids relative to field stars, was tested in January 2007, but has not been fully evaluated yet. This technique should in principle allow to calibrate the linear pixel scale with an accuracy better than 0.01%, and is virtually free of systematic errors.

6.2 Known Visual Binaries

Visual binaries with known angular separations and position angles are well-distributed over the sky, and it is always possible to find one observable at a sufficient elevation. However, not any of the several 1000 known binaries is suitable for calibration purposes. For most of them only few measurements and preliminary orbital elements exist, so that ephemerides for these systems are rather inaccurate.
A subset of the stars contained in the "Sixth Catalog of Orbits of Visual Binary Stars" (Hartkopf and Mason, 2006) has been proposed as astrometric "calibration candidates". For these ≈200 stars the existing astrometric data covers either at least a substantial fraction of the full orbit, or the orbital period is long enough to allow precise predictions of separation and position angle for the next few years. The ephemerides for these objects are published online, and the selection of a suitable calibration star sample can be accomplished in short time.
The major drawback of these objects is, that the published orbits are usually based on measurements of only few different observers, so that systematic errors in one of the data sources will most likely persist and not be averaged out. Furthermore, there is no common astrometric calibration standard used by these observers.

Table 6.1. *November 2006 calibration binary measurements. The standard deviation σ refers to single measurements, not the mean value. The rotation angle gives the difference of the measured position angle minus the prediction, where the position angle is counted from North over East.*

Star	Separation [″]	Pixel scale [″/px]	Rotation [°]	N_{meas}
WDS 00057+4549	5.955	23.206	-0.89	1
WDS 02020+0246	1.788	23.171 ± 0.051	+1.71 ± 0.051	8
WDS 03368+0035	6.686	23.720	-0.43	1
WDS 04233+1123	1.088	22.717	+1.31	1
WDS 05005+0506	1.453	22.899	-0.41	1
WDS 05364+2200	4.114	23.998 ± 0.067	-1.34 ± 0.10	10
WDS 07201+2159	5.645	23.548	-0.47	1
WDS 07461+2107	0.491	25.959 ± 0.138	-0.45 ± 0.25	2
WDS 08554+7048	1.973	23.186 ± 0.028	-1.09 ± 0.04	2
WDS 17053+5428	2.311	23.232	+1.27	1
WDS 17386+5546	1.915	22.744	+1.38	1
WDS 18443+3940	2.360	23.672	+0.09	1
WDS 19121+4951	7.388	23.838	-0.46	1
WDS 19266+2719	2.083	23.361	-0.46	1
WDS 19450+4508	2.655	23.750	-1.26	1
WDS 19553-0644	0.555	24.262	-0.69	1
WDS 20375+1436	0.543	24.974	-1.71	1
WDS 20462+1554	6.128	23.821	-0.95	1
WDS 20467+1607	9.133	23.805	-0.07	1
WDS 21441+2845	1.716	22.540	-2.53	1
WDS 22038+6438	8.304	24.655 ± 0.069	+0.40 ± 0.07	3
WDS 23595+3343	2.076	22.346 ± 0.034	-0.08 ± 0.05	16

Observations of such calibration candidates were carried out in all three AstraLux observing runs. During the first night of each run, around 20 different calibrators were imaged to determine initial pixel scale and image rotation values. About 3−4 stars of the sample were used throughout the remaining nights to check for variations of the pixel scale, typically by observing one standard per hour. On all reduced images, the star positions were extracted by Gaussian fitting, and pixel scale and rotation angle were computed for each image individually, based on the ephemeris prediction for angular separation and position angle. All stars were observed at elevations >50° and no attempt has been made to correct for differential refraction or atmospheric dispersion.
Table 6.1 lists the calibration measurements of the November 2006 observing run, while the derived pixel scales are plotted against the angular separations in Figure 6.1. The pixel scale refers to the pipeline results which are two times oversampled compared to the raw data. A look at the table reveals that the scatter between the individual pixel scales is much larger than the typical accuracy derived from repeated measurements of the same star. On one hand, the 16 measurements of WDS 23595+3343 show a standard deviation of the pixel scale of only 0.034″/px, which indicates a relative accuracy of 0.15%. At an angular separation of 2.″076, this corresponds to an astrometric precision of 3.1 mas. On the other hand, the standard deviation of all pixel scale values is 0.″838 or 3.6% – this is a factor of 24 worse! One reason for this is

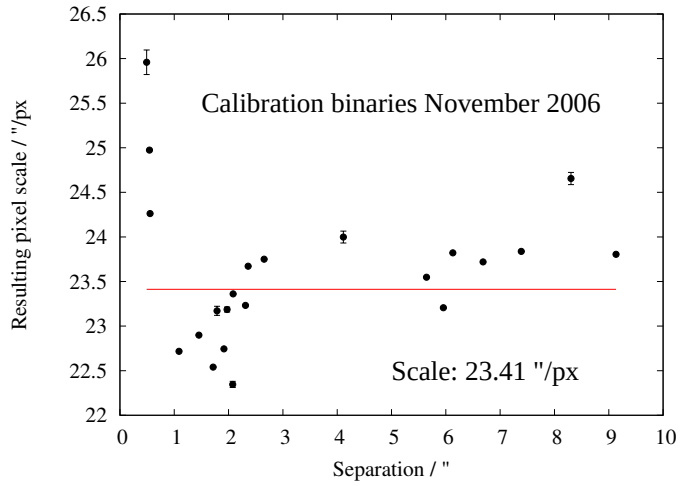

Figure 6.1. *Resulting pixel scale versus angular separation for all November 2006 calibration binaries. Dots with error bars refer to stars with multiple measurements. The adopted pixel scale of 23.41″/pixel is based on all binaries with separations >1″, excluding the lowest and highest value.*

visible in Figure 6.1. Apparently, the three calibrators with angular separations below 1″ result in higher pixel scale values than the average. This is caused by the beginning overlap of the seeing halos at small separations, resulting in systematic underestimates of the separation when using Gaussian fits instead of sophisticated PSF subtraction methods. For the final reduction, only stars with separations >1″ were used, and the two most extreme outliers were also discarded. From the remaining 17 stars a pixel scale of 23.41±0.13″/px was derived, where the standard deviation now refers to the mean value and not single measurements. This implies that any observation based on this calibration is limited to a relative accuracy of 0.56% in separation – still worse than the result for a single calibration star.

The same is true for the rotation angle. While the measurements of WDS 23595+3343 show a standard deviation of only 0.05°, the uncertainty for the finally adopted value of -0.2° is about four times higher. Though this precision is already quite satisfying for angle measurements and indicates that the 2.2 m telescope seems to be well-aligned to the celestial pole, it shows again that the calibration accuracy is not limited by the instrumental stability, but by the uncertainties of the true separations and position angles of the calibrators.

Since all the stars in this sample are supposed to be well-observed and to have high-precision orbital elements, there is no way to decide which one is the best or most accurate. If a calibration strategy is based on known binaries, it is therefore highly recommended to observe as many of these objects as possible to average out any inherent uncertainties.

6.3 Stellar Clusters

Using stellar clusters for calibration purposes is pretty close to the astrometric reduction of wide-field observations. The main ingredient for this method is an accurate catalogue of the astrometric positions of stars in the field of view. Catalogues like the UCAC-2 or the USNO-A2.0 and USNO-B1.0 provide astrometric information for more than a billion stars, allowing high-quality astrometry in virtually any region of the sky. But: this refers to instruments with fields of view in the order of several arcminutes – in the $24'' \times 24''$ field provided by AstraLux, one will rarely see more than two or three stars at the same time. For this reason, multiple-object calibration can be performed only in dense stellar clusters, e.g. globular cluster centres or the Orion Trapezium cluster. Astrometric information for these objects cannot be extracted from one of the standard catalogues mentioned above, but is available in separate publications. For example, globular cluster astrometry of M3, M13, and M15 was published by Guhathakurta et al. (1994), Yanny et al. (1994), and Cohen et al. (1997), based on HST observations. Accurate ground-based astrometry of the Orion Trapezium cluster stars is given by McCaughrean and Stauffer (1994).

The astrometric reduction of AstraLux images of stellar clusters follows the same method as for wide-field astrometry. First, the positions of all stars with a suitable SNR and preferably no close companions are extracted from the image. Second, these stars are matched to their corresponding entries in the astrometric catalogue of the observed object. This leaves the task to determine the transform from pixel coordinates (x,y) to equatorial coordinates (α,δ). At this point it is convenient to switch the coordinate system from equatorial to tangent plane coordinates (ξ,η):

$$\xi = -\frac{\cos\delta \sin(\alpha - \alpha_0)}{s} \tag{6.1}$$

$$\eta = -\frac{\sin\delta_0 \cos\delta \cos(\alpha - \alpha_0) - \cos\delta_0 \sin\delta}{s} \tag{6.2}$$

$$s = \cos\delta_0 \cos\delta \cos(\alpha - \alpha_0) + \sin\delta_0 \sin\delta \tag{6.3}$$

Here, α_0 and δ_0 are the equatorial coordinates of the image centre, and s is a shorthand to make the equations more handy. The transform between tangent plane coordinates and pixel position (x,y) in the image can be expressed by the following equations:

$$\xi = a + bx + cy + dx^2 + ey^2 \tag{6.4}$$

$$\eta = g + hx + iy + jx^2 + ky^2 \tag{6.5}$$

These equations include offsets between true and assumed plate centre (coefficients a, g), the linear pixel scale and image rotation (b, c, h, i), and quadratic terms of the pixel scale that can

account for image distortions (d, e, j, k). It is possible to use a reduced set of transform equations with a single linear pixel scale coefficient and rotation angle, if only two stars are available. In principle the above equations can also be extended by additional 3rd order terms. The resulting linear equation system is solved, e.g. by singular value decomposition, to determine the values of the transform coefficients. From these, the linear pixel scale and the rotation angle of the image can then be computed as:

$$Scale = \sqrt{|bi - hc|} \tag{6.6}$$

$$Angle = \arctan \sqrt{\frac{-ch}{bi}} \tag{6.7}$$

6.3.1 The Centre of M15

This technique has been applied to AstraLux images of the globular cluster M15, obtained during the first observing run in July 2006. The input data was a 10% selection result from 10000 single frames with an effective exposure time of 30 s in the SDSS z' filter. The reduced result was two times oversampled by the Drizzle process during image reconstruction. The astrometric reduction was based on the HST astrometry given by Yanny et al. (1994).
A small piece of software was written that displays the image on the screen and overplots the positions of the reference stars from the catalogue, using preliminary transform coefficients. When the user clicks on a star in the image, the centroid is determined and matched to the nearest available reference star. The transform equations are solved and the residuals for each star are computed. A κσ-clipping algorithm is applied to exclude outliers from the final solution. Figure 6.2 shows the image used for the M15 astrometric reduction. Stars included in the solution are encircled in green, while removed outliers are marked by a red box. The red lines indicate the amount and direction of the astrometric residuals, the line length is 25 times the actual displacement between catalogue position and fit result. Five relatively bright stars in the southwest corner of the field of view were not used at all since they appear twice in the catalogue of Yanny et al. (1994), with differences of around ≈100 mas between the alternative positions. These stars are in the overlap area of the HST images used for catalogue creation, and were not correctly matched between the individual frames. From a total of 106 selected stars, 9 were rejected due to their residuals.
The remaining 97 stars allowed a stable solution of the transform equations. The actual results of the analysis are summarised in Table 6.2. Please note that these values again refer to the pixel scale of the drizzled data which is two times oversampled compared to the raw data.

Compared to the double star measurements, the degree of achievable precision is impressive: the relative uncertainty in pixel scale is now only 0.03%. The quadratic terms are of the same order of magnitude as their errors, but not negligible. The determined values correspond to deviations from a purely linear solution by ≈20 mas at the field edges. This is certainly relevant for applications that need high astrometric precision over the complete field of view, whereas observations of e.g. close binaries may be safely calibrated using a linear fit.

It is interesting to compare the above results to the calibration that was performed with double star measurements during the same night: the pixel scale was measured as 23.27 ± 0.09 mas, and the rotation was found to be 0.71 ± 0.13°. The two pixel scale values agree very well within their errors – which is absolutely not self-evident: one should remember that the globular cluster calibration heavily relies on the correctness of the published HST astrometry and that

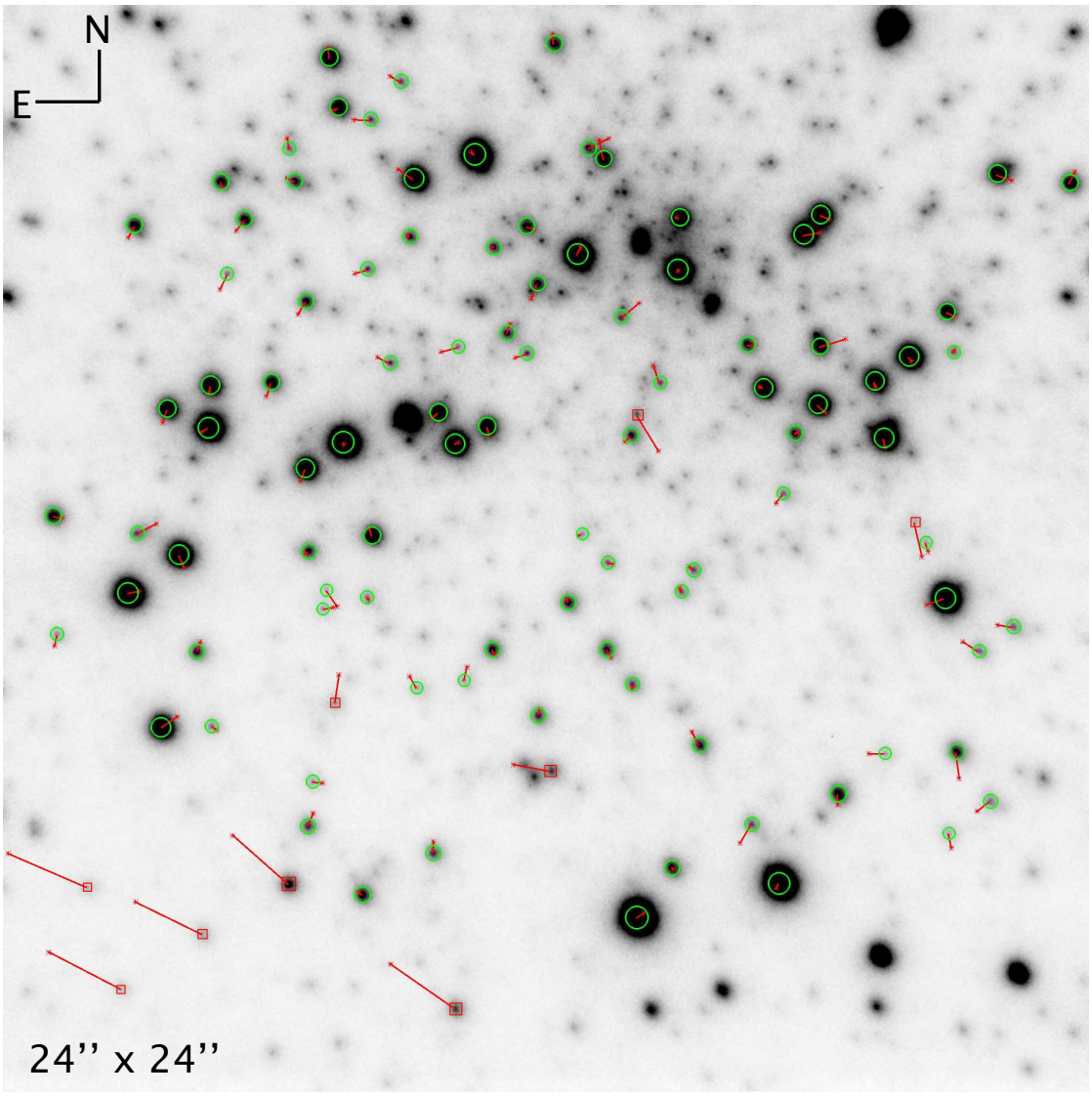

Figure 6.2. *M15 image used for astrometric reduction. Green circles indicate stars that were used in the final solution, rejected stars are marked with red boxes. The red lines show the amount (25× magnified) and direction of the residuals.*

any systematic errors in these data will affect the calibration results. It should be mentioned that Yanny et al. (1994) estimate the measurement errors of the relative astrometry within angles of few arcseconds as ≈20 mas, but ≈40 mas for larger separations.
The position angles derived from binaries and the M15 data differ significantly. However, the difference of 0.6° should still be acceptable for most applications, and probably negligible for astrometry of close binaries – here the angle uncertainty is usually dominated by the measurement errors of the component positions.

A full and thorough reduction of the M15 data would require to account for differential refraction. Depending on airmass, the pixel scale parallel to the parallactic angle is typically 1.0002−1.0006 times higher than in the perpendicular direction. This is of the same order of magnitude as the accuracy of the transform coefficients above. It would also be an advantage to select stars for

Table 6.2. *Astrometric reduction results of M15 calibration data*

Plate center:	$\alpha_0 = 21^h29^m58^s.441$ $\delta_0 = +12°09'53''.22$		
Transform coefficients:			
b =	23.3132 ± 0.0031 mas/px	h =	-0.5549 ± 0.0032 mas/px
c =	0.5151 ± 0.0043 mas/px	i =	23.3173 ± 0.0041 mas/px
d =	$8.1 \cdot 10^{-8} \pm 1.3 \cdot 10^{-8}$ mas/px^2	j =	$-3.4 \cdot 10^{-8} \pm 1.3 \cdot 10^{-8}$ mas/px^2
e =	$0.9 \cdot 10^{-9} \pm 1.7 \cdot 10^{-8}$ mas/px^2	k =	$-3.1 \cdot 10^{-8} \pm 1.7 \cdot 10^{-8}$ mas/px^2
RMS of fit residuals:	10.1 mas		
Linear pixel scale:	23.3214 ± 0.0072 mas/px		
Rotation angle:	$1.31 \pm 0.01°$		
Field of view:	$23''.88 \times 23''.88$		

the astrometric solution according to their colour – atmospheric dispersion will not only produce subtle differences in the PSF shape of stars with different colours, it will also introduce small shifts in elevation.
As long as the available astrometry is not affected by systematic errors, globular clusters are well-suited calibrators for AstraLux. The proper motions that can be expected within these objects are small compared to the orbital motion of most close binary stars, and the selection of several 10 reference stars in the cluster helps to average this effect out. Thus globular clusters can be seen as relatively static calibrators. Unfortunately, the number of these objects with published astrometry is by a factor of ≈10 smaller than the number of calibration candidate double stars, and there might be observing runs where it is difficult to find useable globular clusters at sufficient elevations throughout the night.

6.3.2 The Orion Trapezium

The Orion Trapezium cluster is frequently used for astrometric calibration purposes, especially in the near infrared. Stellar positions for the central 82″×82″ have been published by McCaughrean and Stauffer (1994) with relative astrometric accuracy in the order of 10 mas.
The Orion Trapezium was observed with AstraLux in November 2006 and January 2007. Figure 6.3 shows an image of the western part of the central cluster, overlayed with the star names as given in McCaughrean and Stauffer (1994). The first major difference compared to globular cluster data is the much smaller number of stars – the size of the AstraLux field of view does not allow to have more than three of the four brightest Trapezium stars in the same image, and many of the objects that have published astrometry are not bright enough at wavelengths below 1 µm to be suitable calibrators. The second striking difference is the image quality. While the M15 data shows nearly diffraction limited stars, all AstraLux observations of the Trapezium that could be obtained so far suffer from a large stellar FWHM of 200−300 mas. This limits the number of stars useable for centroid measurement and astrometric reduction to only seven in the shown image. Therefore, only simplified linear versions of the astrometric transform equations were solved, resulting in a pixel scale measurement of 23.54 ± 0.03 mas and a rotation angle of -0.6 ± 0.1° for the November 2006 data. Both values agree with the binary star calibration results from the same observing run within the errors.

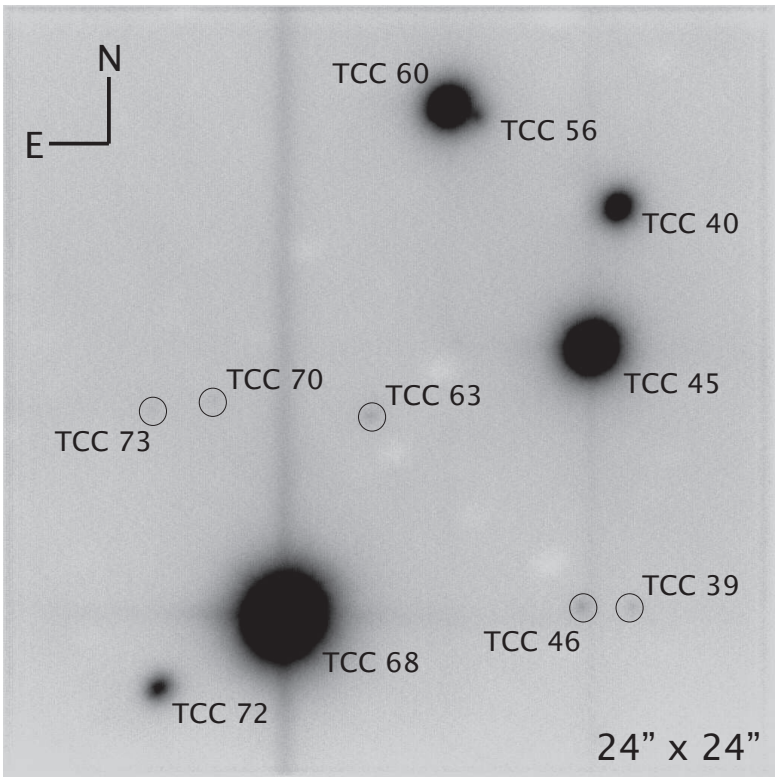

Figure 6.3. *AstraLux observation of the Orion Trapezium cluster in SDSS z' band. The effective integration time was 10 s. Stars are designated with the names given by McCaughrean and Stauffer (1994) and encircled where they are hardly visible in the printed version.*

The January 2007 observations of the Trapezium were independently reduced by Jérome Berthier, IMCCE Paris, to calibrate observations of the binary asteroid (22) *Kalliope* (see Chapter 7.4). As in the previous runs, a good agreement with the binary star calibration results was observed, confirming that the error estimates of the measurements are realistic.

6.4 Conclusions and Recommendations

Both presented methods have their advantages and drawbacks. Binary stars are well-distributed over the sky and ideal for monitoring pixel scale and rotation angle of the instrument. Unfortunately, the typical achievable calibration accuracy is in the order of 2% for the pixel scale and 0.5° for rotation angle. Only by observing a large number of different binary stars it is possible to reduce these errors. Besides this, they are certainly useful to get a quick estimate of the image parameters, since acquisition and reduction of a binary observation can be accomplished in just a few minutes.
If highest precision is necessary and non-linear image distortions have to be determined, globular cluster centres are the only available option. The data reduction requires considerably more effort, but results in superior calibration accuracy compared to the binary stars.
Observations of the Trapezium cluster can be used at least for measurements of the linear pixel scale and rotation angle, but the limited number of useable stars in the field of view will not allow to get the same precision as it is possible with globular cluster centres.

The experiences gained during the last three AstraLux observing runs allow to formulate a set of guidelines for efficient astrometric calibration of the instrument:

- At least one globular cluster centre with published HST photometry should be observed in each run, after any changes of the optical configuration, or if the camera was dis- and remounted.
- Additionally, the Orion Trapezium should be observed at least once (if it is visible).
- The observations of 2−3 calibration binaries should precede and follow globular cluster centre or Trapezium observations to calibrate the binary separations and position angles.
- Observations of these binaries should be used to monitor changes of pixel scale and image rotation during the run. It is sufficient to observe one binary each two hours. If these stars are not available during the whole night, they can be used to calibrate a set of secondary calibrators to fill in gaps of the hour angle coverage. However, using the same binary repeatedly will allow to assess the instrumental stability more reliably. These binaries do not have to be chosen from the set of calibration candidates as they will only serve for monitoring purposes. The actual calibration is done with the cluster astrometry.
- If no globular cluster or Trapezium data can be obtained, at least 10 different calibration binaries with angular separations $>1''$ should be used. They should be observed all in the same night, with as little time difference between the first and last observation as possible. Monitoring of the instrumental stability can then be performed as described above.

Chapter 7

AstraLux Observing Programmes

Scientific observing programmes with the AstraLux instrument started right during the first observing run in July 2006. The following sections give a short status report on these programmes and show some examples of observational data. While none of the target samples has been completed as of March 2007 and data reduction is still ongoing, the first refereed publication has already emerged from the preliminary results (see Chapter 8).

In January 2007, high speed photometric observations of the Crab pulsar were conducted. A GPS-based timing electronics, the μLux add-on, allowed time-stamping of individual exposures at frame rates of up to 1000 Hz with micro-second precision. This enabled the reconstruction of the pulsar's pulse profile. Whereas high speed photometry is not further covered in this thesis, a brief overview of the the μLux timing hardware can be found in Appendix D.

7.1 Young Stars in Nearby Moving Groups

In the past ten years, several nearby moving groups of young stars were identified. They are at distances of 20 to 80 pc and have ages in the range from 8 to 200 Myr (e.g. Zuckerman and Song, 2004; Fuhrmann, 2004). Members of these moving groups are the prime targets for direct imaging surveys for exoplanets, since due to the young age, any substellar objects should still be self-luminous, and hence relatively bright.
Because of their proximity, members of the moving groups exhibit relatively high proper motions of the order of 0.1 to 1″/yr. Hence new stellar and substellar companions can easily be identified by observations taken at 2 different epochs separated by only one year.

High angular resolution observations of ≈60 stars with AstraLux started in July 2006. A total of 7 new companions at angular separations between 0.″2 and 5″ were detected, with magnitude differences of 0–8 mag in the SDSS z' band. While all objects have been observed at least once since the start of the programme, most of them are still lacking second epoch measurements. With the exception of the close binary HD 160934 (see Chapter 8) and HD 96064, where archive pre-discovery images are available, it is too early to classify the discovered companions as physically bound or background stars. In the case of physical companions, dynamical mass estimates and colour index measurements will contribute to the calibration of evolutionary models for young stars in the low mass range.

The targets for this observing programme were selected from Zuckerman et al. (2001), Song et al. (2003), and López-Santiago et al. (2006). The only selection criterion was sufficient visibility with a required minimum elevation of 40°, corresponding to a declination of at least $\delta \approx -13°$. The sample included stars with doubtful classification as members of the Hercules-Lyrae association, as published by López-Santiago et al. (2006). All stars were observed at least in the SDSS z' band with typical total exposure times of 225 s, leading to an effective integration time of 11.25 s at a selection rate of 5%. Stars with new companion candidates were observed in the Johnson I filter as well to determine colour indices. However, as the effective wavelengths of the available SDSS z' and Johnson I filters differ by only 40 nm, and the filter bandpasses have a large overlap, these colour measurements have found to be not very useful. Selected targets will therefore be re-observed in the SDSS i' band when this filter becomes available for AstraLux in mid-2007.

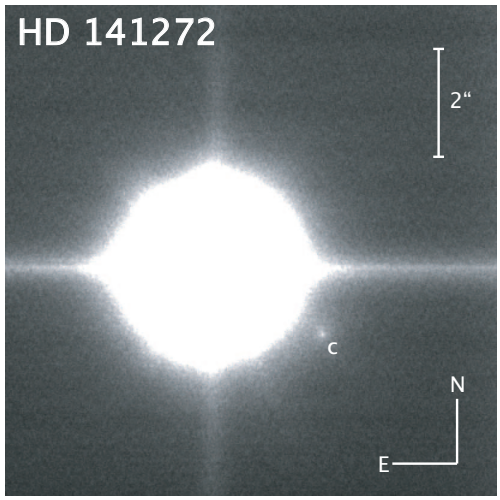

Figure 7.1. *HD 141272 and its possible companion. The I=7.6 mag bright host star is a doubtful member of the Hercules-Lyra association, with an assumed age of 200 Myr. At a distance of 21.4 pc, the magnitude difference of ≈8 mag in the SDSS* z' *band puts the companion in the very low mass regime. The companion has been observed several times in different filters to rule out artefacts like internal reflections or residuals of static aberrations.*

Figure 7.1 shows the the G8 V star HD 141272 with a possible very low mass companion at an angular separation of 2.″5. At a distance of ≈21 pc and a z'-band magnitude difference of nearly 8 mag between the I=7.6 bright host star and the secondary component, mass estimates are close to the brown dwarf regime. Second epoch observations in summer 2007 will allow to distinguish between a gravitationally bound system and a chance projection, as the proper motion of HD 141272 is ≈240 mas/yr.

A particularly interesting object is the wide double star GJ 9251. AstraLux observations revealed that this is in fact a triple system, with one of the known components being a close binary. Such a configuration allows relative astrometry of both close binary components with respect to the third component, yielding complete orbital information and reliable mass estimates. Figure 7.2 shows an image of GJ 9251, obtained during the January 2007 observing run.

Another example is HD 96064 at a distance of 25 pc (see Figure 7.3). The southwestern component of this wide system is a known close binary with nearly equally bright components. A fourth possible very low mass component with an absolute I-band magnitude of ≈14.5 mag is visible in the AstraLux images. This object could be located in VLT/NACO archive data (ESO programme 074.C-0084(B), PI R. Neuhäuser), obtained in June 2005. Astrometric measurements indicate that this component is not co-moving with the HD 96064 system and most likely a background star.

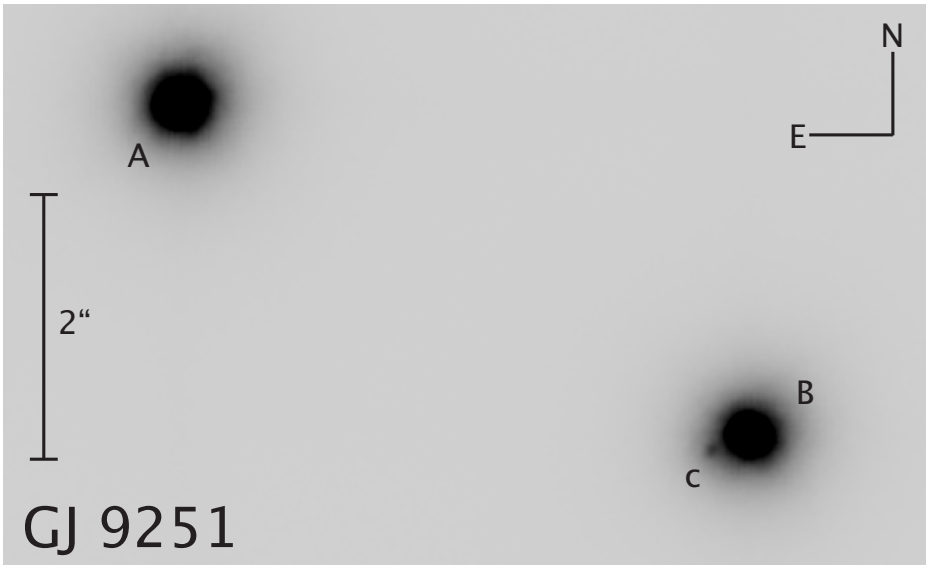

Figure 7.2. *The known double star GJ 9251 with its newly discovered close companion to the B component. The system is a member of the B4 subgroup of the AB Doradus moving group, with an assumed age in the range of 50−150 Myr.*

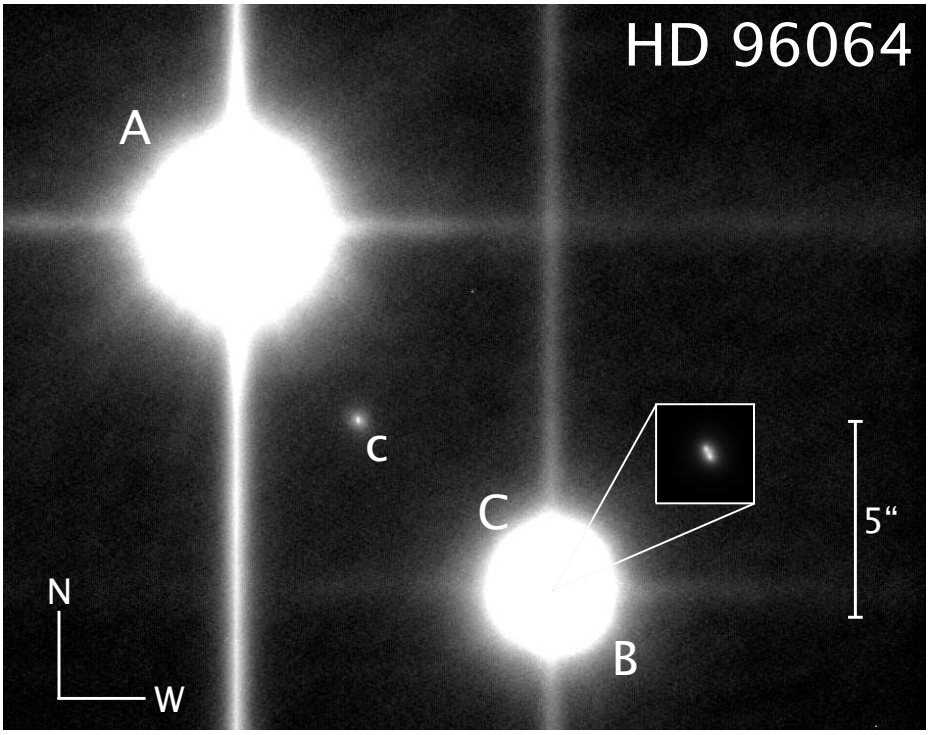

Figure 7.3. *The suggested quadruple system HD 96064, doubtful member of the Hercules-Lyra association. The companion candidate (halfway between A and BC) has an absolute I-band magnitude of ≈14.5 mag. The inset shows the close binary HD 96064 BC on a linear display scale, whereas the full image is scaled logarithmically.*

7.2 T Tauri binaries

From December 1990 until October 1992, a high angular resolution survey for binary and multiple systems was carried out in the nearby (140 pc) Taurus T association using lunar occultation and speckle techniques (Leinert and et al., 1993). In total 104 T Tauri systems were surveyed, and 39 double, 3 triple and 2 quadruple systems with separations between 0.″13 and 13″ were identified. Surveys by other groups (e.g. Mathieu, 1994) added another 9 multiple systems, resulting in a total of 53 binary and multiple systems. Another 27 multiple systems were identified among the sample of X-ray active T Tauri stars by Köhler and Leinert (1998). Relative astrometry of these systems can yield mass estimates of the components, and the combination with brightness ratio measurements in different passbands allows to further constrain the physical properties of these objects.

Taking projection effects into account, a typical T Tauri binary system with a separation of 0.″3 and a system mass of $1\,M_{\odot}$ has an orbital period of 270 yr. For an epoch difference of 15 yrs, a change in position angle (PA) by about 20 degrees is expected. Even closer or more massive systems should show a larger change in PA, while wider or less massive systems should exhibit a smaller change in PA. By comparison with proper motion data (e.g. Ducourant et al. (2005)), the re-observations of systems with only one epoch of data allow to test if these are physical binaries or chance projections.

AstraLux observations of all known T Tauri binaries from the Leinert sample were performed in the SDSS *z'* band in November 2006. For ≈35 systems the data allows relative astrometry with an accuracy better than 10 mas, and changes in PA of up to 40° since the early 1990s are visible in some of the closer systems.

Future observations in different passbands will result in *i'*–*z'* colour indices. This data, as well as the already derived *z'*-band brightness ratios, is complementary to the published measurements for most of the observed objects. While near infrared speckle and adaptive optics observations have been performed for all stars of this sample, resolved photometry at wavelengths <1 μm exists for only few targets.

Figure 7.4 shows the known quadruple system GG *Tau*, imaged in the SDSS *z'* filter. A possible fifth component of the system is visible west of GG *Tau* Bb. It was first observed by Silber et al. (2000) and later classified as a background star by Itoh et al. (2002), based on astrometric measurements.

AstraLux imaging of the double system GI/GK *Tau* shows the presence of a fainter companion to GK *Tau*, apparently not reported so far (see Figure 7.5). The companion is located 2.″5 northeast of GK *Tau*, and is ≈4 mag fainter in the SDSS *z'* band. For this object, acquisition frames obtained with the NICMOS and ACS instruments of the Hubble space telescope are available. While the angular separation between GK *Tau* and the companion did not significantly change during the last eight years, the position angle has decreased by more than 5 degrees. This is inconsistent with an assumed mass of $\approx 1\,M_{\odot}$ for GK *Tau*. Further astrometry and photometry are necessary to distinguish between a chance projection and a bound system.

This finding indicates that it is still possible to detect new companions to rather well observed T Tauri stars. The current AstraLux sample might be expanded by objects that are assumed to be single stars, eventually leading to the discovery of new binary or multiple systems.

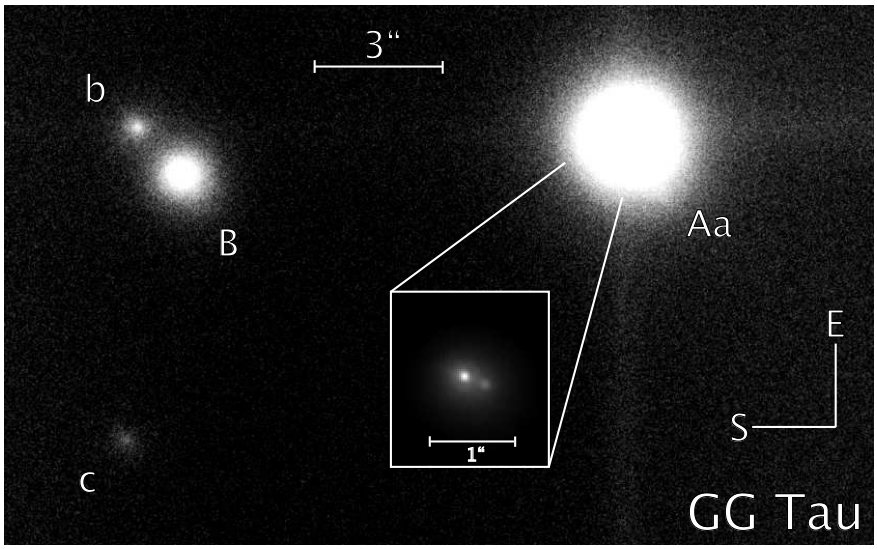

Figure 7.4. *The multiple system GG* Tau, *observed in SDSS z'. The fifth component* c *in the southwestern corner of the image is a background star.*

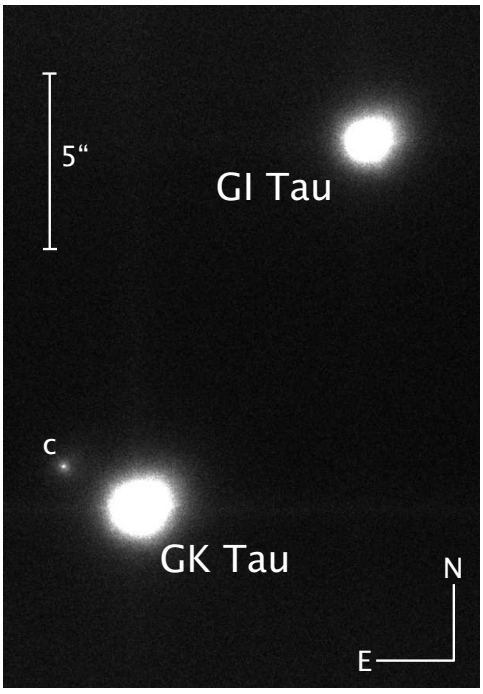

Figure 7.5. *The known binary system GI/GK* Tau *and a possible new companion to GK* Tau. *The angular separation between GK* Tau *and GK* Tau*/c is 2.″5 at an SDSS* z' *band magnitude difference of 4 mag.*

7.3 Nearby M dwarfs

While stellar multiplicity statistics are well established nowadays for the G and K star population in the solar neighbourhood (e.g. Duquennoy and Mayor, 1991; Halbwachs et al., 2003), this is not yet the case for later spectral types. Besides pure statistics, astrometric observations of low-mass binaries allow dynamical mass estimates, vital for the calibration of stellar models. While e.g. the models of Baraffe et al. (1998) are believed to predict accurate absolute near-infrared magnitudes for low-mass stars, they become increasingly unreliable at visible wavelengths. Thus

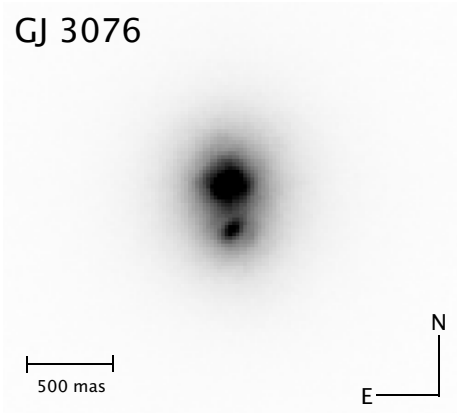

Figure 7.6. *The known M dwarf binary GJ 3076. The PSF of the secondary component is slightly elongated due to atmospheric dispersion.*

Lucky Imaging observations of low-mass binaries can provide valuable input for the refinement of such models.
Law et al. (2006) recently began to successfully survey nearby M dwarfs in the SDSS *i'* and *z'* band with LuckyCam at the Nordic Optical Telescope, and MPIA started a similar binary search programme with AstraLux in November 2006.

The targets for this mini-survey were selected from Riaz et al. (2006). They published a list of 1080 spectroscopically studied nearby stars with spectral types between K5 and M6, selected by correlating the Two Micron All Sky Survey and ROSAT catalogues. The AstraLux sub-sample is volume-complete out to a distance of 11 pc, and includes M3−5 dwarfs with V-magnitudes as faint as 14.5 mag.

Figure 7.6 shows an AstraLux image of the M5 dwarf GJ 3076 at a distance of ≈8 pc. Its companion to the south was first detected by Beuzit et al. (2004) with *K*-band observations at the Canada France Hawaii Telescope (CFHT), using the PUEO adaptive optics system (Arsenault et al., 1994). Since its discovery in August 2000, the angular separation between the two components has decreased from 409 mas to 306±10 mas in the AstraLux image, and the position angle has changed from 147° to 187±2°. This is a good example for a system where follow-up astrometry during the next years will allow to derive accurate mass estimates.

Figure 7.7 shows the triple system 2MASS 03323578+2843554. This object, that has apparently not been observed with high angular resolution techniques before, is listed as a single M5 dwarf at a photometrically determined distance of 11 pc in the catalogue of Riaz et al. (2006). Under the assumption that the spectral types of the three components are not too different, the real distance has to be larger to match with the observed apparent magnitude of V=13.8. This object is certainly one of the highlights of the AstraLux results, needing urgent follow-up observations at different wavelengths to allow spectral typing of the individual components.

The probability that this triple configuration may be just a chance projection is very low. The object can be located in the Digital Sky Survey (DSS) as well as in recent (year 2003) archive frames of the Near Earth Asteroid Tracking programme (NEAT, Pravdo et al. (1999)), allowing measurements of its proper motion. At a rate of ≈1″over the last 50 years, one would expect a binary appearance or at least an elongated PSF in the DSS data, if the three components of the system were not co-moving. As the system's PSF appears pointlike in the DSS images, this is most likely a physically bound system.

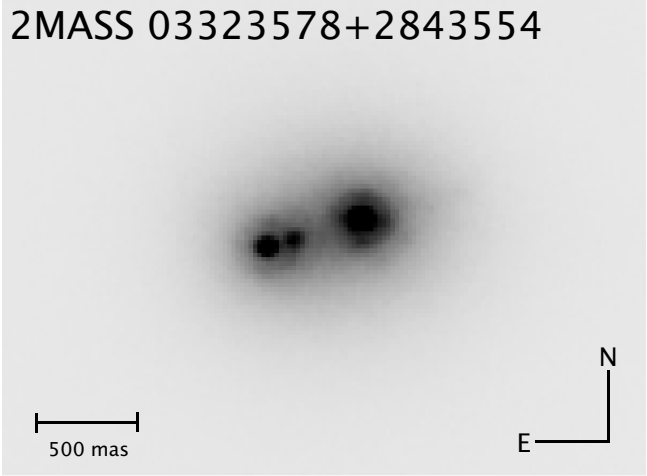

Figure 7.7. *The newly discovered triple M dwarf system 2MASS 03323578+2843554. The angular separation between the two outermost components is 540 mas, and only 150 mas between the two eastern components.*

Besides follow-up observations, the current M dwarf sample will be extended to fainter objects, increasing the volume-completeness to a radius of 20 pc. Future observations will profit from the availability of an SDSS *i'* filter.

7.4 (22) Kalliope and Linus

While asteroids are suspected to have satellites since more than 100 years, real evidence was not found before 1993, when the *Galileo* spacecraft transmitted the first images of an asteroid's moon back to earth. The discovery of the 1.4 km sized moonlet *Dactyl* around the asteroid (243) *Ida* triggered the start of various observing campaigns, focused on the discovery of asteroid satellites. A thorough review of the history of binary asteroid research can be found in Merline et al. (2002).

The most successful method up to now is based on lightcurve analysis. The subtle signatures of mutual eclipse events in binary asteroid systems can be observed even with small telescopes, and collaborations between professional and amateur astronomers are particularly successful (e.g. Behrend et al., 2006). Radar imaging of near-earth asteroids, originally aimed at size measurements, proved that binary asteroids are not confined to the main belt between Mars and Jupiter (e.g. Benner et al., 2006; Ostro et al., 2006). The omnipresence of asteroids with moons in our solar system has been further confirmed by direct imaging of binary or even triple systems among the Kuiper belt asteroid population (see Noll et al. (2006) for a recent example in this field). Pluto, since the IAU general assembly 2006 now officially a dwarf planet, is probably the largest transneptunian body and known to have at least three moons (Weaver et al., 2006).

Direct imaging of binary asteroids from the ground was not possible until the availability of adaptive optics at large telescopes. One example for a ground-based observation is the discovery of the moon *Linus* to the main-belt asteroid (22) *Kalliope* by Margot and Brown (2001) and Merline et al. (2001). This system has been extensively studied since then, leading to a full orbit determination by Marchis et al. (2003).

Among the known binary asteroids in the main belt, (22) *Kalliope* is the best suited system for observations with AstraLux. With a semimajor axis of ≈1000 km, the angular separation between the two components can be as large as 850 mas, and *Kalliope* itself is bright enough to be used as Lucky Imaging reference. The diameters of *Kalliope* and its moon are ≈180 km and 40 km, respectively, resulting in a moderate magnitude difference of ≈3.3 mag.

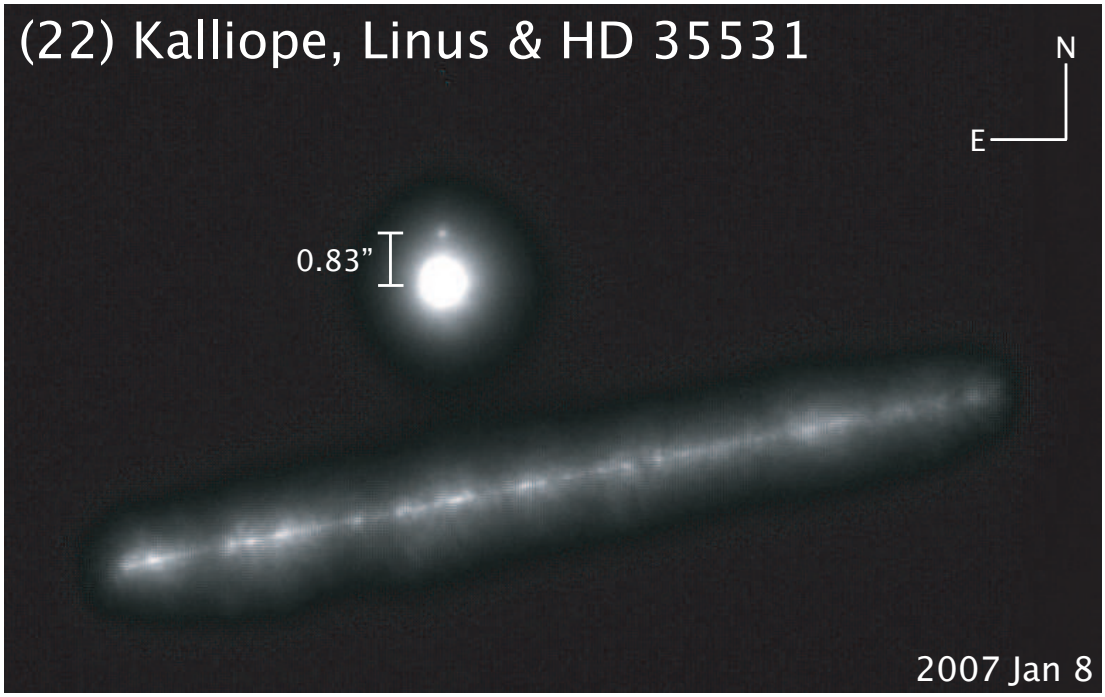

Figure 7.8. *The asteroid (22)* Kalliope*, its moon* Linus *to the north, and the background star HD 35531. This image was generated from the best 2.5% of 65000 frames with 30 ms single frame exposure time. During the ≈30 minutes of the observation,* Kalliope *moved by about 19″ with respect to the star, which appears as a trail in this image.*

First resolved observations with AstraLux were obtained in November 2006 and astrometrically reduced. The comparison with theoretical predictions confirmed that the measured positions were within the ≈30 mas uncertainties of the orbital model (P. Descamps, private communication). On January 8, 2007, the *Kalliope* / *Linus* system occulted the star HD 35531. While the occultation event would have been visible only from locations in northern Asia, the angular separation between *Kalliope* and the star, viewed from southern Spain, was still small enough to fit within AstraLux's field of view.
Figure 7.8 shows the result of this observation. *Kalliope* and *Linus* are clearly resolved and appear pointlike, whereas HD 35531 has left a trail in the final image due to *Kalliope's* proper motion of ≈0.″63/min relative to the star. The non-uniform, somewhat "clumpy" appearance of the star's trail is the result of the Lucky Imaging selection process and demonstrates that the moments of least atmospheric turbulence are not evenly distributed in time. The brightness distribution along the star's trail suggests that seeing conditions were on average better towards the end of the observation, corresponding to the left side of the trail.

It is worth noting that *Kalliope* is not a perfect pointsource, hence not an optimal Lucky Imaging reference object. At a distance of 1.6 AU at the time of the observation, the angular size of *Kalliope* was ≈150 mas, and the asteroid's disk covered an area of almost eight pixels on the

detector. When such a slightly extended object is used as the Lucky Imaging reference, the position of the brightest pixel in a short exposure image does not necessarily correspond to the centre of the object. As a consequence, the final image is convolved with a function whose width and shape are determined by size and geometry of the reference source. This reduces the Strehl ratio and angular resolution of the Lucky Imaging result.

Observations of binary asteroids – direct or photometric – are the primary source for density estimates. Alternative methods like in-situ exploration, analysis of orbiting spacecraft trajectories, or modelling of subtle changes of the orbital elements after close encounters with other asteroids are applicable to only few objects.
The pure existence of binary asteroids is a tough challenge for any evolutionary model of the solar system. More observational input is needed to sort out the question whether some binaries might have formed as primordial pairs, or if collisional mechanisms are the only way to produce them. The question might be more complicated than that, as binary asteroids in different populations, starting in the near-earth region and reaching out to the Kuiper belt, may require different models to explain their existence.

Though AstraLux might be able to observe only the brightest widely separated systems, it can contribute to the solution of this puzzle by monitoring known binary asteroids, allowing the refinement of orbital parameters.

Chapter 8

Direct Imaging of the Young Spectroscopic Binary HD 160934

HD 160934 is a well-suited example for the successful combination of AstraLux observations with data from other sources. The following sections largely correspond to Hormuth et al. (2007), but some aspects, e.g. the unresolved photometric measurements, radial velocity analysis, and the modelling of the physical parameters of HD 160934, are described in more detail.

8.1 Introduction

The young active star HD 160934 was observed as part of the sample of young stars in nearby moving groups. The discovery of a close companion, the availability of pre-discovery HST archive image data and ground-based radial velocity measurements allowed conclusions about the orbital parameters without a second epoch of AstraLux observations. Unresolved photometry from the 2MASS catalogue and own *UBVRIz'* measurements with MPIA's 70 cm telescope were used to constrain the physical properties of the system, i.e. to estimate masses, age, and spectral types of the components.

HD 160934 (= HIP 86346) is a young late-type star with a spectral type of K7 to M0 (Reid et al., 1995; Zuckerman and Song, 2004) at a distance of ≈24.5 pc (Perryman et al., 1997). It is chromospherically active (Mulliss and Bopp, 1994) with prominent EUV (e.g. Pounds et al., 1993) as well as X-ray emission with an X-ray luminosity of $L_X = 3.4 \times 10^{22}$ W (Hünsch et al., 1999). The activity can also be traced in the Hα line, which is seen in emission with an equivalent width between -0.09 and -0.13 nm (Mulliss and Bopp, 1994; Gizis et al., 2002; Zuckerman and Song, 2004). The detection of the Li 6708Å line with an equivalent width of 40 mÅ (Zuckerman and Song, 2004) gives further evidence that HD 160934 is a relatively young star. The youth indicators combined with the 3d space motion led Zuckerman and Song (2004), Zuckerman et al. (2004), and López-Santiago et al. (2006) to suggest that HD 160934 might be a member of the ≈50 Myr old AB Doradus moving group.

Because of its proximity to the Sun and its young age, HD 160934 is a good candidate for the direct detection of substellar, or even planetary mass companions. McCarthy and Zuckerman (2004) report that no brown dwarf companion could be found at projected separations larger than

75 A.U. as a result of a near infrared coronagraphic study carried out at the Keck observatory. Using HST/NICMOS in coronagraphic mode, Lowrance et al. (2005) report the detection of a possible wide companion to HD 160934 at a projected separation of ≈8.″7 (corresponding to ≈210 A.U.) and at a position angle of ≈235°. The brightness difference between the companion candidate, designated HD 160934 B, and HD 160934 A is ΔH = 9.2 mag. Under the assumption that HD 160934 B constitutes a physical companion to HD 160934, Lowrance et al. (2005) derive a mass estimate of ≈0.15 $M_{\odot}$ for this companion.

By combining 38 radial velocity measurements, Gálvez et al. (2006) identified HD 160934 as a spectroscopic SB1 binary and suggested a period of P = 6246.2318 days, a high eccentricity of e = 0.8028, and a spectral type of M2-M3V for the spectroscopic companion, so that HD 160934 may be at least a triple system.

HD 160934 was observed with AstraLux at the Calar Alto 2.2 m telescope in July 2006, leading to the discovery of a close companion at a separation of ≈220 mas. Unresolved *UBVRIz′* photometry was obtained in September 2006 at MPIA's 70 cm telescope.

8.2 Observations and Data Reduction

8.2.1 Direct Imaging with AstraLux at the Calar Alto 2.2 m Telescope

All AstraLux observations were carried out in the standard instrument configuration, i.e. with the Barlow lens in the optical path and a resulting pixel scale of 46.6 mas. The data were uniformly processed with the November 2006 version of the AstraLux pipeline software, using polychromatic MTF-filtering at the image selection stage and a twofold oversampling during the Drizzle process.

Pixel scale and camera rotation angle were determined with observations of seven different known binaries. While the RMS of the pixel scale was on the order of 1% using all stars, the variations for measurements of the same star were below 0.1% in pixel scale and 0.°5 in rotation angle during one night. The 1% scatter between individual stars reflects the uncertainties of the ephemerides for these "calibration binaries" and limits the accuracy of the measurements to this value.

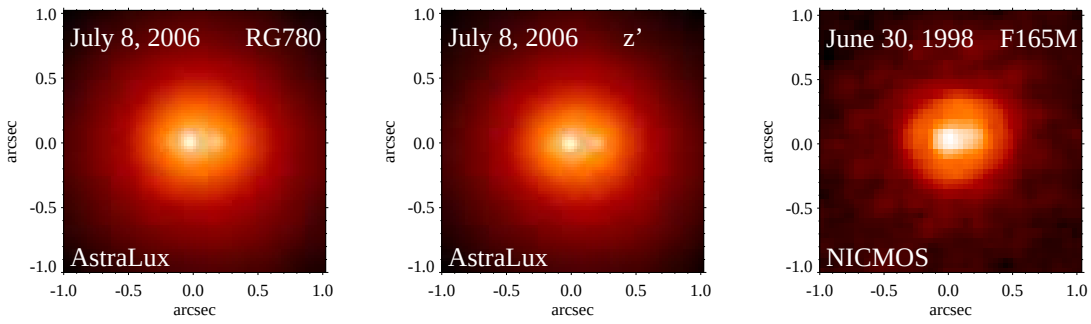

Figure 8.1. *AstraLux I, z' and NICMOS F165M images of the binary displayed on a logarithmic intensity scale. The field of view is 2″×2″, North is up and East is to the left. The binary components are clearly detectable in all three bands.*

8.2.2 HST/NICMOS

Observations of HD 160934 with HST/NICMOS were obtained on June 30, 1998 (GO 7226, PI E. Becklin). Since the main aim of the programme was to search for faint, substellar companions, the coronagraphic mask in NIC2 was used. Because of this, the close companion to HD 160934 was not detected in the science data (see Lowrance et al., 2005). It is, however, detectable in the two acquisition frames.

The acquisition frames were obtained with the $F165M$ filter and an integration time of 0.626 s. For the analysis a pixel scale of 75.10 mas/pixel was assumed. The FWHM of the PSF was around 2 pixel, corresponding to 150 mas, which is close to the diffraction limit of HST at the observing wavelength. For the second acquisition frame, taken at the beginning of a subsequent orbit, the HST guide star acquisition partially failed, resulting in a slightly trailed PSF. Figure 8.1 shows a comparison of the AstraLux I and z', and the NICMOS $F165M$ images of the HD 160934 binary, while Table 8.1 gives the dates and details of the direct imaging observations.

The analysis of the binary properties is based on the pipeline reduced frames and was carried out by Wolfgang Brandner and Markus Janson. Tiny Tim Version 6.3 (Krist and Hook, 2004) was used to compute the theoretical PSF. In order to estimate the effect of HST "breathing" (i.e. focus changes induced by thermal expansion or shrinking of the optical train of HST), also slightly defocused PSFs were calculated and used for the binary fitting.

Table 8.1. *Direct imaging observing log for HD 160934.*

Date	Telesc./Inst.	Filter	t_{int} Seeing
30 June 1998	HST/NIC2	$F165M$	2×0.626s
8 July 2006	CA 2.2m/AstraLux	I	4.5s[a]
8 July 2006	CA 2.2m/AstraLux	z'	4.5s[a]

[a] Best 2% of 15000 frames with an individual $t_{int} = 0.015$s

8.2.3 Fitting of Binary Parameters

For both data sets (AstraLux and NICMOS) a binary model was fitted to the data in order to derive binary separation, position angle and brightness ratio (see Bouy et al., 2003). For the NICMOS data, only the first acquisition frame was used. The slightly trailed binary PSFs due to the partial guide star acquisition failure for the second HST orbit resulted in a bias in the determination of the brightness ratio using a non-trailed PSF.

While for the NICMOS images a theoretical model can serve as reference PSF for binary fitting, this is not feasible for the Lucky Imaging data. Since the PSF shape depends on actual seeing conditions, it is not possible to accurately predict the theoretical PSF of a single star in the final results. Neither is there an isolated third star available in the images, which could have served as an independent reference. Instead a set of eight different reference PSFs was used, generated from observations of single stars throughout the same night. The fit results for each PSF were finally weighted by the residuals after subtraction of the corresponding binary model, leading to the values given in Table 8.2.

Table 8.2. *Binary properties*

Date (Filter)	separation [″]	PA [°]	brightn. ratio
June, 30 1998 (F165M)	0.155 ± 0.001	275.5 ± 0.2	0.485 ± 0.006
July, 8 2006 (SDSS z')	0.215 ± 0.002	270.9 ± 0.3	0.329 ± 0.051

8.2.4 Unresolved Photometry

The available photometry of the unresolved system covers the wavelength range from *U*- to *K*-band. Weis (1991, 1993) has published Johnson-Kron *UBVRI* photometry. *JHK* magnitudes are contained in the 2MASS point source catalogue (Skrutskie et al., 2006).

During the course of the Hipparcos mission, 96 photometric measurements of HD 160934 were acquired. The lightcurve shows irregular brightness variations with semi-amplitudes of 0.05-0.1 mag on timescales of the order of a few days. Ground-based observations by Pandey et al. (2002) point to a period of 43.2 days, whereas Henry et al. (1995) published a much shorter value of 1.84 days with some uncertainties regarding the presence of a longer period.

In addition to the published data, *UBV(RI)*$_C$ and z' all-sky photometry was obtained with MPIA's Königstuhl mountain 70 cm telescope on September 5 and September 13, 2006. The *UBV(RI)*$_C$ calibration was based on 17 standard stars from Landolt (1983, 1992), distributed over a wide range of airmasses. For the SDSS z' measurements, a set of three primary calibrators from the SDSS Standard Star Network (Tucker et al., 2001) was used. Each reference field and HD 160934 were observed five times in each filter during the night, with three exposures per filter and pointing to enhance the dynamic range. The data allowed to reliably determine the measurement errors, to measure the first and second order extinction in each filter, and to establish the previously unknown colour transform coefficients of the filter set.
Table 8.3 summarises all available unresolved photometric measurements.

8.3 Physical Properties of the HD 160934 Binary

8.3.1 Common Proper Motion

The proper motion of the unresolved HD 160934 system amounts to $\mu_{RA} = -31.25 \pm 14.43$ mas/yr and $\mu_{DEC} = 59.44 \pm 11.21$ mas/yr. In the 8 years, which passed between the NICMOS and AstraLux observations, HD 160934 moved 250 ± 115 mas to the West, and 475 ± 90 mas to the North. In the same period, the separation between HD 160934 A and c increased by only $\approx$ 60 mas, and the position angle decreased by $\approx 5°$(see Table 8.2). This gives strong evidence that both sources form a physical binary.

Table 8.3. *Unresolved photometry of HD 160934*

Source	Filter/Colour	mag		1σ
Königstuhl 70 cm	V	10.192	±	0.014
	$U-B$	0.947	±	0.008
	$B-V$	1.215	±	0.005
	$V-R_C$	0.789	±	0.004
	R_C-I_C	0.766	±	0.007
	z'	8.820	±	0.009
Weis (1991, 1993)	V	10.28	±	0.020
	$U-B$	0.95	±	0.015
	$B-V$	1.23	±	0.015
	$V-R$	0.78[a]	±	0.015
	$R-I$	0.63[a]	±	0.015
2MASS	J	7.618	±	0.024
	H	6.998	±	0.016
	K	6.812	±	0.020
Hipparcos	V	10.29		
	$B-V$	1.591	±	0.400
	$V-I_C$	2.58	±	0.91

[a] The R and I-band photometry of Weis is given in the Kron system. Using the cubic transformations given by Bessell and Weis (1987), the corresponding colours in the Cousins system are $V-R_C$=0.78 and R_C-I_C=0.79.

8.3.2 Photometric Estimates of Masses and Spectral Types

Estimates of the spectral types and components' masses were derived using the $V-I_C$ colour index, the V magnitude of the unresolved system, and the SDSS z' and $F165M$ magnitude differences of the components. These values were compared to the model predictions of Baraffe et al. (1998) (abbreviated BCAH98 in the following text) for solar metallicity low-mass stars, searching for a mass combination best fitting the available photometry. Coevality of the two components was assumed throughout the analysis.

Since the published BCAH98 models do not directly predict z'-band magnitudes, the empirical colour transforms of Jordi et al. (2006) were applied to transform from $(RI)_C$ to SDSS z'. Though this seems like a rather crude method and calculating appropriate z'-band magnitudes from model spectra would be a more precise approach, this method should be sufficient. Since not the z'-magnitudes are fitted directly, but rather the z'-magnitude difference, the chosen approach is valid if the components' spectral types do not differ too strongly.

A similar approach was taken in the case of the $F165M$ magnitude difference. Since the centres of the $F165M$ and H passbands are nearly identical, and differ only in width, the $F165M$ magnitude difference was directly compared to the model predictions for H-band brightness differences.

Table 8.4. *HD160934Ac mass estimates for an assumed age of 79 Myr*

Component	mass [$M_\odot$]	T_{eff} [K]	log $L/L_\odot$	g
A	0.69	4290	-0.83	4.60
c	0.57	3780	-1.23	4.68

The BCAH98 model magnitudes were interpolated on a finer mass grid, and for each possible mass combination in the range of 0.2−1.0 $M_\odot$ the combined V magnitude, $V - I_C$ colour index, and the SDSS z' and H-band brightness ratios were computed and compared to the measurements (in the case of the V-band magnitude, the comparison was made to absolute V magnitude, based on the Hipparcos parallax). The residuals were weighted by the measurement errors, and the best fitting mass combination found by iteratively determining the global minimum of the residuals. Fitting was performed with models for different ages in the range of 30 to 158 Myr. Minimum residuals were obtained with the BCAH98 model for an age of 79 Myr, and the resulting mass estimates are given in Table 8.4, together with the effective temperatures, luminosities, and surface gravity from BCAH98. Figure 8.2 shows three example log(χ^2) plots for model ages of 50, 79, and 100 Myr. For all three models there is a distinct global minimum of the χ^2, but the resulting component masses obviously depend on the model age.

Using the unresolved V-magnitude, one derives a distance module of M–m=2.81 mag, corresponding to a distance of d=36.5 pc and a parallax of π = 27.4 mas. Compared with the directly measured Hipparcos parallax of 40.75±12.06 mas, this deviates by 1.1σ. Of course, since the Hipparcos parallax and its error were used in the fitting process, this photometric distance estimate is not an independent measurement and somewhat circular. However, the derived values still constitute a set of physical parameters compatible to observations within the measurement errors.

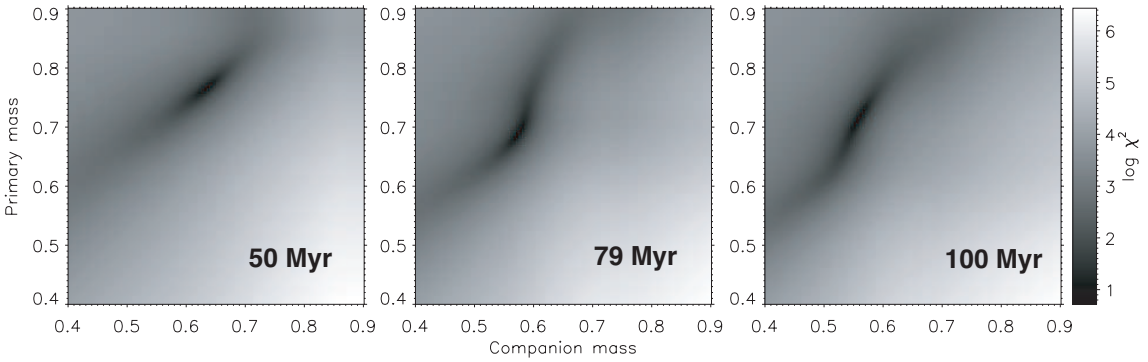

Figure 8.2. *2d plots of the χ^2 fit residuals for component masses between 0.4 and 0.9 $M_\odot$ and three different BCAH98 model ages. Please note the logarithmic scaling of the χ^2.*

It should be noted that using the BCAH98 models for 50 Myr results in nearly equally small residuals as obtained with the 79 Myr models. For the younger model, the components' masses would be 0.64 and 0.77 $M_\odot$, respectively. The error of the mass estimates should therefore be assumed to be of the order of 0.1 $M_\odot$. It should also be noted that the V magnitudes of the BCAH98 models are known to be be rather inaccurate for very-low-mass stars (e.g. Allard et al., 1997), and that this may to some extent still be the case in the 0.7 $M_\odot$ regime.

As a final crosscheck, the combined *J*, *H* and *K* magnitudes of the unresolved binary as predicted by the BCAH98 models were compared to the 2MASS measurements given in Table 8.3. The model magnitudes (using d=36.5pc) are *J*=7.59, *H*=6.99, and *K*=6.86 mag, which corresponds to a maximum deviation of 2.4σ or 0.048 mag in *K*-band.

The derived values allow a tentative spectral typing of the two components, suggesting a combination of a K5 and an M0 star. This is in good agreement with the published spectral types of the unresolved binary (Reid et al., 1995; Zuckerman and Song, 2004).

8.3.3 Orbital Parameters and Comparison to RV Data

Radial velocity (RV) measurements of HD 160934 exist for the years 1995–2004. Gálvez et al. (2006) published an RV curve based on 38 measurements, eventually leading to the classification of HD 160934 as an SB1 spectroscopic binary with an RV amplitude of K≈7.2 km s^{-1}. They deduced a period of P=6246.2318 days and an eccentricity of e=0.8028, and derived a spectral type of M2–M3V for the companion based on their mass estimates.
However, the observations cover less than one orbit and hence only one minimum of the radial velocity. In addition, the phase coverage is relatively sparse with only a single measurement for phases 0.2–0.9, so the given orbital parameters should be considered as preliminary. While the available data allows to conclude that the orbit is relatively eccentric, it is this high eccentricity that makes period estimates without better coverage of the full RV curve unreliable.

Between the HST and AstraLux observations, the change in projected separation and position angle was 65 mas and 4.6°, respectively. Two scenarios are possible: either the orbital period is considerably larger than the 8 years time difference between the observations, or it is an integer fraction of it (including ≈ 8 years as one possibility). The spectroscopically determined period of P∼17.1 yr is – at first sight – incompatible with this, since it would predict a difference in position angle of nearly 180° for the direct imaging observations. A possible solution to this contradiction could be that HD 160934 is in fact a quadruple system (including the possible widely separated B component), and that the directly imaged companion is not identical with the spectroscopic detection.

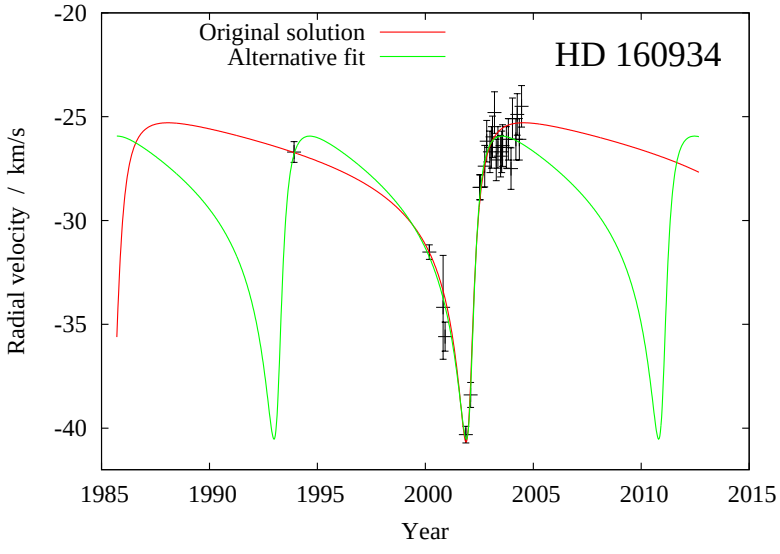

Figure 8.3. *Radial velocity measurements of HD 160934. The RV values were extracted from Gálvez et al. (2006), and the long-period fit uses the published period. The dashed line is the proposed alternative short-period solution.*

The radial velocity curve in Gálvez et al. (2006) is plotted against the orbital phase, but it is possible to reverse-engineer the plot to convert from phase to absolute time. This data can certainly not be used for a thorough quantitative analysis, since it is not based on numbers, but just on plotted points in a printed diagram. Nevertheless, it allows to test alternative orbital periods. Figure 8.3 shows the published measurements together with RV curves for two possible orbital solutions. The long-period fit (in red) is based on the period and eccentricity given by Gálvez et al. (2006), while the short-periodic solution corresponds to an alternative orbit with P=3255 days and e=0.66. If this was the true orbit, the spectroscopic and direct detection would probably refer to the same companion.

If one assumes the shorter period of P=3255 days, and uses the mass estimates of M_1=0.69 and M_2=0.57 $M_\odot$ above, then the corresponding semimajor axis would be a=4.5 A.U. or 0.″12 at a distance of 36.5pc. With an eccentricity of e=0.66, this results in a maximum possible separation between the two components of r=7.5 A.U. or 0.″21, which is close to the July 2006 AstraLux measurement. Further RV measurements and resolved imaging in the next 2-3 years will allow to pin down the true orbit and to sort out the period ambiguity.

8.4 Conclusions

By combining pre-discovery HST archive data, AstraLux high angular resolution astrometry and unresolved photometry, it was possible to derive mass and spectral type estimates for the HD 160934 system. These estimates are compatible with unresolved 2MASS photometry, Hipparcos distance measurements, and existing age estimates for HD 160934 and the AB Doradus young moving group. It is proposed that the directly imaged companion is identical with the companion discovered by radial velocity measurements, and that the orbital period is ≈8.5 years, about half the value of Gálvez et al. (2006).
Further high angular resolution observations and radial velocity measurements in the next 2-3 years will allow to confirm or negate this suggestion. In the positive case, the combination of RV measurements and astrometry will allow to compute a full set of orbital parameters, and to derive precise component masses. The knowledge of the orbit will enable the reanalysis of the Hipparcos measurements, resulting in much smaller errors for the parallax, distance, and distance module. In return, this will make the HD 160934 system a valuable calibrator for pre-main-sequence stellar models.

Chapter 9

Conclusions & Outlook

Within less than one year it was possible to design, build, and characterise a Lucky Imaging instrument for the Calar Alto 2.2 m telescope. Beyond evaluation of the observing technique and data reduction strategies, scientific observations led to the first refereed publication only five months after first light.

Summary of the Instrument's Key Features

AstraLux provides nearly diffraction limited imaging with Strehl ratios of up to 25% at a 2-m class telescope in the *I*-band. At the moment, no other instrument at Calar Alto is capable of such image quality in this wavelength range.

The reference object necessary for image selection can be as faint as I=15.5 mag. This is $\approx$1.5 mag fainter than the typical limit for adaptive optics with natural guide stars, and $\approx$4 mag fainter than the requirements for speckle imaging – the only other ground-based technique that is available for diffraction limited imaging in the visible wavelength range.
At angular separations larger than 2″, fainter companions to the reference star can be detected at magnitude differences of up to 8 mag.

While the reference star may not only be fainter than for other high resolution imaging techniques, Lucky Imaging allows at the same time large angular separations between science target and reference. The isoplanatic angle has found to be $\approx$40 arcsec in *I*-band. Only adaptive optics systems with laser guide stars are able to outperform Lucky Imaging in terms of sky coverage.

It is true that the image selection process of the Lucky Imaging method "throws away" photons. But: the Strehl ratio in an image that is based on a 5% selection is typically ten times higher than in a seeing limited image that contains all accumulated photons. This corresponds to an improvement of the signal-to-noise ratio of point sources by a factor of 10−20, almost compensating the loss in effective integration time. This is not true for extended sources, where an increase of the Strehl ratio and image resolution will not improve the signal-to-noise ratio.
Of course, observing with an adaptive optics system allows to use 100% of the signal, hence the same results can be achieved in less time. But still, this is only possible in the near infrared and with brighter reference objects.

Apart from performance issues, Lucky Imaging requires much less instrumental effort and development time than adaptive optics, at a fraction of the costs. An instrument like AstraLux can be deployed at virtually any telescope in the 1–3 m class on timescales of months. The proposal pressure on such medium sized telescopes has steadily decreased over the past years. The installation of simple and cost effective, yet novel and innovative instruments like AstraLux could be an appealing alternative to decommissioning.

With the recent partial failure of the Hubble Space Telescope's Advanced Camera for Surveys, high resolution imaging at visible wavelengths from space has suffered a major setback. In the long term no replacement can be expected, since HST's successor, the James Webb Space Telescope (JWST), will be equipped with instruments insensitive to wavelengths $<1\,\mu$m. Besides this, one minute of observing time with JWST will be at least as expensive as an entire night at the Calar Alto 2.2 m telescope, and the pressure on JWST observing time will certainly be several times higher.

The straightforward observing technique leads to very small overheads at the telescope. Since the observer can see the reference object on a live display, target acquisition can be accomplished in typically 1–2 minutes. This allows to complete e.g. a binarity survey among 60 stars in only one night.

The simple design of AstraLux provides a high degree of stability. At the moment, the astrometric accuracy is limited by the available calibrators and not by the instrument itself.
AstraLux offers astrometry with a precision better than 5 mas over the full field of view. It is ideally suited for the astrometric follow-up of binary stars, providing valuable information for orbit calculation and refinement.

AstraLux is not limited to Lucky Imaging. Depending on the preferences of the observer, the data can be analysed with conventional speckle imaging algorithms as well.
What is more, AstraLux is not restricted to high resolution imaging at all. Its single photon detection capability at frame rates of up to several hundred Hertz makes it a perfect instrument for high speed photometry.

Outlook and Further Developments

In ten nights of observing time, more than 150 different targets have been observed at various wavelengths with AstraLux so far. Observations of the three largest samples – young nearby stars in moving groups, T Tauri binaries, and nearby M dwarfs – have resulted in a large amount of image data, not fully reduced yet. Besides additional astrometry of known binaries, these observations have resulted in the discovery of several potential low-mass companions.

High speed photometry of the Crab pulsar with precise time stamping of the individual frames has been performed in January 2007. The preliminary analysis of the results has shown that AstraLux is able to reconstruct the optical pulse profile with a time resolution of 100 µs. The timing *accuracy* is by five orders of magnitude better: the difference between the ephemeris prediction of the pulsar period and the AstraLux measurement is only 0.4 ns at a period length of $\approx$34 ms. The acquired data will allow to measure the absolute time of arrival of the optical emission in four photometric bands, and to determine the radio-optical delay and its dependency on wavelength.

Observations of special targets like binary asteroids, FU Ori stars, microquasars, and X-ray binaries have been performed in collaboration with researchers not only at MPIA. This has raised

considerable interest in the instrument among astronomers working in various fields at different institutes.

While AstraLux has reached a certain standard of data quality, future developments might improve its performance. The pipeline software is certainly on top of the to-do list. Minor improvements will add more stability to the online version and speed up image reconstruction. Several ideas concerning optimisation in the photon counting limit are awaiting realisation and are expected to shift detection limits to fainter magnitudes.
The instrument hardware might be modified as well. Different Barlow lens assemblies would allow changes of pixel scale and field of view. The home-made timing electronics μLux could be replaced by a commercial version with improved functionality. An ambitious goal would be the implementation of a time-resolved polarimetric mode, a very interesting option for further observations of the Crab pulsar. For purely photometric applications, AstraLux could be mounted at the 3.5 m telescope, allowing to observe fainter sources or to achieve higher time resolution at the same signal level.

Ideas for the future of Lucky Imaging at Calar Alto do not stop at improvements of the existing instrument. The large isoplanatic angle would in principle allow to build a Lucky Imaging instrument with a larger field of view, two or three times the 24 arcsec of AstraLux.
Future developments in the EMCCD sector might provide us with noise-free detectors in the $1-2\,\mu$m wavelength range. A *J*-band near-infrared version of AstraLux at the 3.5 m telescope could provide the same Lucky Imaging performance as the current instrument in the *I*-band. This would close the gap in wavelength range towards the *H* and *K*-band where adaptive optics has its strengths.

From July 2007 on, AstraLux will be offered to the astronomical community as a regular Calar Alto instrument. Several astronomers have expressed their intention to apply for observing time or already submitted their proposals. This gives me some confidence that the results of the past year's efforts may have a small but lasting impact on astronomical research at Calar Alto. In this context, it is a more than adequate coincidence that the deadline for observing proposals will be on the same day as the submission of this thesis.

Chapter A

The 70 cm telescope pointing model

The pointing accuracy of the MPIA 70 cm telescope is typically on the order of 10−20′. While this is sufficient to reliably acquire targets with the 2k×2k CCD which is usually mounted, the small field of view of the DVC camera used in the first Lucky Imaging tests made it necessary to bring down this pointing error considerably. In the course of this thesis an analytic pointing model was applied, reducing the pointing residuals to well below 1′. This model can be accessed through a graphical user interface and is still in use for normal operations at the telescope today (see Figure A.1).

In principle, pointing models can follow two different approaches. Without any knowledge of the pointing error sources, it is possible to fit a high-order polynomial to the differences between apparent coordinates and the positions where the telescope was pointed to. This method can work remarkably well, but requires a large amount of calibration data to allow a stable fit.
A more sophisticated approach is to use an analytic model of the telescope mechanics and optics, e.g. to consider flexures, misalignments of the telescope with respect to the celestial pole, or misalignments of optical and mechanical axes.

The model adopted for the 70 cm telescope is fully analytic and heavily based on the work of Buie (2003), who developed a simplified set of model equations based on Spillar et al. (1993). The actual terms considered for the MPIA telescope are:

- Zero-point offsets in declination and hour angle
- Non-orthogonality of polar axis and declination axis
- Misalignment of optical and mechanical axes
- Tube flexure
- Angular separation between instrumental and celestial pole
- Angle between true meridian and line of true and instrumental poles
- Bending of the declination axis

In principle, one can also fit non-linearities of the hour angle worm-gear, but this was omitted here. Buie (2003) shows how the above terms can be expressed by a set of linear equations, relating the differences between true and intended pointing to a set of eight model coefficients.

In early January 2006, a total of 65 calibration images with uniform distribution on the sky were obtained. For each image the sidereal time and the telescope coordinates as displayed by the telescope control system were recorded. All images were astrometrically solved with the

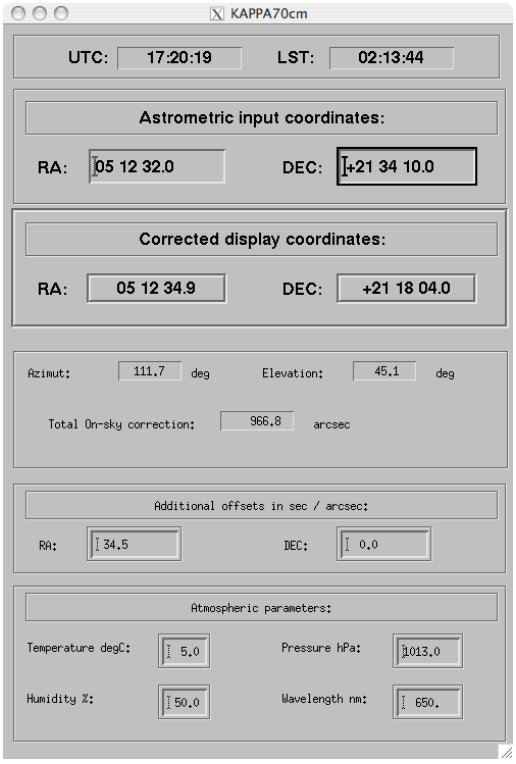

Figure A.1. *The pointing model GUI of the 70 cm telescope. The user enters astrometric J2000.0 catalogue coordinates and reads off the final position where the telescope has to be pointed. The apparent elevation and azimuth of the object as well as the difference between corrected and uncorrected position are displayed. In the bottom part of the interface, the user can change the atmospheric parameters used for refraction correction. Additional constant offsets can be introduced to compensate for drifts of the coordinate zeropoints.*

UCAC-2 catalogue to obtain the actual plate centres with sub-arcsecond precision. The model coefficients were then determined by a least-squares fit. It should be noted that the fit is not made to the differences between telescope coordinates and the *astrometric*, but the *apparent* coordinates of the plate centre. These include corrections due to precession, nutation, aberration and refraction.

Table A.1 compares the pointing performance before and after application of the pointing model. The pointing residuals were greatly reduced, and observations with small fields of view at the 70 cm telescope were enabled without the cost of additional target acquisition overheads.

Table A.1. *Pointing accuracy without and with pointing correction. Applying the described model reduces the RMS by a factor of ≈100 in right ascension (α) and ≈10 in declination (δ).*

	Pre-Fit		Post-Fit	
	α	δ	α	δ
RMS	335″	37.″8	4.″05	3.″61
Worst	904″	1121″	10.″18	8.″78
Best	5.″33	988″	0.″23	0.″04
Peak-to-peak	1038″	133″	19.″75	15.″80

Chapter B

Filters

This chapter provides a consistent overview of all optical filters used during AstraLux observations and Lucky Imaging tests with the conventional CCD . The actual filter composition, physical thickness, centre wavelength and bandwidth are given. The external transmission curve is reproduced in its original form as well as after convolution with the camera's quantum efficiency and the transmission profile of a 1.3 airmass model atmosphere. Mirror coating reflectivity is not included in these plots. All filter curves are accessible in electronic form within the AstraLux data reduction environment.

B.1 Filters for Observations with a Conventional CCD

Effective wavelengths and the effective FWHM of the filter bandpass refer to the combination with the DVC camera used for the Lucky Imaging tests at the MPIA 70 cm telescope. The filter transmission curves are based on own measurements.

Table B.1. *Properties of the conventional CCD observation filters. While λ_{cen} and FWHM refer to the external filter transmission, λ_{eff} and $FWHM_{eff}$ include the atmospheric transmission profile and the camera quantum efficiency.*

Filter name	Composition	λ_{cen} [nm]	FWHM [nm]	λ_{eff} [nm]	$FWHM_{eff}$ [nm]
R	OG 550 / 3 mm + Calflex X / 1 mm	641	162	656	116
I	RG 780 / 3 mm	– –	– –	864	123

B.2 AstraLux Filters

Effective wavelengths and the effective FWHM of the filter bandpass now refer to the convolution with the AstraLux camera's quantum efficiency curve. Please note that the SDSS z' filter will be replaced by an interference filter with improved throughput from May 2007 on. A new SDSS i'

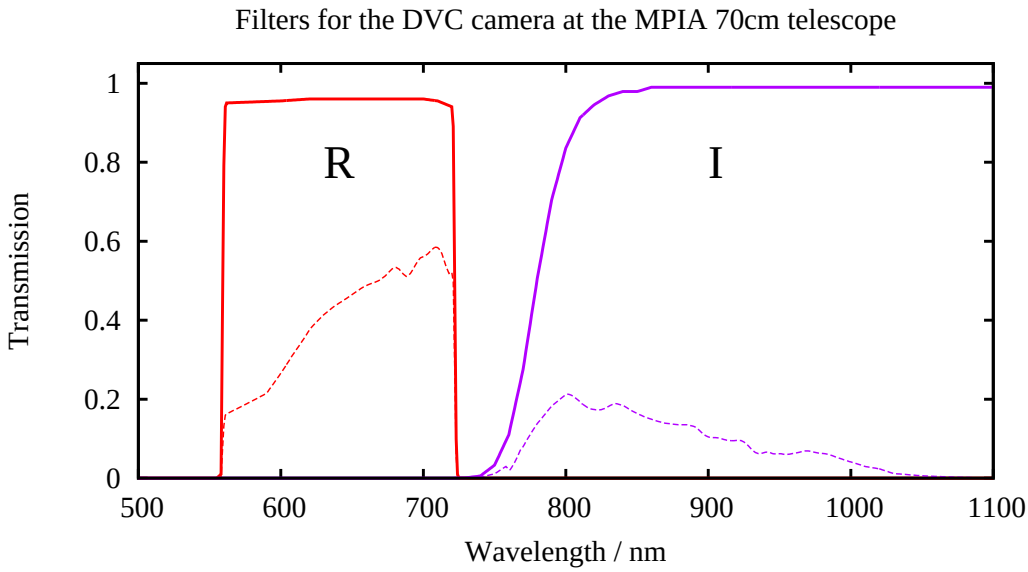

Figure B.1. *Transmission curves of the filters used for observations with the DVC camera at the MPIA 70 cm telescope. The solid lines represent the external filter transmission, the dashed lines include atmospheric transmission and the CCD's quantum efficiency.*

interference filter will be available at the same time. The filter data will be available at the telescope and on the the AstraLux webpages[1].

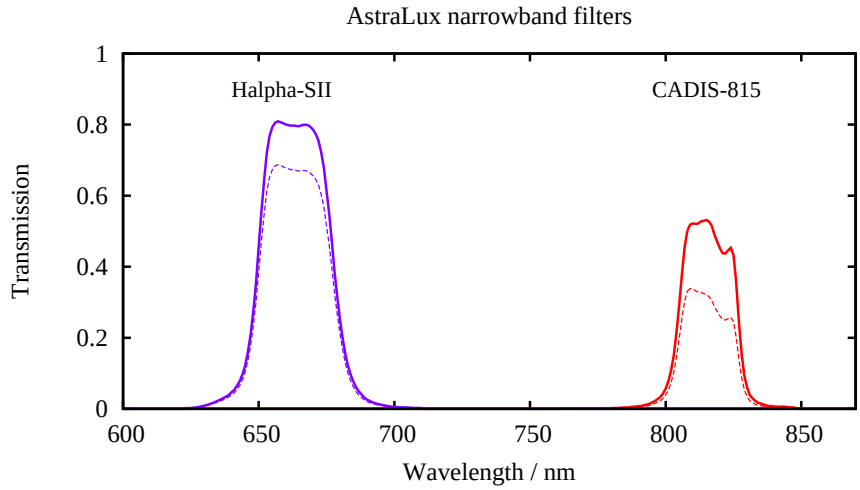

Figure B.2. *Transmission curves of the narrowband filters used with AstraLux. The solid lines represent the external filter transmission, the dashed lines include atmospheric transmission and the CCD's quantum efficiency.*

[1] `http://www.mpia.de/ASTRALUX`

Table B.2. *Properties of filters used during AstraLux observations. While λ_{cen} and FWHM refer to the external filter transmission, λ_{eff} and $FWHM_{eff}$ include the atmospheric transmission profile and the camera quantum efficiency.*

Filter name	Composition	λ_{cen} [nm]	FWHM [nm]	λ_{eff} [nm]	$FWHM_{eff}$ [nm]	Ref.[1]
GG 385	GG 385 / 3 mm	– –	– –	667	474	D
OG 550	OG 550 / 3 mm	– –	– –	734	335	M
RG 610	RG 610 / 3 mm	– –	– –	768	280	D
RG 9	RG 9 / 3 mm	888	314	834	168	M
RG 1000	RG 1000 / 3 mm	– –	– –	982	127	M
Hα-SII	Interference 2.2 mm	664	27	664	27	C
CADIS-815	Interference 5 mm	815	21	815	21	C
B	BG 37 / 1 mm + BG 39 / 2 mm	466	87	474	87	C
V	BG 39 / 2 mm + GG 495 / 1 mm	546	108	547	108	C
R	OG 570 / 2 mm + Calflex X / 1 mm	645	147	644	147	C
I	RG 780 / 3 mm	– –	– –	873	150	C
SDSS z'	RG 830 / 3 mm	– –	– –	911	100	M

Filter curve references:
C: Calar Alto filter database,
available online at `http://www.caha.es/CAHA/Instruments/filterlist.html`
D: Manufacturer datasheet
M: Measurement at MPIA

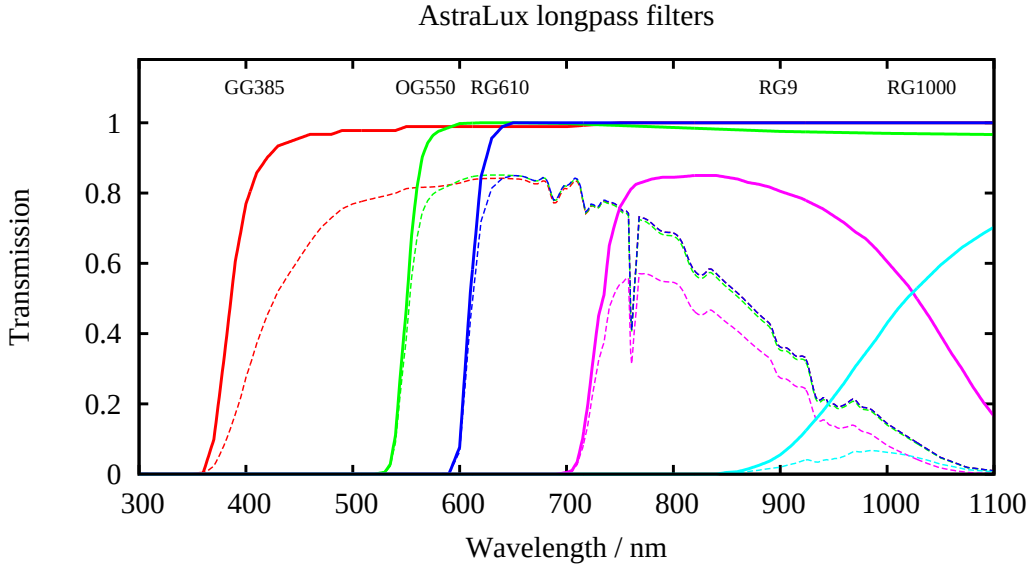

Figure B.3. *Transmission curves of the single-layer longpass filters used for AstraLux observations. The solid lines represent the external filter transmission, the dashed lines include atmospheric transmission and the CCD's quantum efficiency.*

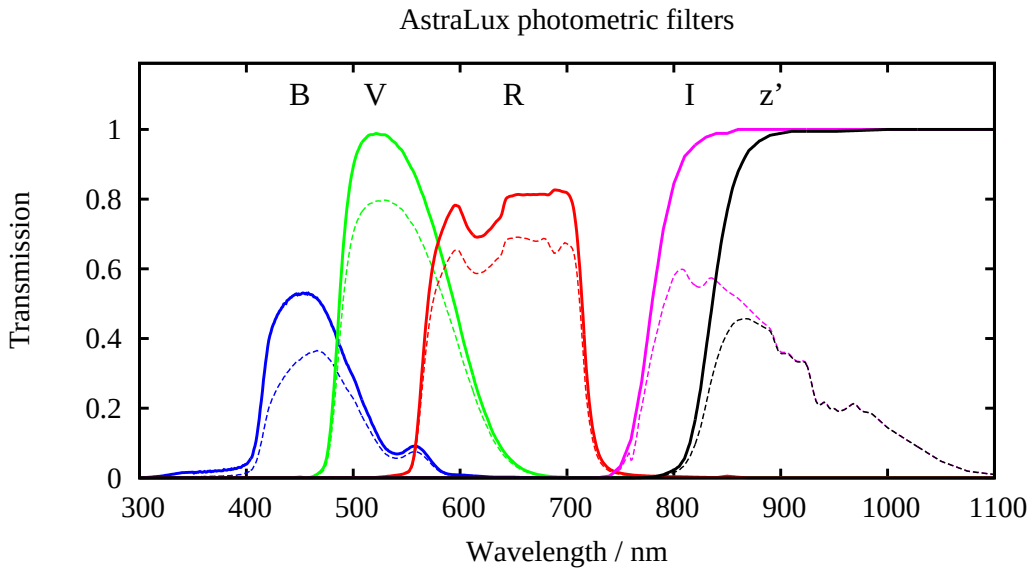

Figure B.4. *Transmission curves of the photometric filters used with AstraLux. The solid lines represent the external filter transmission, the dashed lines include atmospheric transmission and the CCD's quantum efficiency.*

Chapter C

Measuring CCD Analogue Gain and Readout Noise

For comprehensive overviews of the various methods available for CCD characterisation and testing, the interested reader is referred to e.g. Howell (2000) or Berry and Burnell (2005). This chapter describes only the algorithms that were actually used for gain and noise measurements of the AstraLux camera.

C.1 Readout Noise

For the readout noise measurements, bias frames were acquired at unity electron gain to avoid contamination by dark current and CIC events. Using a pair of bias frames B_1 and B_2, the readout noise $\sigma_{readout}$ in ADU is given by:

$$\sigma_{readout} = \frac{\sigma_{B_1-B_2}}{\sqrt{2}}, \tag{C.1}$$

where $\sigma_{B_1-B_2}$ is the standard deviation of the difference image of the two bias frames. This method delivers the pure readout noise without any contribution from bias structure or bias gradients, as it would be the case if the standard deviation of a single image was calculated. The measurements given in this work are based on typically 20−40 bias frame pairs per camera setting.

C.2 Analogue Gain

Measurements of the analogue gain are based on classical mean signal versus variance plots. The chosen method accounts for flatfield effects of the CCD and intensity variations of the calibration lightsource, removing any non-linear terms from the mean/variance relation. Two flatfield images F_1 and F_2 are obtained at 10−20 different intensity levels, plus a high SNR master bias frame B. The second flatfield image is normalised to the illumination level of the first by calculating the

ratio between the mean signal of both frames:

$$F_2 = (F_2^{raw} - B) \cdot \frac{\overline{(F_1^{raw} - B)}}{\overline{(F_2^{raw} - B)}}, \tag{C.2}$$

The subtraction of the normalised and bias corrected images from each other removes any flatfield structure, and the result is used to compute the variance:

$$\sigma^2 = \left(\frac{\sigma_{F_1 - F_2}}{\sqrt{2}} \right)^2 \tag{C.3}$$

The mean intensity of $\overline{(F_1^{raw} - B)}$ is plotted against this variance, and the slope of a linear fit then delivers the conversion factor in e^-/ADU.

Chapter D

μLux - GPS based High Precision Timing

The μLux system is a GPS based high precision time-stamping add-on for AstraLux. The start times of individual images can be recorded with sub-microsecond accuracy with respect to the UTC frame at acquisition rates of up to 1000 Hz. The following sections are a short status report on the interesting domain of high speed photometry with AstraLux.

D.1 Hardware

The actual design was driven by availability and cost considerations for the individual components. While commercial solutions for time-stamping applications are available for typically several thousand Euro, μLux had to be built for less than 1000 Euro as it was a private development of the author.

Figure D.2 shows the block layout of μLux. The heart of the system is a commercial GPS receiver board, model Jupiter 12 from Navman Ltd., UK. Upon reception of at least four GPS satellites, this module delivers a stable 1 Hz and 10 kHz signal, aligned to each other and with respect to the UTC second with an accuracy better than 50 ns. For this, only an external GPS antenna and a very stable power supply are necessary.

The 10 kHz signal is used to stabilise the frequency of an ovenized 10 MHz crystal oscillator via a standard PLL circuit, consisting of phase detector, 1:1000 frequency divider, and control voltage generator. This 10 MHz signal is connected to the input of a synchronous 24 bit counter, which is reset at every full UTC second by the 1 Hz signal of the GPS module. At any given moment, the counter's value will be the fraction of UTC second, divided by the clock period of 100 ns. An external signal, in this case the TTL "fire pulse" from the camera, which is issued each time a new frame is acquired, causes the counter value to be latched into three 8 bit registers. At the same time, this signal indicates the system's control computer that new timing information is available.

The control computer, a "Foxboard LX" from ACME systems, Italy, is an embedded Linux system. It provides various I/O lines, up to four serial ports, two USB ports, and a 100 MBit Ethernet interface. It establishes the connection between the counter hardware and the world

outside and runs a simple command line software to read and store the acquisition start times.

An 8-channel A/D converter with 12 bit resolution is interfaced to the Linux board, allowing monitoring of the various supply voltages, the PLL control voltages and the crystal oven current. This provides full information about the system health and the PLL lock status.

The frame exposure start signal (the "fire" signal) is not directly connected to the Linux system, but first aligned with the 10 MHz master clock and shortened to a pulse length of 50 ns to avoid latch-up conditions or runt pulses in the subsequent stages. After that it is fed into the "trigger board". This simple flip-flop circuit is used to latch the start signal, and to indicate overflow conditions if a second exposure was started before the control computer was able to read out the timing information of the last one. This board also provides an output that can be used to trigger individual exposures or to start a free-running exposure series, hence the name trigger board.

The complete system, shown in Figure D.1, fits into a 19 inch electronics subrack, which can be mounted in the AstraLux computer rack at the 2.2 m telescope mirror cell. A low loss antenna cable with 50 m total length is used to connect a cheap planar outdoor antenna, of the same type as the antennas used for car navigation. The antenna is mounted on the dome's catwalk, at approximately 5 m distance from the dome itself. During the first tests in January 2007, this setup allowed to reliably acquire at least seven satellites with good signal strength during the whole run.

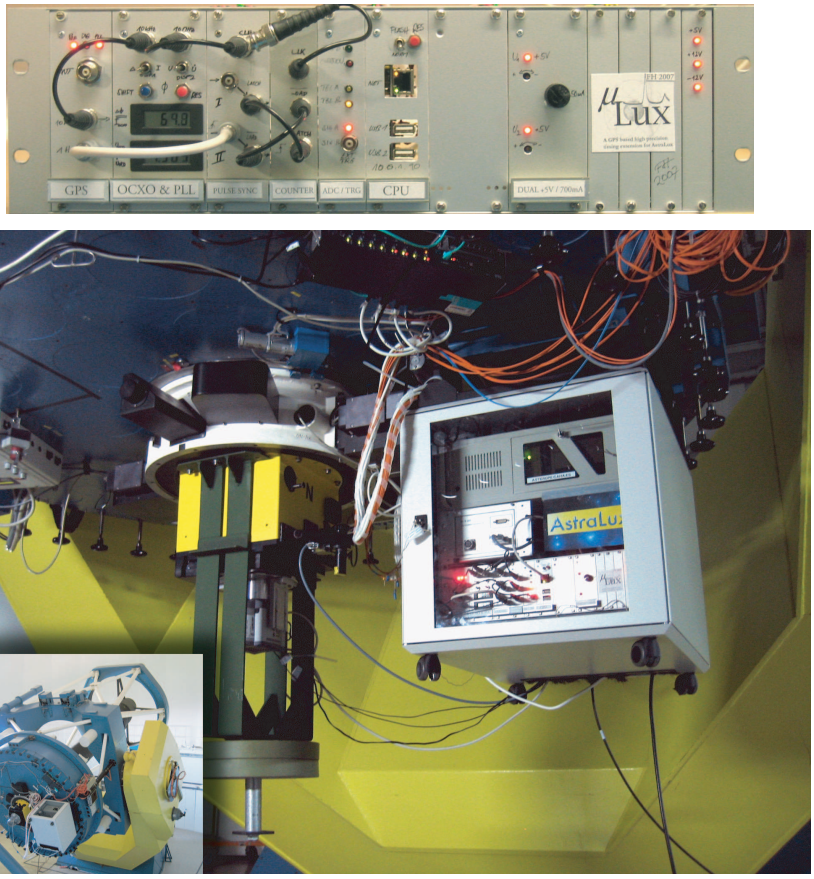

Figure D.1. *Top: close-up of the μLux system. Bottom: AstraLux and μLux at the Calar Alto 2.2 m telescope. For the January 2007 run, an additional weight had been attached to the* Instrumentenansatz 1 *to test if the tracking performance of the telescope can be improved.*

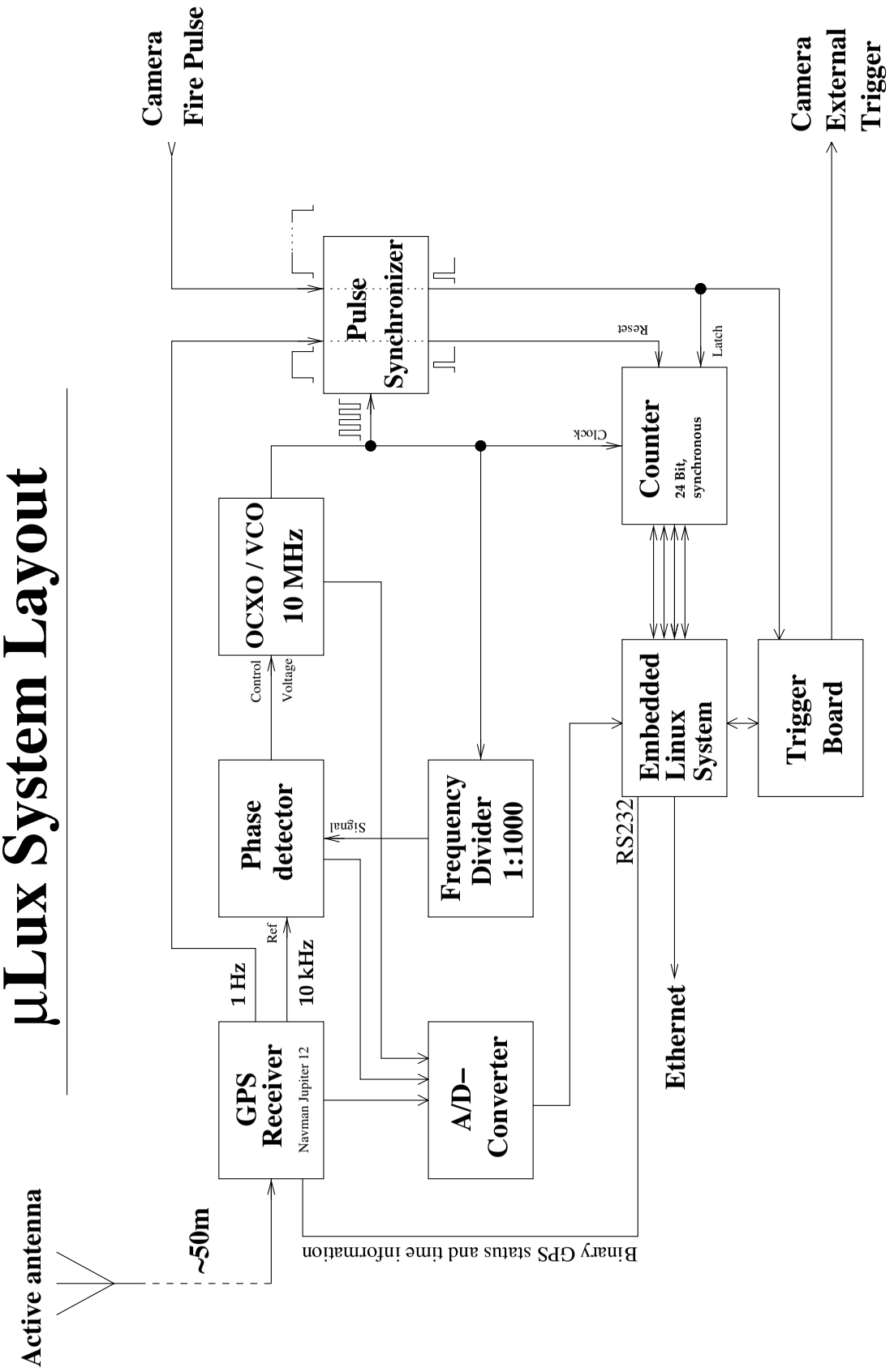

Figure D.2. *Block layout of the µLux GPS based timing system for AstraLux.*

D.2 Software

A cross-platform development kit allows to write software for the FoxBoard on any Linux PC. The compiled binary files are simply copied via FTP or SFTP to the target system.

The μLux software is at the moment restricted to a single command line utility. This program is invoked with the number of frames that will be acquired by the camera and a name for the logfile to be generated. Before any frames are acquired, the μLux software will synchronise itself with the UTC second pulses of the GPS system and obtain the full time and date information by decoding the binary data received from the GPS serial port. After synchronisation, the software waits for the next full UTC second to issue a start signal via the trigger board. This signal starts the free-running time-series acquisition of the AstraLux camera.

Each time the trigger board indicates the start of a new frame, the software reads out the counter value, i.e. determines the precise start time of the frame, and stores this information to the control computer's RAM. It is checked and recorded if the trigger board has indicated an overrun condition.

Upon completion of the time series, all frame start times are written to the RAM file system, ready for retrieval via FTP or SFTP. A system health logfile is created, containing system voltage levels and GPS status information for a timespan of 10 s. Both files can be processed with own IDL programs, allowing to assess the quality of the timing information and to check for any anomalies.

D.3 Measurements and Observations

D.3.1 Performance Verification

Before μLux was deployed at the telescope, laboratory tests were conducted to assess the reliability and accuracy of the system. A second GPS receiver, based on a Navman Ltd. Jupiter Pico T module was used to generate trigger signals with precisely known frequencies. With a typical timing RMS of less than 30 ns, this module is better than the one used in μLux, and will actually replace it in the near future. Up to 700000 time measurements of trigger signals with frequencies between 10 Hz and 1000 Hz, generated with the Pico T module, were acquired with μLux. This is the maximum number of events for which the time information fits into the memory of the FoxBoard. In no case the difference between any two trigger signals in these series differed by more than 100 ns from the predicted value. This is the period length of the counter clock, and hence the expected measurement jitter. The statistical component of the measurement error can hence be assumed to be less than 0.1μs. Including all delays in the electronics between signal input and counter module, the systematic delays are estimated as ≈300 ns. This results in a total timing accuracy of ≤ 0.5μs.

Tests with the AstraLux camera as source of the trigger pulses revealed that the frame rate as predicted by the camera software can differ by up to 0.5% from its actual value. The frame rate shows high stability, though, with quasi-periodic variations of the order of 10 ppm on scales of minutes. They are probably related to temperature changes in the camera control computer housing, causing drifts of the camera control board's master clock frequency. The periodicity most likely reflects the behaviour of the thermostat regulating the speed of the computer's fan.

D.3.2 Observations of the Crab Pulsar

The Crab pulsar, PSR J0534+2200, has a period of ≈34 ms at an average optical magnitude of V=16 mag. Time-resolved observations of its pulse profile were seen as an optimal test case for AstraLux & μLux, making full use of the camera's single photon detection capability and the timing system's accuracy.

In January 2007, several millions of short exposure frames with integration times between 50 μs and 2 ms were acquired in the *B*, *V*, *R*, and *I* filter, as well as unfiltered. Though this data is not in the slightest reduced yet, early on-site analyses have proven that the instrument is able to reconstruct the pulse profile and to reliably reproduce the pulsar period as predicted by radio observations. The data will ultimately allow measurements of the radio-optical delay and its dependency on wavelength. Figure D.3 shows the reconstructed pulse profile, generated from 700000 *V*-band images with 1.6 ms single frame exposure time. The image in the top right corner shows the pulsar at maximum brightness and a nearby star northeast of it.

Before this profile could be reconstructed, the pulsar period including corrections due to pulsar spindown and Doppler effects from earth rotation and earth's orbital motion had to be determined to group the single images into phase bins. Instead of using a theoretical prediction, the period was measured in the optical data itself by using a phase dispersion minimisation (PDM) technique after a first guess of the period by FFT analysis.
The adopted period length was 0.033599726 ± 10^{-9} s. The radio-based theoretical prediction for the time and location of this observation was kindly computed by Michael Kramer of Jodrell Bank's pulsar group: 0.03359972563 s. The difference between the two values is only 0.4 ns, well within the error bar estimated from the PDM algorithm. This corresponds to a relative accuracy of 10^{-7}, or a phase error of ≈1° for the full 33600 pulsar periods that were covered by the data set used in this example. This result impressively confirms that μLux performs well and might provide a valuable extension of AstraLux's capabilities.

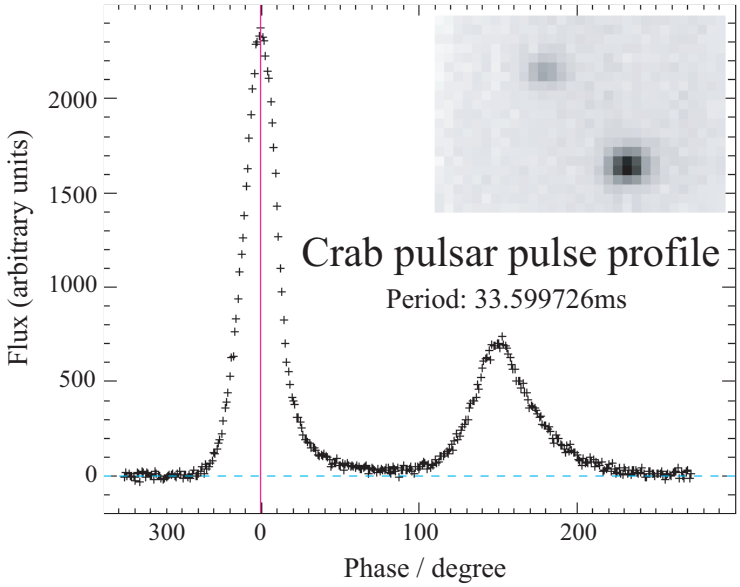

Figure D.3. *The V-band pulse profile of the Crab pulsar, as seen by μLux and AstraLux. The reconstructed profile is based on 700000 images with a single frame exposure time of 1.6 ms. The inset shows the pulsar at maximum brightness. In long-exposure images, the star to the northeast would appear considerably brighter than the pulsar.*

Bibliography

Aime, C., Borgnino, J., Martin, F., Petrov, R. and Ricort, G. (1986), "Contribution to the space-time study of stellar speckle patterns", *JOSA*, Vol. 3, pp. 1001–1009.

Allard, F., Hauschildt, P. H., Alexander, D. R. and Starrfield, S. (1997), "Model Atmospheres of Very Low Mass Stars and Brown Dwarfs", *ARA&A*, Vol. 35, pp. 137–177.

Arsenault, R., Salmon, D. A., Kerr, J. M., Rigaut, F. J., Crampton, D. and Grundmann, W. A. (1994), PUEO: the Canada-France-Hawaii Telescope adaptive optics bonnette I: system description, *in* M. A. Ealey and F. Merkle, eds, 'Proc. SPIE Vol. 2201, Adaptive Optics in Astronomy', pp. 833–842.

Avila, G., Rupprecht, G. and Beckers, J. M. (1997), Atmospheric dispersion correction for the FORS Focal Reducers at the ESO VLT, *in* A. L. Ardeberg, ed., 'Proc. SPIE Vol. 2871, Optical Telescopes of Today and Tomorrow', pp. 1135–1143.

Avila, R., Vernin, J. and Cuevas, S. (1998), "Turbulence Profiles with Generalized SCIDAR at San Pedro Mártir Observatory and Isoplanatism Studies", *PASP* , Vol. 110, pp. 1106–1116.

Baldwin, J. E., Tubbs, R. N., Cox, G. C., Mackay, C. D., Wilson, R. W. and Andersen, M. I. (2001), "Diffraction-limited 800 nm imaging with the 2.56 m Nordic Optical Telescope", *A&A*, Vol. 368, pp. L1–L4.

Baraffe, I., Chabrier, G., Allard, F. and Hauschildt, P. H. (1998), "Evolutionary models for solar metallicity low-mass stars: mass-magnitude relationships and color-magnitude diagrams", *A&A*, Vol. 337, pp. 403–412.

Basden, A. G., Haniff, C. A. and Mackay, C. D. (2003), "Photon counting strategies with low-light-level CCDs", *MNRAS*, Vol. 345, pp. 985–991.

Behrend, R., Bernasconi, L., Roy, R., Klotz, A., Colas, F., Antonini, P., Aoun, R., Augustesen, K., Barbotin, E., Berger, N., Berrouachdi, H., Brochard, E., Cazenave, A., Cavadore, C., Coloma, J., Cotrez, V., Deconihout, S., Demeautis, C., Dorseuil, J., Dubos, G., Durkee, R., Frappa, E., Hormuth, F., Itkonen, T., Jacques, C., Kurtze, L., Laffont, A., Lavayssière, M., Lecacheux, J., Leroy, A., Manzini, F., Masi, G., Matter, D., Michelsen, R., Nomen, J., Oksanen, A., Pääkkönen, P., Peyrot, A., Pimentel, E., Pray, D., Rinner, C., Sanchez, S., Sonnenberg, K., Sposetti, S., Starkey, D., Stoss, R., Teng, J.-P., Vignand, M. and Waelchli, N. (2006), "Four new binary minor planets: (854) Frostia, (1089) Tama, (1313) Berna, (4492) Debussy", *A&A*, Vol. 446, pp. 1177–1184.

Benner, L. A. M., Nolan, M. C., Ostro, S. J., Giorgini, J. D., Pray, D. P., Harris, A. W., Magri, C. and Margot, J.-L. (2006), "Near-Earth Asteroid 2005 CR37: Radar images and photometry of a candidate contact binary", *Icarus*, Vol. 182, pp. 474–481.

Berkefeld, T., Glindemann, A. and Hippler, S. (2001), "Multi-Conjugate Adaptive Optics with Two Deformable Mirrors - Requirements and Performance", *Exp. Astron.*, Vol. 11, pp. 1–21.

Berry, R. and Burnell, J. (2005), *The Hanbdbook of Astronomical Image Processing*, Willmann-Bell.

Bessell, M. S. and Weis, E. W. (1987), "The Cousins and Kron VRI systems", *PASP*, Vol. 99, pp. 642–644.

Beuzit, J.-L., Ségransan, D., Forveille, T., Udry, S., Delfosse, X., Mayor, M., Perrier, C., Hainaut, M.-C., Roddier, C., Roddier, F. and Martín, E. L. (2004), "New neighbours. III. 21 new companions to nearby dwarfs, discovered with adaptive optics", *A&A*, Vol. 425, pp. 997–1008.

Born, M. (1999), *Principles of optics: 7th (expanded) edition*, Cambridge University Press.

Bouy, H., Brandner, W., Martín, E. L., Delfosse, X., Allard, F. and Basri, G. (2003), "Multiplicity of Nearby Free-Floating Ultracool Dwarfs: A Hubble Space Telescope WFPC2 Search for Companions", *AJ*, Vol. 126, pp. 1526–1554.

Brandner, W. and Kasper, M. E., eds (2005), *Science with Adaptive Optics, Proceedings of the ESO Workshop Held at Garching, Germany, 16-19 September 2003*, Springer.

Buie, M. W. (2003), 'General Analytical Telescope Pointing Model', available at http://www.lowell.edu/users/buie/ idl/downloads/pointing/pointing.pdf.

Butler, D. J., Hippler, S., Egner, S., Xu, W. and Bähr, J. (2004), "Broadband, Static Wave-Front Generation: Na-Ag Ion-Exchange Phase Screens and Telescope Emulation", *Appl. Opt.*, Vol. 43, pp. 2813–2823.

Carbillet, M., Vérinaud, C., Femenía, B., Riccardi, A. and Fini, L. (2005), "Modelling astronomical adaptive optics - I. The software package CAOS", *MNRAS*, Vol. 356, pp. 1263–1275.

Christou, J. C. (1991), "Image quality, tip-tilt correction, and shift-and-add infrared imaging", *PASP*, Vol. 103, pp. 1040–1048.

Ciddor, P. E. (1996), "Refractive index of air: new equations for the visible and near infrared", *Appl. Opt.*, Vol. 35, pp. 1566.

Close, L. M. and McCarthy, Jr., D. W. (1994), "High-resolution imaging with a tip-tilt Cassegrain secondary", *PASP*, Vol. 106, pp. 77–86.

Cohen, R. L., Guhathakurta, P., Yanny, B., Schneider, D. P. and Bahcall, J. N. (1997), "Globular Cluster Photometry with the Hubble Space Telescope.VI.WF/PC-I Observations of the Stellar Populations in the Core of M13 (NGC 6205)", *AJ*, Vol. 113, pp. 669–681.

Daigle, O., Gach, J.-L., Guillaume, C., Carignan, C., Balard, P. and Boisin, O. (2004), L3CCD results in pure photon-counting mode, *in* J. D. Garnett and J. W. Beletic, eds, 'Optical and Infrared Detectors for Astronomy. Proceedings of the SPIE, Volume 5499', pp. 219–227.

Dainty, J. C., Hennings, D. R. and Odonnell, K. A. (1981), "Space-time correlation of stellar speckle patterns", *JOSA*, Vol. 71, pp. 490–492.

Douglass, G. G., Hindsley, R. B. and Worley, C. E. (1997), "Speckle Interferometry at the US Naval Observatory. I.", *ApJS*, Vol. 111, pp. 289.

Ducourant, C., Teixeira, R., Périé, J. P., Lecampion, J. F., Guibert, J. and Sartori, M. J. (2005), "Pre-main sequence star Proper Motion Catalogue", *A&A*, Vol. 438, pp. 769–778.

Duquennoy, A. and Mayor, M. (1991), "Multiplicity among solar-type stars in the solar neighbourhood. II - Distribution of the orbital elements in an unbiased sample", *A&A*, Vol. 248, pp. 485–524.

Egner, S. E. (2003), Optical Turbulence Estimation and Emulation, Master's thesis, University of Heidelberg.

Egner, S. E., Masciadri, E., McKenna, D., Herbst, T. M. and Gaessler, W. (2006), G-SCIDAR measurements on Mt. Graham: recent results, *in* B. L. Ellerbroek and D. Bonaccini Calia, eds, 'Advances in Adaptive Optics II. Proceedings of the SPIE', Vol. 6272, p. 165.

Filippenko, A. V. (1982), "The importance of atmospheric differential refraction in spectrophotometry", *PASP*, Vol. 94, pp. 715–721.

Forrest, W. J., Shure, M. and Skrutskie, M. F. (1988), "A possible brown dwarf companion to Gliese 569", *ApJ*, Vol. 330, pp. L119–L123.

Fried, D. L. (1965), "Statistics of a Geometric Representation of Wavefront Distortion", *JOSA*, Vol. 55, pp. 1427–1435.

Fried, D. L. (1978), "Probability of getting a lucky short-exposure image through turbulence", *JOSA*, Vol. 68, pp. 1651–1658.

Fruchter, A. S. and Hook, R. N. (2002), "Drizzle: A Method for the Linear Reconstruction of Undersampled Images", *PASP*, Vol. 114, pp. 144–152.

Fuhrmann, K. (2004), "Nearby stars of the Galactic disk and halo. III.", *Astron. Nachr.*, Vol. 325, pp. 3–80.

Fukugita, M., Ichikawa, T., Gunn, J. E., Doi, M., Shimasaku, K. and Schneider, D. P. (1996), "The Sloan Digital Sky Survey Photometric System", *AJ*, Vol. 111, pp. 1748.

Gálvez, M. C., Montes, D., Fernández-Figueroa, M. J. and López-Santiago, J. (2006), "Chromospheric Activity and Orbital Solution of Six New Late-type Spectroscopic Binary Systems", *Ap&SS*, Vol. 304, pp. 59–61.

Gizis, J. E., Reid, I. N. and Hawley, S. L. (2002), "The Palomar/MSU Nearby Star Spectroscopic Survey. III. Chromospheric Activity, M Dwarf Ages, and the Local Star Formation History", *AJ*, Vol. 123, pp. 3356–3369.

Guhathakurta, P., Yanny, B., Bahcall, J. N. and Schneider, D. P. (1994), "Globular cluster photometry with the Hubble Space Telescope. 3: Blue stragglers and variable stars in the core of M3", *AJ*, Vol. 108, pp. 1786–1809.

Halbwachs, J. L., Mayor, M., Udry, S. and Arenou, F. (2003), "Multiplicity among solar-type stars. III. Statistical properties of the F7-K binaries with periods up to 10 years", *A&A*, Vol. 397, pp. 159–175.

Hardy, J. W. (1998), *Adaptive Optics for Astronomical Telescopes*, Oxford University Press.

Hartkopf, W. I. and Mason, B. D. (2006), 'Sixth Catalog of Orbits of Visual Binary Stars', published online at http://ad.usno.navy.mil/wds/orb6.html.

Hartkopf, W. I., McAlister, H. A., Mason, B. D., ten Brummelaar, T., Roberts, Jr., L. C., Turner, N. H. and Wilson, J. W. (1997), "ICCD Speckle Observations of Binary Stars. XVII. Measurements During 1993-1995 From the Mount Wilson 2.5-M Telescope.", *AJ*, Vol. 114, pp. 1639.

Hecquet, J. and Coupinot, G. (1985), "A gain in resolution by the superposition of selected recentered short exposures", *Journal of Optics*, Vol. 16, pp. 21–26.

Henry, G. W., Fekel, F. C. and Hall, D. S. (1995), "An Automated Search for Variability in Chromospherically Active Stars", *AJ*, Vol. 110, pp. 2926.

Hippler, S., Hormuth, F., Butler, D. J., Brandner, W. and Henning, T. (2006), "Atmosphere-like turbulence generation with surface-etched phase-screens", *Optics Express*, Vol. 14, pp. 10139–10148.

Hormuth, F., Brandner, W., Hippler, S., Janson, M. and Henning, T. (2007), "Direct imaging of the young spectroscopic binary HD 160934", *A&A*, Vol. 463, pp. 707–711.

Howell, S. B. (2000), *Handbook of CCD Astronomy*, Cambridge University Press.

Hünsch, M., Schmitt, J. H. M. M., Sterzik, M. F. and Voges, W. (1999), "The ROSAT all-sky survey catalogue of the nearby stars", *A&AS*, Vol. 135, pp. 319–338.

Hynecek, J. and Nishiwaki, T. (2002), Recent progress toward single photon detection using charge multiplying CCD image sensors, *in* 'Proc. 16th World Multiconference on Systems and Cybernetics'.

Itoh, Y., Tamura, M., Hayashi, S. S., Oasa, Y., Fukagawa, M., Kaifu, N., Suto, H., Murakawa, K., Doi, Y., Ebizuka, N., Naoi, T., Takami, H., Takato, N., Gaessler, W., Kanzawa, T., Hayano, Y., Kamata, Y., Saint-Jacques, D. and Iye, M. (2002), "Near-Infrared Coronagraphy of the GG Tauri A Binary System", *PASJ*, Vol. 54, pp. 963–967.

Jerram, P., Pool, P. J., Bell, R., Burt, D. J., Bowring, S., Spencer, S., Hazelwood, M., Moody, I., Catlett, N. and Heyes, P. S. (2001), The LLCCD: low-light imaging without the need for an intensifier, *in* M. M. Blouke, J. Canosa and N. Sampat, eds, 'Proc. SPIE Vol. 4306, Sensors and Camera Systems for Scientific, Industrial, and Digital Photography Applications II', pp. 178–186.

Johnston, D. C. and Welsh, B. M. (1994), "Analysis of multiconjugate adaptive optics", *JOSA*, Vol. 11, pp. 394–408.

Jordi, K., Grebel, E. K. and Ammon, K. (2006), "Empirical color transformations between SDSS photometry and other photometric systems", *A&A*, Vol. 460, pp. 339–347.

Kasper, M., Looze, D. P., Hippler, S., Herbst, T., Glindemann, A., Ott, T. and Wirth, A. (2000), "Alfa: Adaptive optics for the calar alto observatory optics, control systems, and performance", *Exp. Astron.*, Vol. 10, p. 49.

Klueckers, V. A., Wooder, N. J., Nicholls, T. W., Adcock, M. J., Munro, I. and Dainty, J. C. (1998), "Profiling of atmospheric turbulence strength and velocity using a generalised SCIDAR technique", *A&AS*, Vol. 130, pp. 141–155.

Knox, K. T. and Thompson, B. J. (1973), "New methods of processing speckle pattern star images", *AJ*, Vol. 182, p. L133.

Knox, K. T. and Thompson, B. J. (1974), "Recovery of images from atmospherically degraded short-time exposure photographs", *ApJ*, Vol. 193, p. 45.

Köhler, R. and Leinert, C. (1998), "Multiplicity of T Tauri stars in Taurus after ROSAT", *A&A*, Vol. 331, pp. 977–988.

König, B., Guenther, E. W., Woitas, J. and Hatzes, A. P. (2005), "The young active binary star EK Draconis", *A&A*, Vol. 435, pp. 215–223.

Krist, J. and Hook, R. (2004), 'The Tiny Tim User's Guide (Version 6.3)'.

Labeyrie, A. (1970), "Attainment of diffraction limited resolution in large telescopes by fourier analysing speckle patterns in star images", *A&A*, Vol. 6, p. 85.

Labeyrie, A. (1974), "Speckle interferometry and possible extensions", *A&AS*, Vol. 15, p. 463.

Landolt, A. U. (1983), "Ubvri photometric standard stars around the celestial equator", *AJ*, Vol. 88, p. 439.

Landolt, A. U. (1992), "Ubvri photometric standard stars in the magnitude range 11.5-16.0 around the celestial equator", *AJ*, Vol. 104, p. 340.

Law, N. M., Hodgkin, S. T. and Mackay, C. D. (2006), "Discovery of five very low mass close binaries, resolved in the visible with lucky imaging", *MNRAS*, Vol. 368, p. 1917.

Leinert, C. and et al. (1993), "A systematic search for young binaries in taurus", *A&A*, Vol. 278, pp. 129–149.

Lohmann, A. W., Weigelt, G. and Wirnitzer, B. (1983), "Speckle masking in astronomy - Triple correlation theory and applications", *Appl. Opt.*, Vol. 22, pp. 4028–4037.

López-Santiago, J., Montes, D., Crespo-Chacón, I. and Fernández-Figueroa, M. J. (2006), "The Nearest Young Moving Groups", *ApJ*, Vol. 643, pp. 1160–1165.

Lowrance, P. J., Becklin, E. E., Schneider, G., Kirkpatrick, J. D., Weinberger, A. J., Zuckerman, B., Dumas, C., Beuzit, J.-L., Plait, P., Malumuth, E., Heap, S., Terrile, R. J. and Hines, D. C. (2005), "An Infrared Coronagraphic Survey for Substellar Companions", *AJ*, Vol. 130, pp. 1845–1861.

Marchis, F., Descamps, P., Hestroffer, D., Berthier, J., Vachier, F., Boccaletti, A., de Pater, I. and Gavel, D. (2003), "A three-dimensional solution for the orbit of the asteroidal satellite of 22 Kalliope", *Icarus*, Vol. 165, pp. 112–120.

Margot, J.-L. and Brown, M. E. (2001), "S/2001 (22)", *IAUC* 7703.

Mathieu, R. D. (1994), "Pre-Main-Sequence Binary Stars", *ARA&A*, Vol. 32, pp. 465–530.

McAlister, H. A. (1977), "Speckle interferometric measurements of binary stars. I", *ApJ*, Vol. 215, pp. 159–165.

McAlister, H. A., Hartkopf, W. I., Hutter, D. J. and Franz, O. G. (1987), "ICCD speckle observations of binary stars. II - Measurements during 1982-1985 from the Kitt Peak 4 M telescope", *AJ*, Vol. 93, pp. 688–723.

McCarthy, C. and Zuckerman, B. (2004), "The Brown Dwarf Desert at 75-1200 AU", *AJ*, Vol. 127, pp. 2871–2884.

McCaughrean, M. J. and Stauffer, J. R. (1994), "High resolution near-infrared imaging of the trapezium: A stellar census", *AJ*, Vol. 108, pp. 1382–1397.

Merline, W. J., Ménard, F., Close, L., Dumas, C., Chapman, C. R. and Slater, D. C. (2001), "S/2001 (22)", *IAUC* 7703.

Merline, W. J., Weidenschilling, S. J., Durda, D. D., Margot, J. L., Pravec, P. and Storrs, A. D. (2002), *Asteroids Do Have Satellites*, The University of Arizona Press, chapter 2.2, pp. 289–314.

Moffat, A. F. J. (1969), "A Theoretical Investigation of Focal Stellar Images in the Photographic Emulsion and Application to Photographic Photometry", *A&A*, Vol. 3, pp. 455.

Mugrauer, M., Neuhäuser, R., Guenther, E., Brandner, W., Alves, J. and Ammler, M. (2005), Search for sub-stellar companions using ao – first results obtained with naos-conica, *in* W. Brandner and M. Kasper, eds, 'Science with Adaptive Optics', ESO, Springer, pp. 158–160.

Mulliss, C. L. and Bopp, B. W. (1994), "A search for chromospherically active stars from the ROSAT EUV source list", *PASP*, Vol. 106, pp. 822–827.

Noll, K. S., Levison, H. F., Grundy, W. M. and Stephens, D. C. (2006), "Discovery of a binary Centaur", *Icarus*, Vol. 184, pp. 611–618.

Ostro, S. J., Margot, J.-L., Benner, L. A. M., Giorgini, J. D., Scheeres, D. J., Fahnestock, E. G., Broschart, S. B., Bellerose, J., Nolan, M. C., Magri, C., Pravec, P., Scheirich, P., Rose, R., Jurgens, R. F., De Jong, E. M. and Suzuki, S. (2006), "Radar Imaging of Binary Near-Earth Asteroid (66391) 1999 KW4", *Science*, Vol. 314, pp. 1276–1280.

Pandey, J. C., Singh, K. P., Sagar, R. and Drake, S. A. (2002), "Photometric Variability of Four Coronally Active Stars", *JA&A*, Vol. 23, pp. 9.

Perryman, M. A. C., Lindegren, L., Kovalevsky, J., Hoeg, E., Bastian, U., Bernacca, P. L., Crézé, M., Donati, F., Grenon, M., van Leeuwen, F., van der Marel, H., Mignard, F., Murray, C. A., Le Poole, R. S., Schrijver, H., Turon, C., Arenou, F., Froeschlé, M. and Petersen, C. S. (1997), "The HIPPARCOS Catalogue", *A&A*, Vol. 323, pp. L49–L52.

Phillips, A. C., Miller, J., Cowley, D. and Wallace, V. (2006), The Keck-I Cassegrain atmospheric dispersion corrector, *in* 'Ground-based and Airborne Instrumentation for Astronomy. Edited by McLean, Ian S.; Iye, Masanori. Proceedings of the SPIE, Volume 6269', pp. 6269.

Pounds, K. A., Allan, D. J., Barber, C., Barstow, M. A., Bertram, D., Branduardi-Raymont, G., Brebner, G. E. C., Buckley, D., Bromage, G. E., Cole, R. E., Courtier, M., Cruise, A. M., Culhane, J. L., Denby, M., Donoghue, D. O., Dunford, E., Georgantopoulos, I., Goodall, C. V., Gondhalekar, P. M., Gourlay, J. A., Harris, A. W., Hassall, B. J. M., Hellier, C., Hodgkin, S., Jeffries, R. D., Kellett, B. J., Kent, B. J., Lieu, R., Lloyd, C., McGale, P., Mason, K. O., Matthews, L., Mittaz, J. P. D., Page, C. G., Pankiewicz, G. S., Pike, C. D., Ponman, T. J., Puchnarewicz, E. M., Pye, J. P., Quenby, J. J., Ricketts, M. J., Rosen, S. R., Sansom, A. E., Sembay, S., Sidher, S., Sims, M. R., Stewart, B. C., Sumner, T. J., Vallance, R. J., Watson, M. G., Warwick, R. S., Wells, A. A., Willingale, R., Willmore, A. P., Willoughby, G. A. and Wonnacott, D. (1993), "The ROSAT Wide Field Camera all-sky survey of extreme-ultraviolet sources. I - The Bright Source Catalogue", *MNRAS*, Vol. 260, pp. 77–102.

Pravdo, S. H., Rabinowitz, D. L., Helin, E. F., Lawrence, K. J., Bambery, R. J., Clark, C. C., Groom, S. L., Levin, S., Lorre, J., Shaklan, S. B., Kervin, P., Africano, J. A., Sydney, P. and Soohoo, V. (1999), "The Near-Earth Asteroid Tracking (NEAT) Program: an Automated System for Telescope Control, Wide-Field Imaging, and Object Detection", *AJ*, Vol. 117, pp. 1616–1633.

Prieur, J.-L., Koechlin, L., André, C., Gallou, G. and Lucuix, C. (1998), "The 'Pisco' Speckle Camera at Pic Du Midi Observatory", *Exp. Astron.*, Vol. 8, pp. 297–315.

Rabien, S., Davies, R. I., Ott, T., Hippler, S. and Neumann, U. (2002), PARSEC: the laser for the VLT, *in* R. K. Tyson, D. Bonaccini and M. C. Roggemann, eds, 'Proc. SPIE Vol. 4494, Adaptive Optics Systems and Technology II', pp. 325–335.

Ragazzoni, R. (1996), "Pupil plane wavefront sensing with an oscillating prism", *Journal of Modern Optics*, Vol. 43, pp. 289–293.

Reid, I. N., Hawley, S. L. and Gizis, J. E. (1995), "The Palomar/MSU Nearby-Star Spectroscopic Survey. I. The Northern M Dwarfs -Bandstrengths and Kinematics", *AJ*, Vol. 110, pp. 1838.

Riaz, B., Gizis, J. E. and Harvin, J. (2006), "Identification of New M Dwarfs in the Solar Neighborhood", *AJ*, Vol. 132, pp. 866–872.

Robbins, M. S. and Hadwen, B. J. (2003), "The noise performance of electron multiplying charge coupled devices", *IEEE Transactions on Electron Devices*, Vol. 50, pp. 1227–1232.

Roddier, F. (1981), "The Effects of Atmospheric Turbulence in Optical Astronomy", *Prog. Optics*, Vol. 19, pp. 281–376.

Roddier, F. (1988), "Curvature sensing and compensation: a new concept in adaptive optics", *Appl. Opt.*, Vol. 27, pp. 1223–1225.

Roddier, F. (1999), *Adaptive optics in astronomy*, Adaptive Optics in Astronomy.

Roddier, F., Cowie, L., Graves, J. E., Songaila, A. and McKenna, D. (1990), Seeing at Mauna Kea - A joint UH-UN-NOAO-CFHT study, *in* L. D. Barr, ed., 'Advanced technology optical telescopes IV; Proceedings of the Meeting, Tucson, AZ, Feb. 12-16, 1990. Part 1 (A91-23201 08-89). Bellingham, WA, Society of Photo-Optical Instrumentation Engineers, 1990', pp. 485–491.

Roddier, F., Gilli, J. M. and Lund, G. (1982), "On the origin of speckle boiling and its effects in stellar speckle interferometry", *Journal of Optics*, Vol. 13, pp. 263–271.

Rousset, G., Lacombe, F., Puget, P., Hubin, N. N., Gendron, E., Fusco, T., Arsenault, R., Charton, J., Feautrier, P., Gigan, P., Kern, P. Y., Lagrange, A.-M., Madec, P.-Y., Mouillet, D., Rabaud, D., Rabou, P., Stadler, E. and Zins, G. (2003), NAOS, the first AO system of the VLT: on-sky performance, *in* P. L. Wizinowich and D. Bonaccini, eds, 'Adaptive Optical System Technologies II. Proceedings of the SPIE, Volume 4839', pp. 140–149.

Sarazin, M. and Roddier, F. (1990), "The ESO differential image motion monitor", *A&A*, Vol. 227, pp. 294–300.

Scaddan, R. J. and Walker, J. G. (1978), "Statistics of stellar speckle patterns", *Appl. Opt.*, Vol. 17, pp. 3779–3784.

Shack, R. and Platt, B. (1971), "Production and Use of a Lenticular Hartmann Screen", *JOSA*, Vol. 61, p. 656.

Silber, J., Gledhill, T., Duchêne, G. and Ménard, F. (2000), "Near-Infrared Imaging Polarimetry of the GG Tauri Circumbinary Ring", *ApJ*, Vol. 536, pp. L89–L92.

Simon, M., Bender, C. and Prato, L. (2006), "The Gl569 Multiple System", *ApJ*, Vol. 644, pp. 1183–1192.

Skrutskie, M. F., Cutri, R. M., Stiening, R., Weinberg, M. D., Schneider, S., Carpenter, J. M., Beichman, C., Capps, R., Chester, T., Elias, J., Huchra, J., Liebert, J., Lonsdale, C., Monet, D. G., Price, S., Seitzer, P., Jarrett, T., Kirkpatrick, J. D., Gizis, J. E., Howard, E., Evans, T., Fowler, J., Fullmer, L., Hurt, R., Light, R., Kopan, E. L., Marsh, K. A., McCallon, H. L., Tam, R., Van Dyk, S. and Wheelock, S. (2006), "The Two Micron All Sky Survey (2MASS)", *AJ*, Vol. 131, pp. 1163–1183.

Song, I., Zuckerman, B. and Bessell, M. S. (2003), "New Members of the TW Hydrae Association, β Pictoris Moving Group, and Tucana/Horologium Association", *ApJ*, Vol. 599, pp. 342–350.

Spillar, E. J., Dumbrill, D., Grasdalen, G. L. and Howell, R. R. (1993), "The Wyoming Infrared Observatory telescope software system", *PASP*, Vol. 105, pp. 616–624.

Stone, R. C. (1996), "An Accurate Method for Computing Atmospheric Refraction", *PASP*, Vol. 108, pp. 1051–1058.

Strehl, K. (1902), "Über Luftschlieren und Zonenfehler", *Zeitschrift für Instrumentenkunde*, Vol. 22, p. 213.

Tatarski, W. I. (1961), *Wave Propagation in a Turbulent Medium*, McGraw-Hill, New York.

Taylor, G. I. (1938), "The spectrum of turbulence", *Proc. R. Soc. A*, Vol. 164, p. 476.

Tokovinin, A. (2004), "Seeing Improvement with Ground-Layer Adaptive Optics", *PASP*, Vol. 116, pp. 941–951.

Tubbs, R. N. (2003), Lucky Exposures: Diffraction Limited Astronomical Imaging Through the Atmosphere, PhD thesis, University of Cambridge.

Tubbs, R. N., Baldwin, J. E., Mackay, C. D. and Cox, G. C. (2002), "Diffraction-limited CCD imaging with faint reference stars", *A&A*, Vol. 387, pp. L21–L24.

Tucker, D. L., Allyn Smith, J. and Brinkmann, J. (2001), The Sloan Digital Sky Survey Standard Star Network., *in* R. Clowes, A. Adamson and G. Bromage, eds, 'ASP Conf. Ser. 232: The New Era of Wide Field Astronomy', pp. 13.

van Dam, M. A., Bouchez, A. H., Le Mignant, D., Johansson, E. M., Wizinowich, P. L., Campbell, R. D., Chin, J. C. Y., Hartman, S. K., Lafon, R. E., Stomski, Jr., P. J. and Summers, D. M. (2006), "The W. M. Keck Observatory Laser Guide Star Adaptive Optics System: Performance Characterization", *PASP*, Vol. 118, pp. 310–318.

Vernin, J. and Munoz-Tunon, C. (1994), "Optical seeing at La Palma Observatory. 2: Intensive site testing campaign at the Nordic Optical Telescope", *A&A*, Vol. 284, pp. 311–318.

Weaver, H. A., Stern, S. A., Mutchler, M. J., Steffl, A. J., Buie, M. W., Merline, W. J., Spencer, J. R., Young, E. F. and Young, L. A. (2006), "Discovery of two new satellites of Pluto", *Nature*, Vol. 439, pp. 943–945.

Weis, E. W. (1991), "VRI photometry of late dwarf common proper motion pairs", *AJ*, Vol. 101, pp. 1882–1901.

Weis, E. W. (1993), "Photometry of dwarf K and M stars", *AJ*, Vol. 105, pp. 1962–1966.

Winker, D. M. (1991), "Effect of a finite outer scale on the Zernike decomposition of atmospheric optical turbulence", *JOSA*, Vol. 8, pp. 1568–1573.

Wynne, C. G. (1993), "A new form of atmospheric dispersion corrector", *MNRAS*, Vol. 262, pp. 741–748.

Yanny, B., Guhathakurta, P., Bahcall, J. N. and Schneider, D. P. (1994), "Globular cluster photometry with the Hubble Space Telescope. 2: U, V, and I measurements of M15", *AJ*, Vol. 107, pp. 1745–1763.

Ziad, A., Gredel, R., Aceituno, J., Borgnino, J., Hoyo, F., Irbah, A., Martin, F., Thiele, U. and Pedraz, S. (2005), "A site-testing campaign at the Calar Alto Observatory with GSM and DIMM instruments", *MNRAS*, Vol. 362, pp. 455–459.

Ziad, A., Martin, F., Conan, R. and Borgnino, J. (2002), GSM: a monitor of wavefront optical parameters for the site evaluation, *in* J. Vernin, Z. Benkhaldoun and C. Muñoz-Tuñón, eds, 'ASP Conf. Ser. 266: Astronomical Site Evaluation in the Visible and Radio Range', p. 114.

Zuckerman, B. and Song, I. (2004), "Young Stars Near the Sun", *ARA&A*, Vol. 42, pp. 685–721.

Zuckerman, B., Song, I. and Bessell, M. S. (2004), "The AB Doradus Moving Group", *ApJ*, Vol. 613, pp. L65–L68.

Zuckerman, B., Song, I., Bessell, M. S. and Webb, R. A. (2001), "The β Pictoris Moving Group", *ApJ*, Vol. 562, pp. L87–L90.

Appendix

List of Acronyms & Abbreviations

2MASS	Two Micron All Sky Survey
ACS	Advanced Camera for Surveys
ADC	Analogue-to-Digital Converter
ADU	Analogue-Digital-Unit
AO	Adaptive Optics
A.U.	Astronomical Unit
BUSCA	Bonn University Simultaneous Camera
CAFOS	Calar Alto Faint Object Spectrograph
CAOS	Code for Adaptive Optics Systems
CCD	Charge Coupled Device
CFHT	Canada France Hawaii Telescope
CIC	Clock Induced Charge(s)
DC	Dark Current
DIMM	Differential Image Motion Monitor
DSS	Digital Sky Survey
EM	Electron Multiplication
EMCCD	Electron Multiplying Charge Coupled Device
ESO	European Southern Observatory
FITS	Flexible Image Transport System
FFT	Fast Fourier Transform
FK 4/5	*Fundamentalkatalog* 4/5
FOV	Field of View
FTP	File Transfer Protocol
FWHM	Full Width at Half Maximum
GLAO	Ground Layer Adaptive Optics
GPS	Global Positioning System
GSM	Generalised Seeing Monitor
GUI	Graphical User Interface
HST	Hubble Space Telescope
IAU	International Astronomical Union
ICRS	International Celestial Reference System

IDL	Interactive Data Language
IMCCE	*Institut de mécanique céleste et de calcul des éphémérides*
IR	Infrared
JWST	James Webb Space Telescope
mas	milli-arcsecond
MCAO	Multi-conjugated Adaptive Optics
MPIA	*Max-Planck-Institut für Astronomie*
MTF	Modulation Transfer Function
NACO	NAOS-CONICA
NEAT	Near Earth Asteroid Tracking
NICMOS	Near Infrared Camera and Multi-Object Spectrometer
NIR	Near Infrared
OTF	Optical Transfer Function
PA	Position Angle
PDM	Phase Dispersion Minimisation
PLL	Phase Locked Loop
ppm	parts per million
PSF	Point Spread Function
PUEO	Probing the Universe with Enhanced Optics
QE	Quantum Efficiency
RAM	Random Access Memory
RMS	Root Mean Square
ROSAT	*Röntgensatellit*
RV	Radial Velocity
SDSS	Sloan Digital Sky Survey
SFTP	Secure File Transfer Protocol
SNR	Signal-to-Noise Ratio
TTL	Transistor-Transistor Logic
UCAC	USNO CCD Astrograph Catalog
USNO	US Naval Observatory
UTC	Coordinated Universal Time
UV	Ultraviolet
VLT	Very Large Telescope
WDS	Washington Double Star (Catalogue)
WFC	Wide Field Camera

Appendix

Acknowledgements

First and foremost, I would like to thank Wolfgang Brandner, Stefan Hippler, and Thomas Henning for the opportunity to carry out this thesis under their excellent supervision.

It is a pleasure to further acknowledge the support of the following people:

Stephan Birkmann for sharing the secrets of the 70 cm telescope with me.

Karl “Sam” Wagner for his efforts to re-activate the IA1 filter wheel.

Armin Böhm and the fine mechanics workshop for coping with my personal style of engineering drawings.

Lothar Kurtze for proof-reading and numerous helpful comments.

Ulli Thiele, Jens Helmling, João Alves, and all Calar Alto staff for the excellent support during the AstraLux observing runs.

Ángel Barbero and Jose Luis Corral for providing culinary reasons to enjoy Calar Alto even in bad weather.

And now the fineprint:

This work is based on observations collected at the Centro Astronómico Hispano Alemán (CAHA) at Calar Alto, operated jointly by the Max-Planck Institut für Astronomie and the Instituto de Astrofísica de Andalucía (CSIC).

This research has made use of the SIMBAD database, operated at CDS, Strasbourg, France.

This research has made use of NASA’s Astrophysics Data System Bibliographic Services.

This work is based on observations made with the NASA/ESA Hubble Space Telescope, obtained from the data archive at the Space Telescope Institute. STScI is operated by the association of Universities for Research in Astronomy, Inc. under the NASA contract NAS 5-26555.

Based on observations made with ESO Telescopes at the La Silla or Paranal Observatories under programme ID 074.C-0084.

This publication makes use of data products from the Two Micron All Sky Survey, which is a joint project of the University of Massachusetts and the Infrared Processing and Analysis Center/California Institute of Technology, funded by the National Aeronautics and Space Administration and the National Science Foundation.

This document was typeset in LaTeX, using TX fonts.

Back illustration:

The Calar Alto 3.5 m telescope, photographed from the catwalk of the 2.2 m telescope dome during sunset.

The spatial resolution of astronomical observations from the ground is impaired by earth's atmosphere. Turbulent variations of the refractive index of the air above a telescope degrade the image resolution to values of typically one arcsecond in the visible light, seventy times worse than the diffraction limit of an 8-m class telescope.

This has been overcome in the past years by the development of adaptive optics systems. These instruments actively compensate the wavefront aberrations introduced by the atmosphere and allow diffraction limited imaging at large telescopes in the near infrared.

This thesis covers an alternative, totally passive approach to the problem of high resolution imaging through the atmosphere. The Lucky Imaging Technique exploits the temporal behaviour of atmospheric turbulence. By selecting only the best few percent of several thousand short exposure images, it is possible to recover the full angular resolution of medium-sized telescopes at visible wavelengths. This can be realised with a fraction of the instrumental effort and costs needed for adaptive optics.

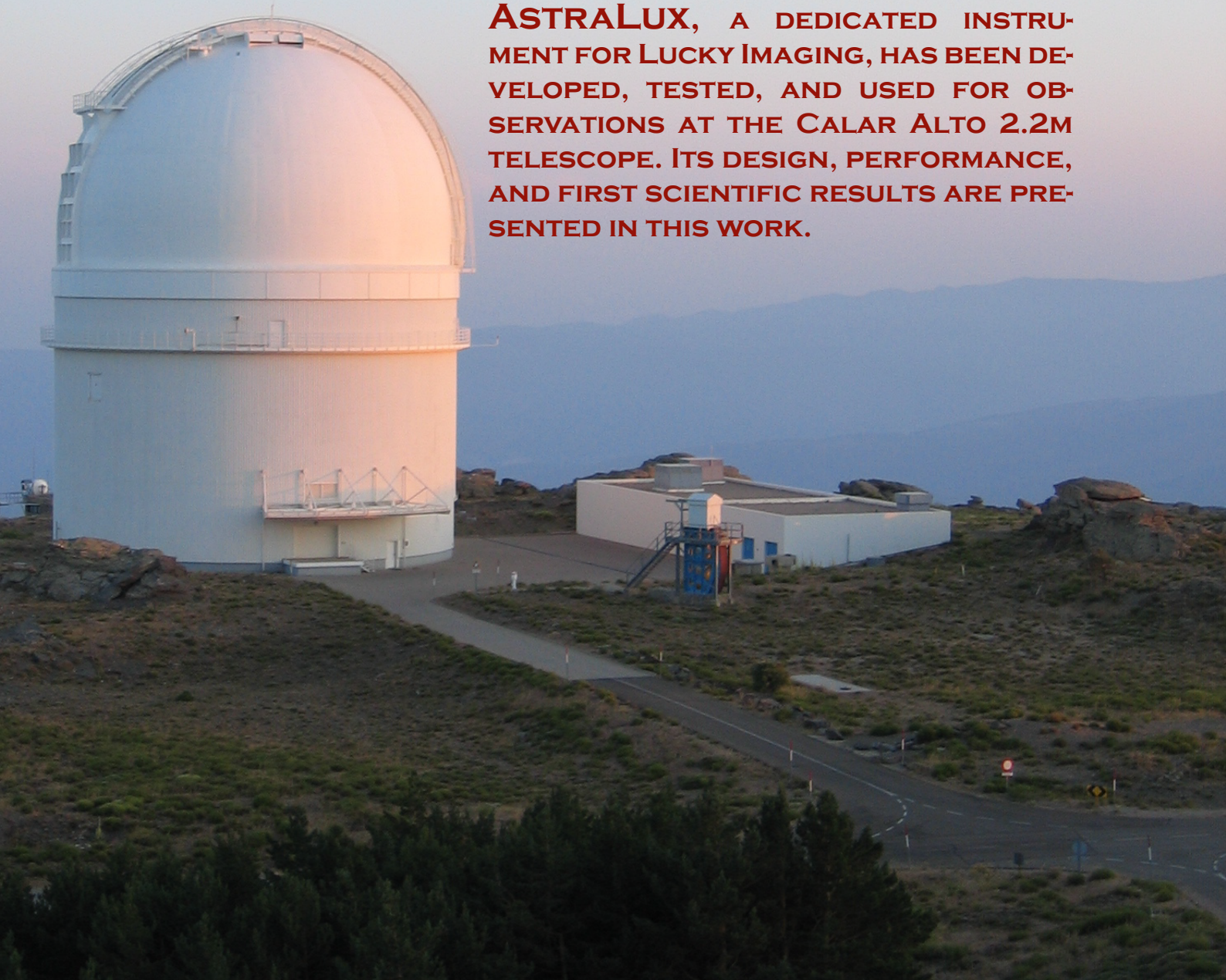

AstraLux, a dedicated instrument for Lucky Imaging, has been developed, tested, and used for observations at the Calar Alto 2.2m telescope. Its design, performance, and first scientific results are presented in this work.